# The First Experiments with Bose-Einstein Condensation of $^{87}$Rb

by

**Jason Remington Ensher**

B.S., State University of New York at Buffalo, 1993

M.S., University of Colorado at Boulder, 1996

A thesis submitted to the

Faculty of the Graduate School of the

University of Colorado in partial fulfillment

of the requirements for the degree of

Doctor of Philosophy

Department of Physics

1998

This thesis entitled:
The First Experiments with Bose-Einstein Condensation of $^{87}$Rb
written by Jason Remington Ensher
has been approved for the Department of Physics

Eric Cornell

Carl Wieman

Date

The final copy of this thesis has been examined by the signatories, and we find that both the content and the form meet acceptable presentation standards of scholarly work in the above mentioned discipline.

Ensher, Jason Remington (Ph.D., Physics)

The First Experiments with Bose-Einstein Condensation of $^{87}$Rb

Thesis directed by Prof. Eric Cornell

Bose-Einstein Condensation (BEC) is the macroscopic occupation of the ground-state of a system of bosons that occurs when the extent of the wavefunctions of the particles is comparable to the interparticle spacing. Although predicted by Albert Einstein in 1924, BEC in a dilute system was observed only recently in an atomic vapor of $^{87}$Rb by our group in 1995. This thesis describes the first experiments to explore the properties of this new state of matter. In early experiments, we studied how interparticle interactions modify the ground-state wavefunction and mean energy. We observed phonon-like collective excitations of the condensate. We studied modes of different angular momenta and energies. Our observations of how the characteristics of the modes depend on interactions quantitatively supported the mean-field picture of the dilute BEC. Shortly thereafter, we developed thermometry and calorimetry to study the ground-state fraction and mean energy of the Bose gas as a function of temperature. The BEC transition temperature and the temperature dependence of the ground-state fraction are in good agreement with predictions for an ideal Bose gas. However, the measured mean energy is larger than that of the ideal gas below the transition. We observe a distinct change in the energy-temperature curve near the transition, which indicates a sharp feature in the specific heat.

In an effort to produce larger condensates we constructed a double-MOT apparatus that became the third-generation machine at JILA to observe

and study BEC. The new apparatus produces condensates five times more quickly than the original experiment, increasing the number of atoms in the condensate from several thousand to 1-2 million atoms. Using the improved apparatus, we studied the TOP (time-averaged orbiting potential) magnetic trap. An important, new observation is that the trap symmetry is affected by the sag due to gravity, an effect which can be exploited to create very harmonic, spherical potentials. We also measured a sharp decrease in trap lifetime for bias fields below 1 G. The improved understanding of the TOP trap should enable future interesting experiments with BEC.

I dedicate this thesis to my family, and especially to Mom.

## Acknowledgements

I would like to acknowledge the many people who have helped make my thesis work fun and rewarding. I thank my advisor Eric Cornell for giving me the opportunity to work on the BEC experiment. He helped me cultivate my skills as a scientist and has been an outstanding source of support and advice throughout my graduate work. Similarly, I thank Carl Wieman for being my de facto second advisor, offering guidance and terrific insights. It has been a privilege and a pleasure to work with such outstanding physicists as Eric and Carl. I have learned tremendously not only from their advice, but also from watching them work their magic.

I also want to thank all of the post-docs with whom I have worked in the lab. I thank Nate Newbury, Wolfgang Petrich and especially Mike Anderson for teaching me the ropes and leading the charge to BEC. I also thank Debbie Jin, whose keen mind and constant drive was a great source of inspiration and taught me much about being a physicist. I also thank David Hall for his experimental and physical insights and for great camraderie in the lab.

My graduate experience was also blessed with many capable students who were also good friends. I especially thank Mike Matthews for his skills in the lab and in physics, and for his friendship. Around the BEC experiments

I thank Neil Claussen, Brian DeMarco, Rich Ghrist, Paul Haljan, Heather Lewandowski, Chris Myatt and Jake Roberts. I also thank Steve Bennett, Kristan Corwin, Tim Dineen, Kurt Vogel and Chris Wood.

Thanks go to Murray Holland, Jinx Cooper, Chris Greene and John Bohn for numerous discussions about the theoretical aspects of my work. I also thank the many JILA staff people who have helped me throughout my studies. In particular, thanks to Hans Rohner for all his glass-making artistry.

I will never forget the wonderful experience I had at the European Laboratory for Non-Linear Spectroscopy in Florence, Italy. I am grateful to Massimo Inguscio and Guglielmo Tino for their hospitality and support during my visit. I also thank Marco Prevadelli, Chiara Fort, Francesco Cattaliotti and Francesca for making my visit to Florence so productive and so much fun.

Finally, thank-you to all my friends, in and around physics, for putting up with me and making my graduate school years a lot of fun. I'd like to point-out a few people. First, I thank Brett Esry and Brad Paul for years of friendship, months of pre-comps preparation and one fantastic road-trip. We'll always have Tuktoyatuk. I also thank Julie Paul and especially Hilary Eaton. And I couldn't have made it without Kim King, John Metz, Sarah and Harold Parks, Sarah Roberts and Heather Robinson.

## Contents

**Chapter**

## Figures

**Figure**

# Tables

**Table**

# Chapter 1

## Introduction

In the conditions of our everyday experience, the quantum mechanical distinction of whether a gas is composed of bosons or fermions is irrelevant to the statistical behavior of the gas. The thermal wavelength of a gas particle is so small compared to the interparticle spacing that each particle appears perfectly distinguishable and countable. The gas therefore obeys classical statistics. We can quantify the degree of quantum degeneracy of the system by defining the phase space density of the system $D \equiv n\lambda_{dB}^3$, where $\lambda_{dB}$ is the thermal deBroglie wavelength $h/\sqrt{2\pi m k_B T}$ and $n$ is the density. For most temperatures and densities, the phase space density of a gas is much less than one. Typically, much, much less. In the controlled environment of a room temperature gas of rubidium in a vacuum of $10^{-11}$ Torr the phase space density is $\sim 10^{-22}$.

As Einstein first pointed out in 1924 [23], expanding upon a suggestion by Satyendranath Bose [24], if the temperature of a non-interacting gas of bosons is low enough and the density high enough such that the phase space density approaches unity, the quantum indistinguishability of the particles requires a new statistical description - later called Bose-Einstein statistics. Bose-Einstein Condensation (BEC) is an exotic consequence of the new statistics: When $D \rightarrow 2.612$, a gas of bosons accumulates in the ground-state of

the system. This condensation is driven purely by the quantum statistics of the bosons and not by interactions between them. A Bose condensate is also a unique state of matter, rich in interesting physics, because it is a many-body quantum state that involves a macroscopic fraction of the system.

Recently, advances in laser trapping and cooling, in conjunction with magnetic trapping and evaporative cooling have enabled the first observation of BEC in a dilute atomic vapor. The purpose of this thesis is to describe the first experiments with BEC in a gas of $^{87}$Rb. In this introductory chapter I present a brief history of BEC, particularly as it relates to systems of atomic gases. The presentation will not be comprehensive in the context of dilute atomic systems either, but focuses on the concepts and techniques essential to the research of the present work. In the first section I review the theory of ideal-gas BEC. The second section presents a history of the field, starting from the conceptual beginnings of Bose and Einstein, moving to the first real systems to show quantum degeneracy (liquid Helium, superconductive state of metals, and excitons) and then describing the efforts to achieve BEC in atomic systems. The third section describes the experimental situation when research for this thesis began in 1993, culminating in the observation of BEC in 1995. In the last section I outline the research of the thesis.

### 1.0.1 BEC in an Ideal Gas.

Consider a system of $N$ indistinguishable bosons, distributed among the microstates of a confining potential, such that any occupation number is allowable. The mean distribution, the Bose-Einstein distribution (BED), may be derived in several different ways. See for instance [25]. In the end one may always understand the BED as the most random way to distribute a certain

amount of energy among a certain number of particles in a certain potential. The BED gives the mean number of particles in the ith state as

$$n_i = \frac{1}{e^{(\epsilon_i - \mu)/kT} - 1} \tag{1.1}$$

where $\epsilon_i$ is the energy of a particle in the ith state, $k$ is Boltzmann's constant, and $T$ and $\mu$ are identified as the temperature and chemical potential, respectively. In the grand canonical understanding of the BED, $\mu$ and $T$ are determined from the constraints on total number $N$ and total energy $E$:

$$N = \sum_i \frac{1}{e^{(\epsilon_i - \mu)/kT} - 1} \tag{1.2a}$$

$$E = \sum_i \frac{\epsilon_i}{e^{(\epsilon_i - \mu)/kT} - 1} \tag{1.2b}$$

For systems with a large volume and an infinite number of particles, the constraints may be written as integrals

$$N = \int d\epsilon \frac{g(\epsilon)}{e^{(\epsilon - \mu)/kT} - 1} \tag{1.3a}$$

$$E = \int d\epsilon \frac{\epsilon g(\epsilon)}{e^{(\epsilon - \mu)/kT} - 1} \tag{1.3b}$$

where $g(\epsilon)$ is the density of states in the confining potential.

Equations (1.1)-(1.3) contain nearly all the ideal gas physics of BEC. The number of spatial dimensions, and the effects of a confining potential, are all taken care of in the power law of the density of states, $g(\epsilon)$. A particularly illuminating system is the "box-potential", a 3-d square well potential where within a volume $V$ the potential is flat and at the edge it goes to infinity. Extending the volume to infinity, while also allowing $N \to \infty$ such that the gas density $n$ is fixed we can use equations (1.3) to determine the ground state occupation as a function of temperature. The result is that when the phase space density of the system is $\approx 2.612$, the number of particles occupying all states of the system other than the ground-state saturates. The critical temperature for ideal-gas BEC in a gas with mass $m$ is related to density $n$ by

$$T_{c,ideal} = \frac{h^2}{2\pi m k}\left(\frac{n}{\zeta(3/2)}\right)^{2/3} \tag{1.4}$$

where $\zeta(z)$ is the Riemann zeta function and $\zeta(3/2) \approx 2.612$. Below this temperature and/or above this density, particles in the gas accumulate in the ground state of the system. Although this result was derived for a particular, homogeneous potential it actually applies to systems in all confining potentials where the critical temperature is much larger than the energy splitting between levels of the system [26].

The effects of finite number, and of very asymmetric potentials [27], can be determined by using the sums rather than the integrals to constrain $\mu$ and $T$. The critical temperature, the ground-state occupation fraction, the specific heat, can all be calculated without difficulty. Only number fluctuations, which require a more careful consideration of the underlying ensemble statistics,

are left out of this picture. The overall picture is sufficiently easy to understand that, if it the system truly **were** an ideal gas, there would be little left to study at this point.

As it actually has turned out, interactions between particles add immeasurably to the richness of the system. A central focus of the work in this thesis was to understand the role of interactions in dilute-gas BEC.

### 1.0.2 Some Real Systems

Einstein's original conception of BEC was in a dilute gas, but the first experiments in BEC were in superfluid Helium, a liquid, (which is to say a strongly correlated fluid, the opposite limit from a dilute gas). The beautiful and startling experiments on viscosity, vortices, and heat-flow in liquid Helium, and the ground-breaking theory those experiments inspired, more or less defined the field of Bose-Einstein condensation for four decades and more [28]. The BEC concept has been put to use in broader contexts over the years, however, in such diverse topics as Kaons in neutron stars [29], cosmogenesis, and exotic superconductivity [30]. Using the term in its broadest meaning ("macroscopic number of bosons in the same state") one needn't have a fluid of any sort – lasers and masers produce macroscopically occupied states of optical and microwave photons, respectively. For that matter, a portable telephone, or even a penny-whistle produce macroscopic occupation numbers of identical bosons (radio-frequency photons in one case, acoustic-frequency phonons, in the other.)

In superfluid He-4, the bosons exist independently of the condensate process. The fermionic neutrons, protons, and electrons that make up a He-4 atom bind to form a composite boson at energies much higher than the super-

fluid transition temperature. There exists a broad family of physical systems, however, in which the binding of the fermions to form composite bosons, and the condensation of those bosons into a macroscopically occupied state, occurs simultaneously. This of course is the famous BCS mechanism. Best-known for providing the microscopic physical mechanism of superconductivity, the Bose-condensed "Cooper pairs" of BCS theory occur in superfluid He-3 and may also be relevant to the dynamics of large nuclei [31] and of neutron stars.

Previous to the observation of BEC in a dilute atomic gas, the laboratory system which most closely realized the original conception of Einstein was excitons in cuprous oxide [32]. Excitons are formed by pulsed laser excitation in cuprous oxides. There exist meta-stable levels for the excitons which delay recombination long enough to allow the study of a thermally equilibrated Bose gas. The effective mass of the exciton is sufficiently low that the BEC transition at cryogenic temperatures occurs at densities which are dilute in the sense of the mean inter-particle spacing being large compared to the exciton radius. Recombination events, which can be detected either bolometrically [33] or by collecting their fluorescence [32] are the main experimental observable. The most convincing evidence for BEC in this system is an excess of fluorescence from "zero-energy" excitons. In addition, anomalous transport behaviour evocative of superfluidity has been observed [34].

As an experimental and theoretical system, BEC in a dilute gas is nicely complementary to the variety of BEC-like phenomena described above. In terms of strength of interparticle interaction, atomic gas BEC is intermediate between liquid helium, for which interactions are so strong that they can not be treated by perturbation theory, and photon lasers, for which "interactions" or nonlinearity, is small except in effectively two-dimensional configurations.

In terms of the underlying statistical mechanics, atomic-gas BEC is most like He-4. Unlike in superconductivity, the bosons are formed before the transition occurs, and unlike in lasers, the particle number is conserved. The properties of the phase transition, then, should most closely resemble liquid helium. Finally, in terms of experimental observables, atomic-gas BEC is in a class entirely by itself. The available laboratory tools for characterizing atomic-gas BEC are essentially orthogonal to those available for excitonic systems or for liquid helium.

## 1.1 History

### 1.1.1 Conceptual beginnings

The notion of Bose statistics dates back to a 1924 paper in which Satyendranath Bose used a statistical argument to derive the black-body radiation spectrum [24]. Albert Einstein extended the statistical model to include systems with conserved particle number [35, 23]. The result was Bose-Einstein statistics. Particle which obey B-E statistics are called bosons, and of course today it is known that all particles with integer spin (and only those particles) are bosons. Einstein immediately noticed a peculiar feature of the distribution: at low temperature, it saturates. "I maintain that, in this case, a number of molecules steadily growing with increasing density goes over in the first quantum state (which has zero kinetic energy) while the remaining molecule separate themselves according to the parameter value $A = 1$ [in modern notation, $\mu = 0$] ... A separation is effected; one part condenses, the rest remains a 'saturated ideal gas.' " [35, 36] Thus began the concept of Bose-Einstein condensation.

BEC has not always been a particularly reputable character. In the decade following Einstein's papers, doubts were cast on the reality of the model [37]. Fritz London and L. Tisza [38, 39] resurrected the idea in the mid 1930s as a possible mechanism underlying superfluidity in liquid helium-4. London's view was either disbelieved or else felt to be not particularly illuminating. Certainly the influential helium theory papers of the 50s and 60s make little or no mention of BEC. [40, 41, 42]. I am not well-versed in the history of that era, but it is evident that sometime in the intervening years the bulk of expert opinion has shifted. Experiment and theory (neutron scattering [43] and path-integral Monte Carlo simulations [44], respectively) now support the idea that the microscopic physics underlying superfluidity is a zero-momentum BEC. Due to interactions, only about 10% of the helium atoms participate in the condensate, even at temperatures so low that empirically 100% of the fluid appears to be in the super state.

### 1.1.2 Spin-polarized hydrogen

Efforts to make a dilute BEC in an atomic gas were spurred by provocative papers by Hecht [45] and Stwalley and Nosanov [46]. They argued on the basis of the quantum theory of corresponding states that spin-polarized hydrogen would remain a gas down to zero temperature, and thus would be a great candidate for making an weakly interacting BEC. A number of experimental groups [47, 48, 49, 50] in the late 70s and early 80s began work in the field. Spin-polarized hydrogen was first stabilized by Silvera and Walraven in 1980 [47], and by the mid-80s spin-polarized hydrogen had been brought within a factor of 50 of condensing [49]. These experiments were performed in a dilution refrigerator, in a cell whose walls were coated with superfluid liq-

uid helium. A radiofrequency (rf) discharge dissociated hydrogen molecules, and a strong magnetic field preserved the polarization of the resulting atoms. Individual hydrogen atoms can thermalize with a superfluid helium surface without becoming depolarized. The atoms were compressed using a (conceptually) simple piston-in-cylinder arrangement [51], or inside a helium bubble [52]. Eventually the helium surface became problematic, however. If the cell is made relatively cold, the surface density of hydrogen atoms becomes so large that they undergo recombination there. If the cell is too hot, the volume density of hydrogen necessary for BEC becomes so high that, before that density can be reached, the rate of three-body recombination becomes too high [53].

### 1.1.3 Laser cooling and the ascendancy of alkalis

Contemporaneous with (but quite independent from) the hydrogen work, an entirely different kind of cold-atom physics was evolving. The remarkable story of laser cooling has been reviewed elsewhere [54, 55, 56, 57] but we mention some of the highlights in compressed form below. The idea that laser light could be used to cool atoms was suggested in early papers from Wineland and Dehmelt [58], from Hänsch and Shawlow [59], and from Letokhov's group [60]. Early optical force experiments were performed by Ashkin [61]. Trapped ions were laser-cooled at the University of Washington [62] and at the National Bureau of Standards (now NIST) in Boulder [63]. Atomic beams were deflected and slowed in the early 80s [64, 65, 66]. Optical molasses was first studied at Bell Labs [67] and at the National Bureau of Standards in Gaithersburg [68]. The temperatures in optical molasses were understood from the following 1-d model. Consider a two-level atom which scatters photons from two counter-propagating laser beams of equal intensity and detuned to a frequency less than

the atomic resonance (at zero-velocity). The atom scatters more photons from the beam which opposes the atom's direction of motion because the frequency of the opposing beam is Doppler shifted closer to resonance. The momentum of the scattered photons reduce the kinetic energy of the atom. However, because the scattering is spontaneous, the random scattering also imparts a diffusive heating to the atom. The balance between the cooling and heating leads to the Doppler Temperature Limit, $T_d = \hbar\Gamma/2k_B$ where $\Gamma$ is the linewidth of the atom and $k_B$ is Boltzmann's constant. Measured temperatures in the early molasses experiments were consistent with the Doppler limit, which amounts to about 300 microkelvin in most alkalis.

Coherent stimulated forces of light were studied [69, 70]. The dipole force of light was used to confine atoms as well [71]. Then in 1987 there was a major advance. Pritchard and coworkers demonstrated a practical spontaneous-force trap, the Magneto-Optical trap (MOT) [72]. The MOT works because real atoms have internal level structure. By superimposing a quadrupole magnetic field onto three orthogonal pairs of suitably polarized, counter–propagating laser light, a spatially varying photon scattering rate is achieved. The scattered photons create a damping and restoring force that confines the atoms. A second major advance came in 1988 when it was observed that under certain conditions, the temperatures in optical molasses are in fact much colder than the Doppler-limit [73, 74, 75]. These were heady times in the laser-cooling business. The MOT had generated much higher densities in the trapped gases. With experiment yielding temperatures mysteriously far below what theory would predict, it seemed reasonable enough at the time to speculate that still colder temperatures and still higher densities were due to arrive shortly. Perhaps the methods of laser cooling and trapping might soon

lead directly to BEC!

### 1.1.4 Cold reality: limits on laser cooling

It didn't happen that way, of course. By 1990 it was clear that there were fairly strict limits to both the temperature and density obtainable with laser cooling. Theory caught up with experiment and showed that the sub-Doppler temperatures were due to a combination of light-shifts and optical pumping that became known as Sysiphus cooling. Random momentum fluctuations from the rescattered photons limit the ultimate temperature to about a factor of ten above the recoil limit [76]. The rescattered photons are also responsible for a density limit – the light pressure from the reradiated photons gives rise to an effective inter-atom repulsive force [77]. The product of the coldness limit and the density limit works out to a phase-space density of about $10^{-5}$, which is to say, five orders of magnitude too low for BEC.

Since 1990, advances in laser cooling and trapping have allowed both the temperature [78, 79] and the density [80] limit to be circumvented. But it seems that in most cases higher densities have been won at the cost of high temperatures, and lower temperatures have been achievable only in relatively low density experiments. The peak phase-space density in laser cooling experiments has increased hardly at all in the decade since 1989 [81]. For instance, MOT's typically operate at or slightly below the Doppler Temperature. Sub-Doppler cooling is suppressed by the magnetic field gradients intrinsic to the MOT. The limitations to temperature in MOTs on the one hand and the densities in optical molasses on the other inevitably shaped how these techniques were later integrated into a method to achieve BEC.

The alkali-atom work of the 1980s included another development,

however, which was to have a large impact on BEC work. Sodium atoms were trapped in purely magnetic traps [82, 83, 84].

### 1.1.5 Magnetic Trapping

Magnetic traps for neutral atoms play an essential role in the road to BEC. The magnetic moment $\vec{\mu}$ of an atom interacts with a magnetic field $\vec{B}$ (to first order) through the Hamiltonian $H = -\vec{\mu} \cdot \vec{B}$. The potential energy of atoms that are spin aligned with the field increases as the magnetic field increases. Hence, the atoms experience a force towards lower magnetic fields. By creating a local minimum in the magnetic field we can confine these so-called "weak-field seeking" states. For alkali atoms, where we describe the ground-state structure of the atoms in the hyperfine angular momentum picture, the magnetic potential energy is $U_{mag} = m_F g_F B$, where $m_F$ is the magnetic sublevel and $g_F$ is the Landé g-factor of the atomic state. Rubidium 87 is the atom used in experiments for this thesis work and it's structure is typical of the alkalis. It's nuclear magnetic moment is $I = 3/2$, yielding two hyperfine ground states, $F = 1$ and $F = 2$. Based on the above arguments (see also Figure 1.1), three states of $^{87}$Rb are trapped: $|F = 2, m_F = 2\rangle$, $|2, 1\rangle$ and $|1, -1\rangle$.

### 1.1.6 Evaporative cooling and the return of Hydrogen

Harold Hess from the MIT hydrogen group realized the significance that magnetic trapping could make for their BEC effort. Atoms in a magnetic trap have no contact with a physical surface and thus the surface recombination problems could be circumvented. Moreover, thermally isolated atoms in a magnetic trap were the perfect candidate for evaporative cooling. In a remarkable paper Hess laid out in 1986 most of the important concepts of evaporative

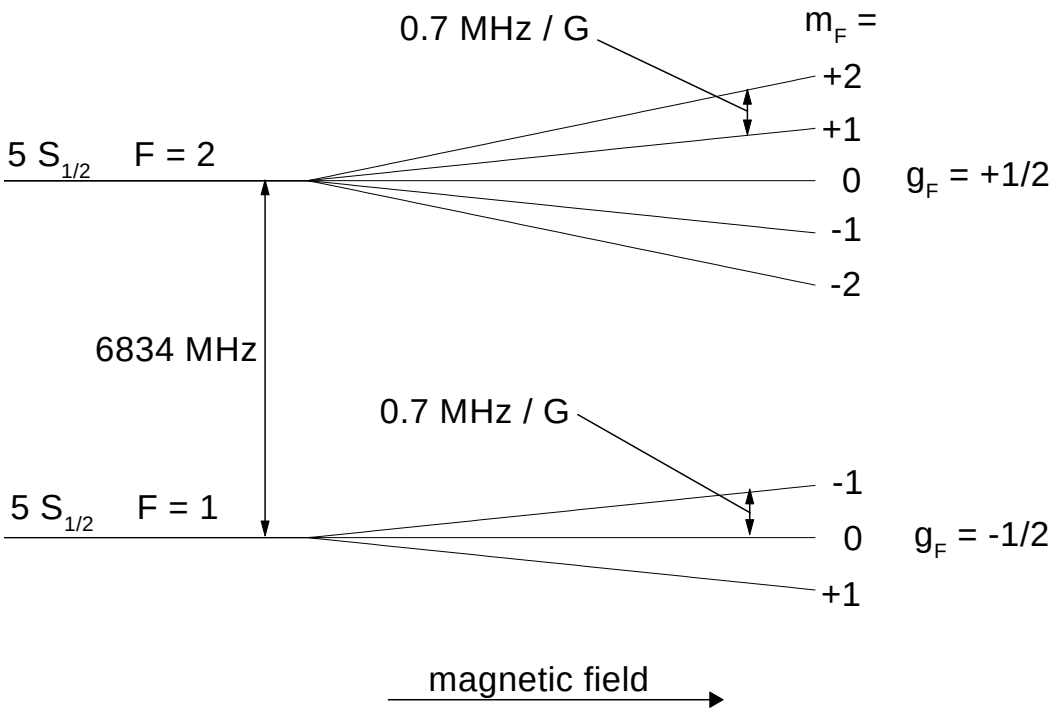


Figure 1.1: Rubidium 87 $5S_{1/2}$ Zeeman energy level structure

cooling of trapped atoms [53]. Let the highest energy atoms escape from the trap, and the mean energy, and thus the temperature, of the remaining atoms will decrease. In a dilute gas in an inhomogeneous potential, decreasing temperature in turn means decreasing occupied volume. One can actually increase the density of the remaining atoms even though the total number of confined atoms decreases. The Cornell University Hydrogen group also considered evaporative cooling [85]. By 1988 the MIT group had implemented these ideas and had demonstrated that the method was as powerful as anticipated. In their best evaporative run, they obtained, at a temperature of 100 $\mu$K, a density only a factor of five too low for BEC [86]. Further progress was limited by dipolar relaxation, but perhaps more fundamentally by loss of signal-to-noise, and the need for a more accurate means of characterizing temperature and density in the coldest clouds [87]. Evaporative work was also performed by the Amsterdam group [88].

The evaporation results from MIT made a big impression on the JILA alkali group. It seemed that a hybrid approach combining laser cooling and evaporation had an excellent chance of working. Evaporation from a magnetic trap seemed like a very appealing way to circumvent the limits of laser cooling. Laser cooling could serve as a pre-cooling technology, replacing the dilution refrigerator of Hydrogen work. With convenient lasers in the near-IR, and with the good optical access of a room-temperature glass cell, detection sensitivity could approach single-atom capability. The elastic cross-section, and thus the rate of evaporation, should almost certainly be larger in an alkali atom than it is in hydrogen. Encouraged by these thoughts (and by other collisional considerations, see section 1.1.8 below) the JILA group set out to combine the best ideas of alkali and of hydrogen experiments, in an attempt to see BEC in

an alkali gas.

### 1.1.7 Hybridizing MOT and evaporative cooling techniques

In a sense efforts to hybridize optical cooling with magnetic trapping are as old as atomic magnetic trapping itself. The original NIST magnetic trap [83] and the first Ioffe-Pritchard (IP) trap [84] were loaded by an Zeeman-tuned optical beam-slower. Most modern alkali BEC apparatuses, however, can trace their conceptual roots through a series of devices built at JILA during an era beginning in late 1980's and continuing into the early 90s [89, 90, 91, 92, 20, 93, 94]. As things stood at the end of the 1980s, optical cooling on the one hand and magnetic trapping on the other were both somewhat heroic experiments, to be undertaken only by advanced and well-equipped AMO laboratories. The prospect of trying to get both working, and working well, on the same bench and on the same day was daunting.

The JILA vapor-cell MOT, with its superimposed IP trap (Figure 1.2) represented a much-needed technological simplification and introduced a number of ideas which are now in common use in the hybrid trapping business [89, 90]: i) Vapor-cell (rather than beam) loading; ii) fused-glass rather than welded-steel architecture. iii) extensive use of diode lasers; iv) magnetic coils located outside the chamber; v) over-all chamber volume measured in cubic centimeters rather than liters; vi) temperatures measured by imaging an expanded cloud; vii) magnetic-field curvatures calibrated **in situ** by observing the frequency of dipole and quadrupole (sloshing and pulsing) cloud motion. In the early experiments [89, 91, 90, 92] a number of experimental issues came up that continue to confront all BEC experiments: the importance of aligning the centers of the MOT and the magnetic trap; the density-reducing effects of

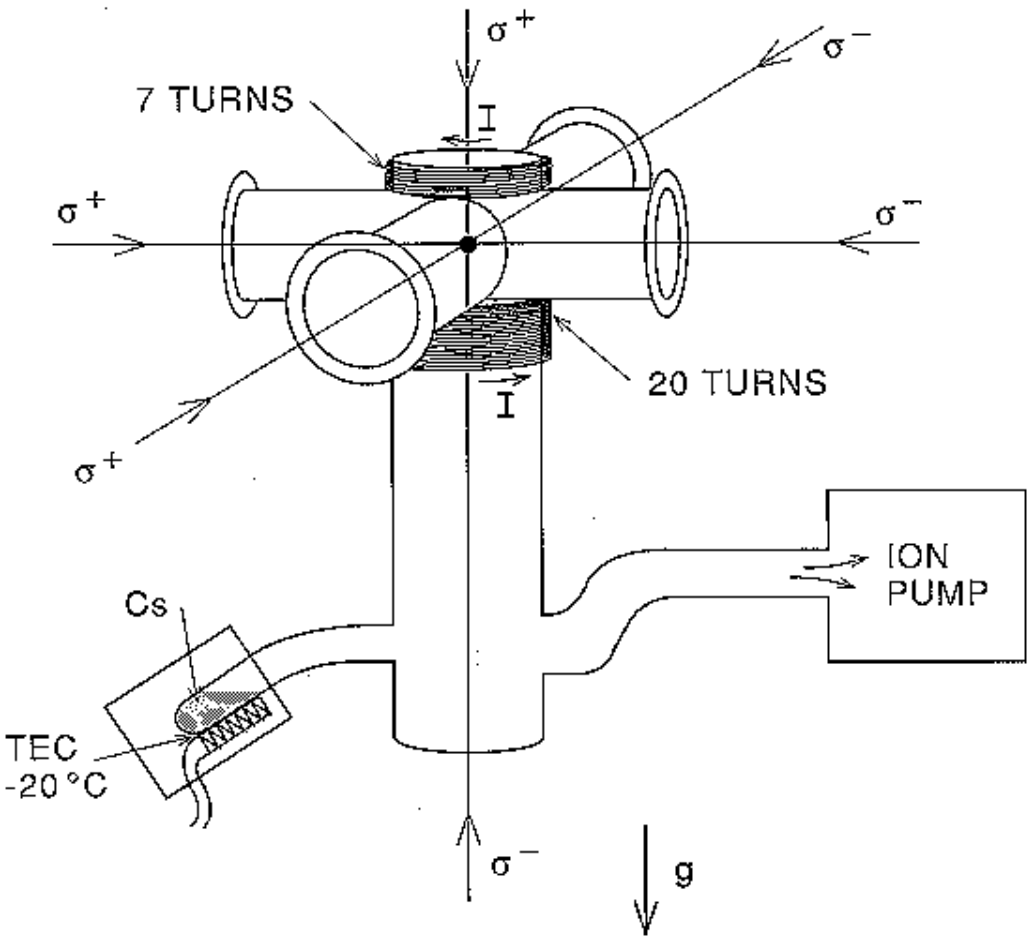


Figure 1.2: The first vapor cell used by Monroe, et. al 1990

mode-mismatch; the need to account carefully for the (usually ignored) force of gravity; heating (and not merely loss) from background gas collisions; the usefulness of being able to turn off the magnetic fields rapidly; the need to synchronize many changes in laser status and magnetic fields together with image acquisition. At the time the design was quite novel, but by now it is almost standard. It is instructive to note how much our current, third generation BEC device (Figure 1.3) resembles its ancestor (Figure 1.2).

The basic MOT properties established in the early vapor cell work laid the foundation for the development of the MOT as a pre-cooling stage for reaching BEC. The first demonstrated MOT was loaded from an atomic beam and the collection rate was therefore more or less determined by the beam flux. In the vapor cell, however, the source of atoms is a room temperature bath of atoms. The intersection of the six MOT beams defines a trapping volume $V$ where atoms may be caught from the vapor, but the optical forces of the MOT are only able to slow down a small fraction of the total speed distribution of atoms, typically characterized by a maximum capture velocity $v_c$. The rate $R$ at which the MOT captures atoms out of the vapor works out to be

$$R = \frac{P}{2k_B T} V^{2/3} v_c^4 \left( \frac{m}{2k_B T} \right)^{3/2} \tag{1.5}$$

where $P$ and $T$ are the ambient vapor pressure and temperature, respectively [89]. Several mechanisms can lead to loss from the trap. First, room temperature rubidium atoms in the untrapped vapor can collide with the trapped atoms with enough energy to cause a loss from the trap at a rate $1/\tau_{Rb}$. A second class of loss mechanisms are inelastic losses from collisions between trapped

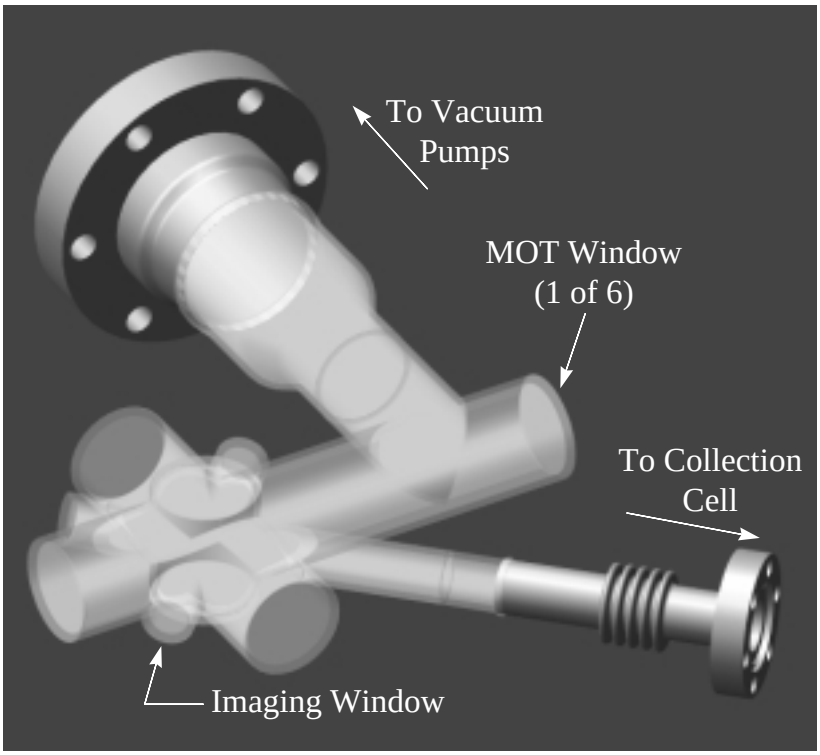


Figure 1.3: Vapor cell of the Science MOT of the Third Generation BEC Machine (JILA III).

atoms. The primary mechanism is photon-assisted binary collisions. An atom, excited by a scattered photon can spontaneously emit the photon during a collision with a ground state atom, gaining kinetic energy (from moving along the excited state potential) that exceeds the energy depth of the MOT. The overall rate equation for the MOT is

$$\frac{\mathrm{d}N}{\mathrm{d}t} = R - \frac{N}{\tau_{Rb}} - \beta \int n^2(\vec{r}) d^3r, \tag{1.6}$$

where $\beta$ is the rate constant for light-assisted collisional losses (see for example Ref.[20]). Since $1/\tau_b \sim P$, at high vapor pressure the light-assisted losses can be negligible and the number in the MOT achieves a steady state $N_{ss} = R\tau_{Rb}$. In this "vapor-pressure limited regime", increasing vapor pressure actually doesn't help improve conditions for evaporation: the number is independent of pressure (note dependence of $R$ and $\tau$ on $P$) while the lifetime is decreasing. We therefore needed to keep the background pressure low but find another way to increase the density within the MOT (see Section 1.2).

### 1.1.8 Collisional concerns

From the very beginning, dilute-gas BEC experiments had to confront the topic of cold collisions. Even before evaporation was considered, when cooling was simply a matter of conduction to the chamber walls, the rate of three-body decay determined the lifetime of samples of spin-polarized hydrogen samples. With the advent of evaporation, there was a demand for understanding several different collisional processes – elastic collisions, dipolar relaxation, three-body recombination, and to a lesser extent spin-exchange.

Atomic collisions at very cold temperatures is now a major branch of the discipline of AMO physics, but in the early 1980s there was almost no experimental data, and what there was came in fact from the spin-polarized hydrogen experiments [95] There was theoretical work on hydrogen from Shlyapnikov and Kagan [96, 97], and from Silvera and Verhaar [98]. An early paper by Pritchard [99] includes estimates on low-temperature collisional properties for alkalis. His estimates were extrapolations from room-temperature results, but in retrospect they were surprisingly accurate.

Experiments on cold collisions between alkali atoms were initially all performed on inelastic excited-state/ground-state collisions in MOTs [100, 101, 102]. The earliest ultra-cold ground-state on ground-state measurements were based on pressure-shifts in the Cs clock transition [103] and thermalization rates in magnetically trapped cesium [92], Rb [94] and Na [104]. Eventually experiment and theory of excited state collisions, in particular photoassociative events, yielded so much information on atom-atom potentials that ground-state cross-sections could be extracted [105, 106, 107, 108, 109, 110]. By the time BEC was observed in rubidium, sodium, and lithium, there existed at least at the 20% level reasonable estimates for the respective elastic scattering length of each species. Evaporation efforts on all three species were initially begun, however, under conditions of relatively large uncertainty concerning elastic rates, and near-ignorance on inelastic rates.

In 1992 the JILA group came to realize that dipolar relaxation in alkalis should in principle not be a limiting factor. The scaling with temperature and field is such that, except in pathological situations, the problem of good and bad collisions in the evaporative cooling of alkalis is reduced to the ratio of the elastic collision rate to the rate of loss due to imperfect vacuum;

dipolar relaxation and three-body recombination can be finessed. Of course, even given successful evaporative cooling, there was still the question of the sign of scattering length, which must be positive to ensure the stability of a large condensate. The JILA group had sufficient laser equipment, however, to trap either $^{85}$Rb, $^{87}$Rb, or $^{133}$Cs. Given the "modulo" arithmetic that goes into determining a scattering length, it seemed fair to treat the scattering lengths of the three species as statistically independent events, and the chances then of Nature conspiring to make all three negative were too small to worry about. With regard to the possibility of all three being negative, we were also aware of the small-condensate exception that the Rice group was successfully able to exploit.

## 1.2 A thesis begins...

Such was the state of the art when I joined the JILA alkali group in the summer of 1993. In summary, we had a convenient way to load alkali atoms from a vapor (MOT) and a means to cool them (optical molasses). New cold collision data suggested that evaporative cooling would probably not be limited by too small elastic cross-sections or massive inelastic ones. The principle question that remained was: Could we combine these tools to load atoms into a magnetic trap in which evaporative cooling would runaway and take us to BEC? Specifically, we recognized that the challenge was to increase the elastic collision rate $n\sigma v$ (where $n$ is the gas density, $\sigma$ the cold collision cross-section and $v$ the relative collision velocity) compared to the loss rate from the magnetic trap (dominated by background losses).

A simple MOT, with operating parameters adjusted to maximize col-

lection rate, will have the density at which it can confine atoms limited by reradiated photon pressure to a relatively low value [77], with correspondingly low collision rate after transfer to the magnetic trap. Another complication arose for the vapor cells at JILA. Maximizing collection rate meant operating at high background vapor pressures that limited magnetic trap lifetimes.

### 1.2.1 Multiple Loading

Early efforts to surmount the density limit included a multiple-loading scheme pursued at JILA [91]. Multiple MOT-loads of atoms were launched in moving molasses, optically pumped into an untrapped Zeeman level, focused into a magnetic trap, then optically repumped into a trapped level. The repumping represented the necessary dissipation, so that multiple loads of atoms could be inserted in a continuously operating magnetic trap. In practice each step of the process involved some losses, and the final result hardly justified all the additional complexity. It is interesting to note, however, that multiple transfers from MOT to MOT [111, 93], rather than from MOT to magnetic trap, is a technique currently in wide-spread practice.

### 1.2.2 Compression

Another approach to the collision rate limitation of optical traps is the practice of magnetic compression. After loading into a magnetic trap from the optical trap, the atoms can be compressed by further increasing the curvature of the confining magnetic fields. In a harmonic trap, the collision rate after adiabatic compression scales as the final confining frequency squared [90]. This is a technique available to experiments which use MOTs to load the magnetic trap, but not to experiments which use cryogenic loading (in the latter, the

magnetic fields are usually already at their maximum values during transfer to maximize capture.) This method is discussed in [90] and was implemented first in early ground-state collisional work [92].

### 1.2.3 Enhancing MOT density

An important advance came from the MIT Sodium group in 1992, when they developed the Dark-spot MOT [80]. A shadow is arranged in the repumping light, such that atoms that have already been captured and concentrated in the middle of the trap are pumped to an internal state that is relatively unperturbed by close neighbors. In effect, the MOT is divided into two spatial regions, one for efficient collection, and one for efficient compression and storage. In a related technique, our group at JILA modulated the MOT parameters temporally, rather than spatially. The approach (dubbed CMOT for Compressed MOT) achieved transient compression of the MOT cloud for an order of magnitude increase in the density [19]. A very thorough study of related MOT behavior came out of a British-French collaboration [112].

### 1.2.4 Reducing background loss

Since the most important figure of merit in the evaporation business is the ratio of trap lifetime to elastic collision time, one can do almost as much good improving vacuum as one can improving MOT density. Early machines for cooling atomic beams were relatively dirty, by the standards of modern UHV practice. Except for the Pritchard group's cryogenic trap [84], confinement times in trapping experiments were usually on the order of two or three seconds. Improved beam design [113, 114] and the adoption of modern UHV practice has made 100 s lifetimes standard. Shortly after the CMOT work, we recognized

the importance of a Dark-spot MOT for our vapor cell traps. By forcing atoms in the central, dark region of the trap into a state that is also dark to the trap light we dramatically suppressed light-assisted collisional losses [20]. We could collect an order of magnitude more atoms into the forced Dark-spot MOT with over an factor of ten longer lifetime than the vapor cell MOT at the same background vapor pressures. At our lowest background pressures ($< 10^{-12}$ Torr), we also observed a 1000s MOT lifetime. For fixed trap volumes, the product of atom number and lifetime is proportional to the ratio of elastic to loss-inducing collisions. With the Dark-spot MOT we substantially improved the ratio achieved through optical collection from a vapor, setting the stage for the first attempts at evaporative cooling of alkali atoms.

### 1.2.5 Forced evaporation

Cooling by evaporation is a process found throughout nature. Whether the material being cooled is an atomic nuclei or the Atlantic ocean, the rate of natural evaporation, and the minimum temperature achievable, are limited by the particular fixed value of the work-function of the evaporating substance. In magnetically confined atoms, no such limit exists, because the "work function" is simply the height of the lowest point in the rim of the confining potential. Hess pointed out [53] that by perturbing the confining magnetic fields, the work-function of a trap can be made arbitrarily low; as long as favorable collisional conditions persist, there is no lower limit to the temperatures attainable in this forced evaporation. Pritchard [115] pointed out that evaporation could be performed more conveniently if the rim of the trap were defined by an RF-resonance condition, rather than simply by the topography of the magnetic field; experimentally, his group made use of position-dependent RF

transitions to selectively transfer magnetically trapped sodium atoms between Zeeman levels and thus characterized their temperature [116]. From 1993-1995, a number of other experimental groups launched efforts to create BEC in alkali species using the hybrid laser-cooling/evaporation approach. Progress accelerated and by summer of 1994 three groups, including the JILA team, had announced the successful use of evaporation to increase the phase-space density of trapped alkalis [21, 117, 104]. By the DAMOP meeting in Toronto, in May of 1995, the number of groups with clear evidence of evaporative cooling had increased to four [118]. The Rice, JILA, and MIT alkali groups were all seeing orders of magnitude increase in phase-space density.

### 1.2.6 Magnetic trap improvements

Of the three groups reporting run-away evaporation at Toronto, each had recently implemented a major upgrade in magnetic trap technology. Using compression of the atom cloud (Section 1.2.2), there was much to be gained by building a more tightly confining magnetic trap. Unfortunately, the requirement of adequate optical access for the MOT, along with engineering constraints on power dissipation, make the design problem complicated. When constructing a trap for weak-field seeking atoms, with the aim of confining the atoms to a spatial size much smaller than the size of the magnets, one would like to use linear gradients. The quadrupole magnetic trap conveniently addressed all the above concerns. It generates a linear magnetic field gradient from a pair of coils in anti-Helmholtz configuration. In addition to requiring only 2 coils, the quadrupole field is intrinsic to the MOT. In quadrupole potential however one is confronted with the problem of the minimum in the magnitude of the magnetic fields (and thus of the confining potential) occurring at a local zero

in the magnetic field. This zero represents a "hole" in the trap, a site at which atoms can undergo Majorana transitions and escape from the trap. If one uses the second-order gradients from the magnets to provide the confinement, there is a marked loss of confinement strength. This scaling is discussed for instance in reference [21].

The three experimental groups each solved the problem differently. The Rice group built a trap with permanent magnets [114] that can be stronger than electromagnets. The MIT and JILA groups each built traps with linear gradients, and then "plugged the hole." At MIT, a beam of blue-detuned light repelled atoms from the magnetic zero region [104]. At JILA, we added a small rotating bias field to displace the static quadrupole zero and orbit it in a radius that encompasses all the atoms [21]. The rotation frequency is chosen large enough that the atoms perceive only a time-averaged potential that is nearly harmonic with a micromotion associated with the rapid bias rotation that is negligibly small. Details of the so-called TOP trap are discussed later in this thesis (Chap. 6 and Appen. C).

As it turned out, all three methods worked well enough. In Spring of 1995 (less than three weeks after the DAMOP meeting), the JILA group saw BEC in rubidium 87, and by Autumn of 1995 all three groups had either observed BEC or else had preliminary evidence for it [22, 119, 120]. If one is willing to accept tight confinement in two directions only, it turns out that the original IP design, operated with a very low bias field, is more than adequate to produce BECs. In 1996, BEC was observed in second-generation traps at both MIT [121] and JILA [122]. The fields were in the IP configuration; additional coils were used to nearly null the central magnetic field.

### 1.2.7 Early research with BEC

The initial observation of BEC raised several important questions. Would the system be robust enough to allow repeated, quantitative study of the condensates? The first experiments were complicated by poor imaging resolution (a technical problem, but not a limit), slow experimental cycles (a fact of life for the vapor cell Dark-Spot MOT), periodic irreproducibility and a temperamental apparatus (both resolved by improving the lifetime and noise in the magnetic trap, and by optimizing evaporation). In terms of the physics, BEC was a vast, undiscovered country. The first measurements of BEC measured a transition temperature that was higher than expected for an ideal Bose gas, although the discrepancy was partly attributed to imaging systematics [22]. Meanwhile, the effects of a repulsive mean-field interaction seemed to be evident in our ballistic expansion data, further shaking the notion of a non-interacting condensate [22] in $^{87}$Rb. Our first task was to improve our BEC machine to make condensates more repeatably, with more atoms and better imaging diagnostics. Next, we identified those observables we could quantify and measure to understand the physics of BEC. We soon returned to the unresolved issues of interparticle interactions and the thermodynamics of BEC.

### 1.2.8 The Next Generation BEC Machine

Even as we were performing the first experiments with BEC, a new approach to overcome the limitations of the vapor cell was being developed. Using only a single vapor cell we needed to operate at low background pressures to insure long magnetic trap lifetimes. The forced dark-spot enabled us to fill

the MOT up to $\sim 10^7$ atoms, but at the expense of long fill times and hence long times between condensates ($3-5$ min). With an efficiency of evaporating only 1 in 1000 of the initially loaded atoms into the condensate we were limited to relatively small condensates ($\lesssim 10^4$). Large condensates were desired for a number reasons such as improving the signal-to-noise of the condensates and increasing the size of interatomic interactions within (and between separate) condensates.

The solution was the double-MOT apparatus [93]. The conflicting features of high collection rate (for rapid loading) and long lifetime and compact cell (for high confinement, long lifetime magnetic trapping and good evaporation) were delegated to two separate vapor cells. A high collection rate MOT is formed in the first cell via: (i) High rubidium pressure ($\sim 10^{-9}$ Torr) and (ii) Larger windows (38-51 mm) to allow larger and more powerful MOT beams. The second vapor cell is connected to the first with a long, narrow tube to allow differential pumping and a very low ($\sim 10^{-11}$ Torr) vapor pressure for long magnetic trap lifetimes in the second cell. Atoms from the (first) "Collection MOT" are transferred to the (second) "Science MOT" by pushing them repeatedly down the transfer tube.

## 1.3 Thesis Timeline and Outline

The remainder of the thesis is organized as follows. The first two years this thesis work were devoted to developing methods of increasing the MOT density (Ref. [19] and Appen. A), achieving initial conditions for evaporation (Ref. [20] and Appen. B) and creating a modified quadrupole trap, the TOP magnetic trap (Ref. [21] and Appen. C). This stage of the thesis culminated

in the first observation of BEC in a dilute gas of $^{87}$Rb in June, 1995 (Ref. [22] and Appen. D).

Chapter 2 describes early measurements of mean-field interactions and how they depend on both the number of atoms and the trap spring constants.

Chapter 3 describes our study of phonon-like collective excitations of the condensate. We observed modes with different angular momenta and different energies and studied how their characteristics depend on interaction energy. We also found that the condensate excitations persisted longer than their counterparts in uncondensed clouds.

By this time, we understood the ballistic expansion diagnostics well-enough to formulate a model-independent analysis for extracting thermodynamic quantities of the condensate. Chapter 4 presents detailed measurements of the ground-state occupation and mean-energy of the condensate as a function of temperature. These measurements were the first quantitative studies of the macroscopic properties of the condensate. In addition, the change in the slope of the energy-temperature curve at the transition temperature indicates a feature in the specific heat of the gas.

Driven by the desire for better signal-to-noise, larger condensates and shorter experimental cycles, I constructed the third generation BEC apparatus at JILA, a double-MOT system called JILA III. Chapter 5 discusses the construction and operating procedures and principles in exquisite detail.

After completion of JILA III, I transferred my knowledge of the double-MOT technology to the lab of Massimo Inguscio in Florence, Italy for the study of isotopes of potassium. Upon my return to Boulder, this thesis came full-circle. Working with JILA III, I revisited the TOP magnetic trap.

Chapter 6 present a comprehensive and detailed theoretical and experimental study of the TOP trap.

# Chapter 2

# Interactions in the Condensate at Zero Temperature

## 2.1 BEC: The Undiscovered Country

The initial observation of Bose-Einstein Condensation (BEC) [22] in a dilute vapor of $^{87}$Rb spurred great interest in experimentally studying the quantum phase transition and the macroscopic quantum state, in a system whose good diagnostics promised quantitative comparison to theory. These aspirations raised several important questions. From a technical perspective, could the system become robust enough to allow repeated, quantitative study of the condensates? In terms of the physics, could we understand the details of the condensate physics? Our roadmap for these initial studies was the set of unresolved observations made by Anderson, *et al* [22] regarding the presence of mean-field interactions and the temperature of the BEC transition. In this chapter I describe our first efforts to quantitatively study the mean-field interactions in pure condensates [123]. Understanding the BEC phase transition would wait until the results of the seminal studies of this chapter paved the way to more sophisticated analysis (see Chapter 4).

## 2.2 Theory of Interactions in a dilute Bose gas

Bose condensates in dilute alkali vapors such as $^{87}$Rb should be well-described by the Gross-Pitaevskii theory of weakly interacting bosons [124, 125, 126, 127]. The effects of binary collisions are described by a mean-field interaction, parameterized by the two-body scattering length $a$. Considering only binary collisions leads to a non-linear Schrödinger equation, the Gross-Pitaevskii (GP) equation, for the condensate wavefunction $\Psi$ of the form:

$$i\hbar\frac{\partial\Psi}{\partial t} = \left(-\frac{\hbar^2\nabla^2}{2m} + V_{\text{ext}} + \frac{4\pi\hbar^2 a}{m}|\Psi|^2\right)\Psi \tag{2.1}$$

where $V_{\text{ext}}$ is the external potential of the trap. For our experiments, the external potential is a cylindrically symmetric harmonic oscillator $V_{\text{ext}} = 1/2m(\omega_r^2x^2 + \omega_r^2y^2 + \omega_z^2z^2)$ in which the trap aspect ratio is $\lambda \equiv \omega_z/\omega_x$ . In a dilute gas at zero-temperature, the density $n$ at any point is space and time is $|\Psi|^2$. The non-linear interaction energy, relative to the harmonic oscillator energy, is proportional to $Na\sqrt{\nu_r}$ when the density distribution is well-approximated by a Gaussian distribution (see below and Refs. [128, 129, 130, 5]). Thus, varying the scattering length, trap frequency, or number of atoms changes the importance of interactions in the condensates.

In the limit of zero interactions ($a = 0$), the ground-state wavefunction of the Bose gas is the harmonic oscillator ground-state. The density distribution is therefore Gaussian:

$$n(\vec{r}) = \frac{N}{\sigma_r^3}\frac{\sqrt{\lambda}}{(2\pi)^{3/2}}e^{-(x^2+y^2+\lambda z^2)/\sigma_r^2} \tag{2.2}$$

where $\sigma_r = \sqrt{\frac{\hbar}{2m\omega_r}}$ is the root mean square (rms) size of the density distribution. The mean energy $(1+\lambda/2)\hbar\omega_r$ is equally divided among the mean kinetic and harmonic oscillator potential energies. The interactions for ground-state $^{87}$Rb atoms in our trap are effectively repulsive (scattering length $a > 0$) [108, 131] which tends to lower the central density of the condensate compared to the non-interacting case. This corresponds to less curvature, and therefore less kinetic energy, in the condensate wavefunction. In the limit of very strong interactions, the kinetic energy may be ignored (the Thomas-Fermi (TF) limit) and the ground-state density distribution mirrors the spatial form of the confining potential. Note that in the TF limit, the interactions are still weak in the sense of the scattering length being small compared to the mean interparticle spacing. A condensate confined in the harmonic potential of our experiments has a density distribution in the form of an inverted paraboloid. The TF wavefunction vanishes at a finite distance from the center of the potential. We define this distance as the half-width at zero maximum (hwom) in the radial ($R_{\rm hwom}$) and axial ($Z_{\rm hwom}$) directions:

$$n(\vec{r}) = \frac{15}{8\pi}\frac{N}{R_{\rm hwom}^2 Z_{\rm hwom}}\left(1-\left(\frac{x}{R_{\rm hwom}}\right)^2-\left(\frac{y}{R_{\rm hwom}}\right)^2-\left(\frac{z}{Z_{\rm hwom}}\right)^2\right) \tag{2.3a}$$

$$R_{\rm hwom} = 2\left(\frac{15}{2}\lambda a N\right)^{1/5}\sigma_r^{4/5} \tag{2.3b}$$

$$R_{\rm hwom} = \lambda Z_{\rm hwom} \tag{2.3c}$$

The mean energy is $\frac{5}{14}(\frac{15}{2}\frac{aN}{\sigma_r}\lambda)^{2/5}\hbar\omega_r$. Since there is no contribution from the kinetic energy, a generalization of the virial theorem shows that the energy is distributed between the harmonic oscillator and interaction potential energies in a ratio of 3 : 2 [5]. In the regime of atom number ($10^3$), trap frequency ($\nu_r \sim 100$ Hz) and scattering length (5.8 nm) of our early work neither the non-interacting nor the TF limit truly applies and a numerical solution of the GP equation is needed to extract the density profile. The mean energy is distributed between kinetic, harmonic oscillator and interaction energies $E_{\rm kin}$, $E_{\rm HO}$ and $E_{\rm int}$.

## 2.3 Experimental Procedure

Details of the experimental apparatus and procedures can be found elsewhere (see Appendix D and Chap. 3) and will only be outlined briefly here. We note that the experimental procedures described here differ from the methods of Chapter 5. We optically trapped and pre-cooled $^{87}$Rb from a vapor cell and then loaded the atoms into a purely magnetic TOP (time-averaged orbiting potential) trap. The TOP trap consists of a large static quadrupole field plus a small rotating transverse bias field [21]. The atoms

experience a time-averaged potential that is axially symmetric and harmonic with an axial to radial frequency ratio of $\sqrt{8}$. See Chap. 6 for more details. Atoms in the TOP trap were cooled further by forced evaporation, in which an applied radio frequency (rf) magnetic field selectively removes higher energy atoms by inducing Zeeman transitions to untrapped spin states [132, 115].

We observed the atoms with absorption imaging, using a 26 $\mu$s pulse of light near the $5S_{1/2}, F = 2 \rightarrow 5P_{3/2}, F = 3$ atomic transition to illuminate the atoms. A lens system, having a full-width half maximum spot size resolution of 6 $\mu$m, imaged the shadow of the cloud onto a charge-coupled device (CCD) array. By suddenly turning-off the magnetic trapping fields and allowing the cloud to expand ballistically before illuminating the atoms we circumvented the limited imaging resolution and observed a spatial distribution that accurately reflected the initial velocity distribution in the magnetic trap. The image was digitized and stored for analysis. The measurement destroys the cloud, but a full-cycle of loading, cooling and imaging the atoms could be repeated in several minutes.

We substantially improved our analysis of cloud shapes compared with our initial studies of BEC [22]. The digitized velocity distributions were fit to full 2-D profiles which approximate the observed density distributions (the observed distribution is actually the column density integrated through the cloud). For classical clouds, a 2-D Gaussian profile accurately describe the distribution. Pure condensates were fit to Gaussian or parabolic surfaces, though both functional forms leave systematic residuals. The fits to the observed clouds gave detailed information about the Bose gas. Temperatures were obtained from the width of a Gaussian fit to the classical component of the total Bose gas. The size of the Gaussian or paraboloid surface fit to the

condensate gave a close approximation to the spatial extent of the ground-state. By integrating under the area of the corresponding fit profiles we also obtained the number of condensate and classical atoms.

In addition to improved analysis, we substantially improved several aspects of the experimental apparatus. First, we decreased losses due to noise on the magnetic trapping fields and refined our evaporative cooling profiles such that overall efficiency of cooling an initially trapped atom into a pure condensate rose, from 1 in $10^4$, to 1 in $10^3$. The higher efficiency placed less severe demands on the initial collision rates required to begin evaporation and improved day-to-day robustness. Our ballistic imaging scheme was improved in two important ways. First, we decreased the turn-off time for the magnetic trap to allow us to turn off the trap potential rapidly enough to allow free expansions from traps with any radial frequency between 9 and 308 Hz [133]. Second, we changed from a single lens imaging system, with diffraction-limited fwhm spot size of 12.7 $\mu$m and magnification of 3.3, to a double-lens system with a diffraction limit fwhm spot size of 2 $\mu$m and magnification of 8.8. In practice, spherical aberrations in our optics and glass cell limited the fwhm resolution limit spot size to 6 $\mu$m. We reduced the $f/\#$ of our optics by moving the lens very near the atoms. This forced us to place the first lens in the path of the MOT light. By positioning the first lens one focal length in front of one of the retro-mirrors for the MOT (Fig.2.1) we preserved robust MOT performance and alignment. The retro-mirror was mounted on a flip-mount to remove it from the path of the probe light during the probe flash (and during the magnetic trap when no retromirror is required). For the optical-loading phase of the experiment, the mirror was returned to its initial position.

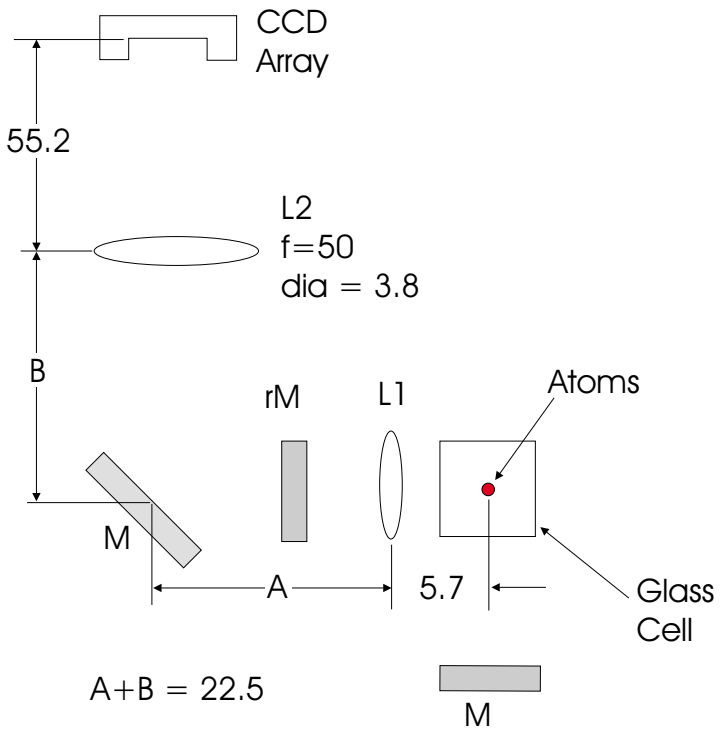


Figure 2.1: Optical System for imaging Bose Condensates. Adding a second lens and moving the first lens L1 (focal length = 6 cm, diameter = 2.5 cm) closer to the atoms we increased our magnification and improved our resolution limit. The new position required a MOT alignment with lens L1 in the MOT beam and placed one focal length from the retromirror and quarter-wave plate (rM$\lambda$). For probing in the magnetic trap, (rM$\lambda$) was rotated out of the probe light path to permit light to reach the CCD array. All dimensions in cm. M$\lambda$ = retromirror and quarter-wave plate; M = mirror; L = lens.

## 2.4 Measurements of the Interaction Energy

The ballistic expansion we employed to facilitate imaging also gave us a way to measure the mean energy of the cloud. When we suddenly turn off the trap potential, the harmonic oscillator energy $E_{HO}$ vanishes. By energy conservation, the kinetic energy plus the self interaction energy of the condensate then appear in the form of purely kinetic energy $E$ of the expanding cloud. By varying the frequency of the trap and the number of atoms, we measured this energy as a function of interaction strength. According to the virial theorem, if the particles were ideal then $E$ would equal half the total energy. However, for a system with repulsive interactions the energy per particle due to $E_{int}$ can be non-negligible and $E \geq \frac{1}{2}E_{\rm tot}$.

We approached the zero-temperature limit described by the Gross-Pitaevskii Equation (eq.(2.1)) by evaporatively cooling to a point where the non-condensate component was no longer observed, corresponding to $T/T_0 < 0.5$ and $N_0/N > 0.8$. Exact temperature and condensate fraction for these deeply evaporated condensate clouds was difficult to determine because no non-condensate atoms were seen. We evaporated to BEC in the 373 Hz trap, then adiabatically ramped the trap fields to reach a new trap frequency and change the strength of interaction in the condensate. We released the condensate from this new trap by suddenly turning off the magnetic fields. In practice, a weak magnetic trap remains which served to support the atoms against gravity to allow longer expansion times. The effect of this remaining field on the expansion was calculated as always less than 6% and was accounted for in the analysis. We checked that our release of the atoms was purely non-adiabatic by expanding uncondensed clouds, with $T/T_0 \approx 1.3$ from different frequency

traps. We observed that the expanded clouds are symmetric and found that, for axial trap frequencies from 130 to 870 Hz, the energy expressed in units of trap frequency, $E/Nh\nu_r$, was constant to within 5%, as expected for classical clouds in the non-interacting limit.

We performed expansions of condensates for the same range of trap frequencies. In this experiment, each energy measurement consisted of typically ten pictures of condensates taken for different expansion times. We fit the data twice, using the two different limiting cases for the functional form - the Gaussian of a non-interacting condensate and a parabolic surface for a strongly interacting condensate in the TF limit. At short expansion times, the cloud widths changed non-linearly with time as $E_{int}$ was transformed into the pure kinetic energy of the cloud. At long expansion times we performed a linear fit to the expanded cloud widths to obtain the mean axial and radial velocities (see inset to Fig.2.2), from which we calculated the total energy $E$.

Fig.2.2 contains condensate expansion data for $N \approx 4200$ (circles), 2100 (triangles), and 800 atoms (square) released from traps having axial frequencies from 130 to 870 Hz. By using the product $N\sqrt{\nu_r}$ as the dependent variable we combined our different number and trap frequency data into one figure. From the trap asymmetry $\lambda = \sqrt{8}$ the measured kinetic energy was expected to be $\approx 1.207$. Note that the energies measured with parabolic fits for the most weakly interacting clouds were inconsistent with the energy in the non-interacting limit. The parabolic surface fits yielded lower energies than the Gaussian fits for all interaction strengths. We compared our measured condensate energy, as a function of interaction strength, with the theoretical prediction of Dalfovo and Stringari, who used the standard Gross-Pitaevskii theory to calculate the energy of the condensate in the zero-temperature limit

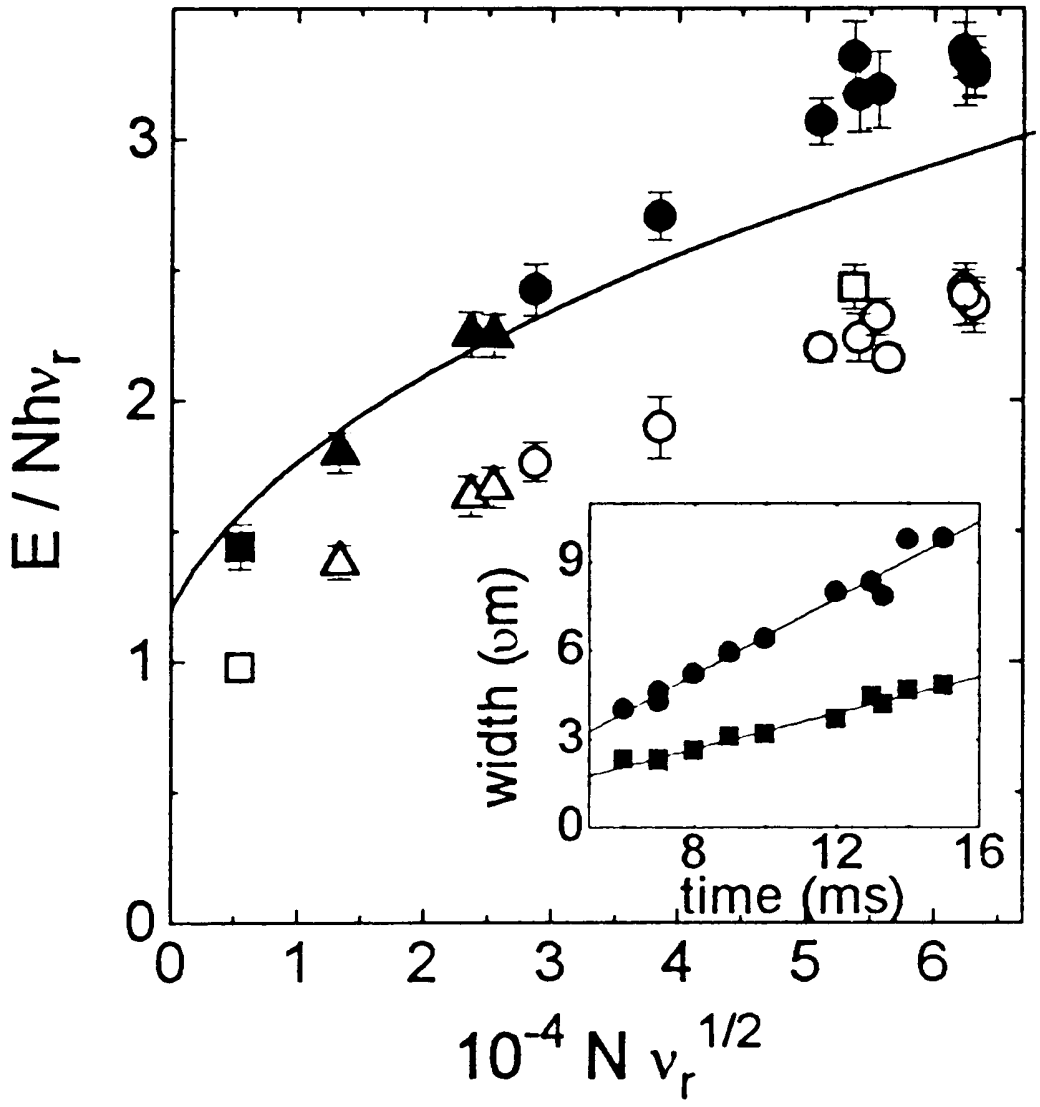


Figure 2.2: We measured the condensate energy as a function of effective interaction strength of $N\sqrt{\nu}$. The expansion velocity, and therefore energy, was obtained from a linear fit to the time-dependent widths of freely expanding condensates (inset). The widths were obtained from fits to either a Gaussian (solid shapes) or a parabolic surface (open shapes), as discussed in the text. The condensates contained $\approx 4200$ (circles), $\approx 2100$ (triangles) or $\approx 800$ (squares) atoms. The solid line shows the mean field prediction by Dalfovo and Stringari [5], which agrees well with the Gaussian fit data. Figure taken from Ref.[6].

[5]. The solid line in Fig.2.2 shows the prediction using the current best value of the scattering length for ground-state $^{87}$Rb atoms, $a = 110a_0$, where $a_0$ is the Bohr radius [108, 131]. Unlike results presented by Mewes **et al.** [121], the theory curve has no free parameters. Our energy data, measured from Gaussian fits, agrees reasonably well with the mean-field theory results.

## 2.5 Conclusions

Through several improvements in the original BEC apparatus we were able to perform quantitative studies of the interaction energy present in Bose condensates. For the data described here, Gaussian fits to the expanded clouds yielded condensate energies that are more in agreement with the predictions of a Gross-Pitaevskii mean-field theory than fits with paraboloids. Nonetheless, even the condensate energies derived from Gaussian fits are systematically higher than the theory, for the largest interaction strengths. For the regime of strong interactions, a parabolic surface should be a better approximation to the condensate density. A quantitative reconciliation between our data and the results of mean-field theory was achieved by Holland, *et al.* [7]. Using a mixed distribution to fit the condensate, consisting of a central parabolic surface and a Gaussian distribution in the periphery, they obtained good quantitative agreement between the measured expansion energies and energies predicted from mean-field theory (see Figure 2.3).

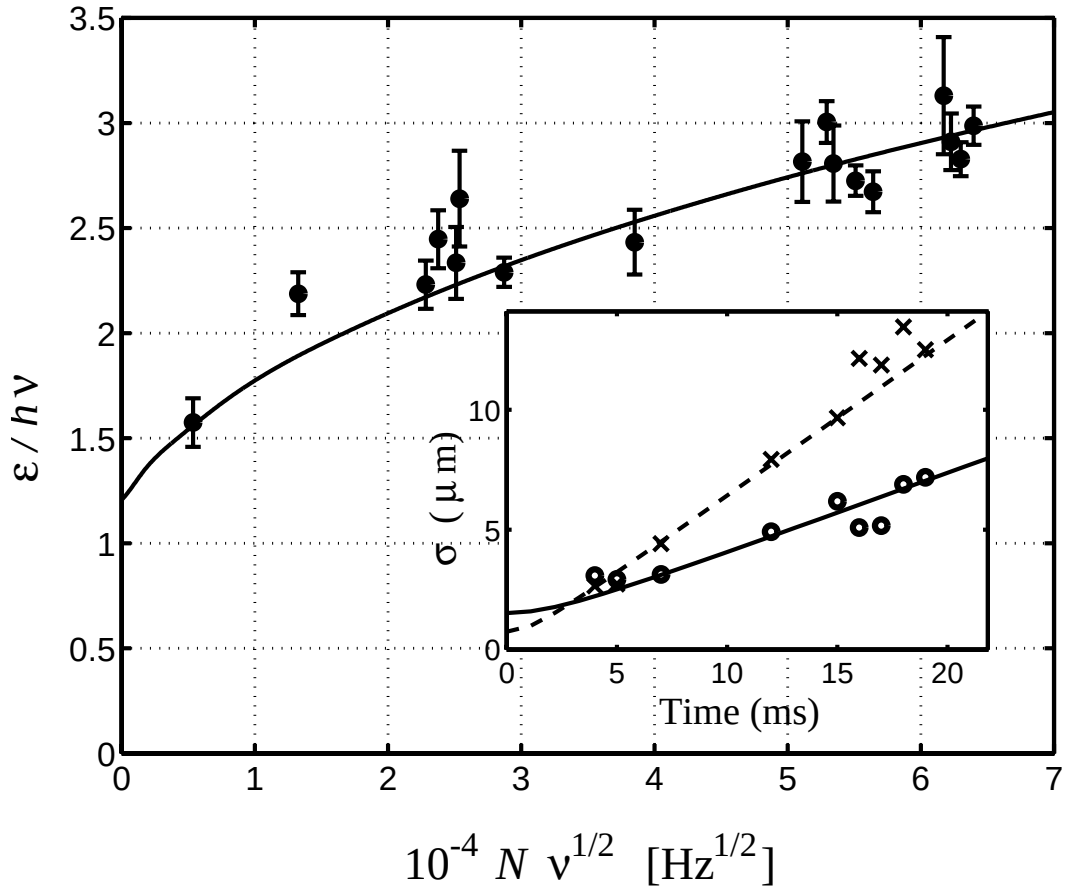


Figure 2.3: Comparison of the release energy as a function of interaction strength from mean-field theory (solid line) and the experimental measurements (•). Inset shows experimental widths in the horizontal (○) and vertical (×) directions against the mean-field predictions (dashed and solid lines) for the data point at $10^{-4}N\nu^{1/2} = 0.53$ Hz$^{1/2}$. Used with permission of M. Holland from Ref.[7].

# Chapter 3

# Collective Excitations of a Bose-Einstein Condensate in a Dilute Gas

## 3.1 Introduction

Early experiments with BEC showed that interatomic interactions influence the energy and wavefunction of a zero-temperature condensate [121, 6]. Using simple Gaussian or paraboloid models of the density distribution of the condensate, we observed good qualitative agreement between our energy data and the predictions of the Gross-Pitaevskii mean-field theory [124, 125, 126]. Unfortunately, the model profiles fit the subtle features of the condensate profile too crudely, and thereby compromised a quantitative and detailed test of theory. Gross-Pitaevskii theory also makes predictions for the existence of elementary condensate excitations [9, 10, 11, 12, 134, 135]. Such time-dependent behaviour was more amenable to a precise measurement since it was easier to measure a frequency accurately than to determine the absolute features of the density profile. We report herein on studies of low-energy, collective excitations of a dilute condensate of $^{87}$Rb. Characterizing these low-lying excitations was a first step towards understanding the dynamics of this novel quantum fluid [136].

## 3.2 Experimental Procedure

The apparatus and procedures for creating and observing BEC were the same as used in Section 2.3. For the experiments described here, the final evaporation took place in a trap with a radial frequency of 132 Hz (373 Hz axial). To approach the zero-temperature limit, we evaporated well below the BEC phase transition [137] so that the expanded clouds showed no sign of having a thermal component. At higher temperatures, this component appeared as a broad, symmetric Gaussian background [22]. Typically we had $4500 \pm 300$ atoms in the condensate.

## 3.3 Theory of Excitations

The standard theory for BEC in a dilute atomic vapor uses a nonlinear Schrödinger equation, the Gross-Pitaevskii equation, to describe the condensate wavefunction in the limit of zero temperature [138]. This equation comes from a second-quantized mean-field theory with the interatomic interactions modeled by an s-wave scattering length. The elementary excitations of BEC in a finite, harmonically-confined dilute gas were studied theoretically using this model [9, 10, 11, 12, 134, 135]. The lowest energy normal modes of the condensate, corresponding to rigid-body center-of-mass motion ("sloshing"), were predicted to occur at the trap frequencies. The frequencies of the next lowest condensate excitation modes, however, were expected to deviate from the spectrum of a cloud of ideal gas, for which the excitation frequencies are simply multiples of trap frequencies. Not surprisingly, the amount of deviation depends on the strength of the interatomic interactions.

## 3.4 Exciting collective modes

We excited these collective modes of the condensate by applying a small time-dependent perturbation to the transverse trap potential. We generated the perturbations by applying a sinusoidal current to the coils responsible for the rotating field of our TOP trap (in addition to the normal TOP currents). The response of the condensate depends on the symmetry of the driving force as well as the driving frequency, $\nu_d$. By appropriately setting the phases of the currents through the coils, we generated perturbations with either of two different symmetries. We label these two driving symmetries $m = 0$ and $m = 2$, where $m$, the angular momentum projection onto $\hat{z}$, is a good quantum number because of the axial symmetry of our unperturbed magnetic trap. Equipotential contours for the two trap perturbations are shown in Fig. 3.1. The $m = 0$ drive preserved axial symmetry and corresponds to an oscillation in radial size. For the $m = 2$ drive symmetry, the trap spring constants along $\hat{x}$ and $\hat{y}$ were modulated 90° out of phase. This corresponded to a normal mode resembling a transverse ellipse whose major axis rotates in the $x - y$ plane.

The basic spectroscopic approach was as follows: we distorted the cloud by applying the perturbative drive for a short time, then allowed the cloud to evolve freely in the unperturbed trap for a variable length of time. Finally, we turned off the confining potential suddenly and imaged the resulting cloud shape after 7 ms of free expansion.

## 3.5 Observation of Excitations

Initial studies were made in a 132 Hz trap. The perturbative drive pulse duration was 50 ms, the center frequency was set to match the frequency

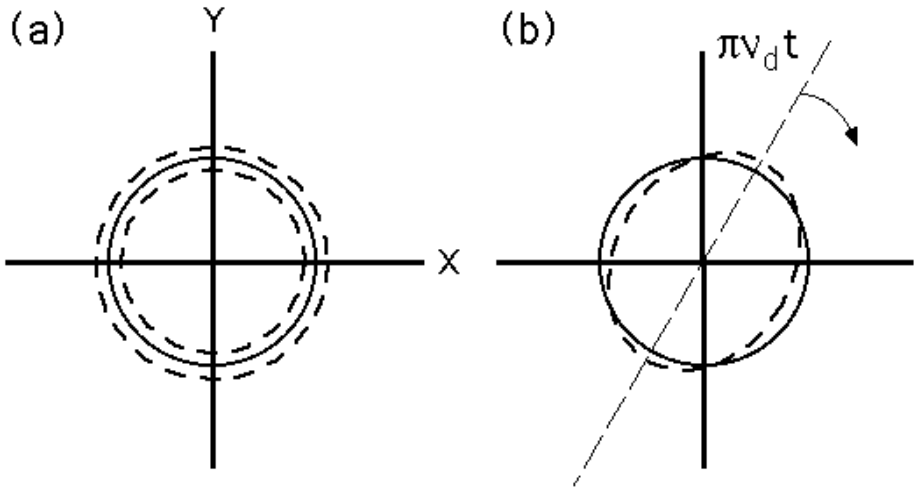


Figure 3.1: In the unperturbed trap, contours of equipotential in the transverse plane are symmetric (solid line). To drive the $m = 0$ excitation ($a$) we applied a weak harmonic modulation with frequency $\nu_d$ to the trap radial spring constant. The $m = 2$ drive ($b$) broke axial symmetry with elliptical contours which rotate at $\nu_d/2$. The amplitude of perturbation is shown exaggerated for clarity. Figure taken from Ref.[8].

of the excitation being studied, and the amplitude was 1.5% of the radial spring constant of our trap. We observed two different collective excitations of the condensate. The observables in both cases were the widths of the expanded clouds as a function of the free evolution time. In one case we observed a sinusoidal oscillation of the radial width at a frequency of $(1.84 \pm 0.01)\nu_r$, where $\nu_r$ is the radial trap frequency and the error quoted reflects only statistical uncertainties. This mode was driven by the axially symmetric $m = 0$ trap perturbation and was not observed for the drive with $m = 2$ symmetry (with the same drive amplitude and frequency). The cloud widths oscillated in both axial and radial directions, with approximately opposite phase. This response is shown in Fig. 3.2. The observed phase difference between the oscillations of axial and radial widths is not exactly $\pi$; however, the free expansion of the condensate prior to imaging complicates analysis of this phase shift [139]. The second excitation oscillated freely at $(1.43 \pm 0.01)\nu_r$, and appeared in response to a $m = 2$ drive, and not to a $m = 0$ drive. In this case, the radial width oscillated, with no observable response in the axial width. The two-dimensional projection of an ellipsoidal cloud whose major axis rotates in the transverse plane would exhibit this behavior.

We calibrated the observed excitation frequencies in units of the trap frequencies by making similar measurements on non-condensate clouds. The temperature of these clouds, in units of the BEC transition temperature, is $T/T_c \approx 1.3$; consequently the density and thus the interactions were very small. Here, we saw a response that oscillated at 264 Hz and was driven with either symmetry. A harmonically confined, noninteracting gas pulses at twice the radial trap frequency, so this gave $\nu_r = 132 \pm 1$ Hz. We also checked that the thermal cloud did not respond when driven at $1.43\nu_r$.

## 3.6 Effect of Interactions

In the s-wave scattering approximation, the interactions for ground state $^{87}$Rb atoms in our trap are repulsive (positive scattering length) [108, 131], providing an effective potential energy which favors a lower central density of the condensate compared to the non-interacting case. This interaction energy determines the excitation spectrum of the condensate [140]. We were able to examine this effect because BEC in trapped neutral atoms offers the advantage of an adjustable interaction energy. In the standard mean-field picture, the strength of the non-linear interaction term in the Gross-Pitaevskii equation, relative to the harmonic trap's energy-level spacing, scales with $Na\sqrt{\nu_r}$ for the regime of interactions in which the ground-state density is well-approximated by a Gaussian [128, 129, 130, 5]. Thus, by varying the trap frequency or the number of atoms, $N$, we changed the relative importance of interactions in the condensates.

We measured the excitation frequencies of the $m = 0$ and $m = 2$ modes of the condensate as a function of both $N$ and $\nu_r$. In the 132 Hz trap, we changed the relative interaction strength by reducing the number of atoms. To change $\nu_r$, we evaporated to BEC in the 132 Hz trap, then adiabatically ramped the trap fields until the condensate was held in a trap with an axial frequency of 43.2 Hz. In this lower frequency trap, we excite the condensate with a 100 ms pulse and a drive amplitude equal to 3% of the radial spring constant. The observed fractional amplitude of the oscillations in the cloud width was typically 11% of the mean width for this drive. We measured the free oscillation frequency of the $m = 0$ and $m = 2$ modes in this trap to be $(1.90 \pm 0.01)\nu_r$ and $(1.51 \pm 0.01)\nu_r$, respectively, for $N \approx 3000$.

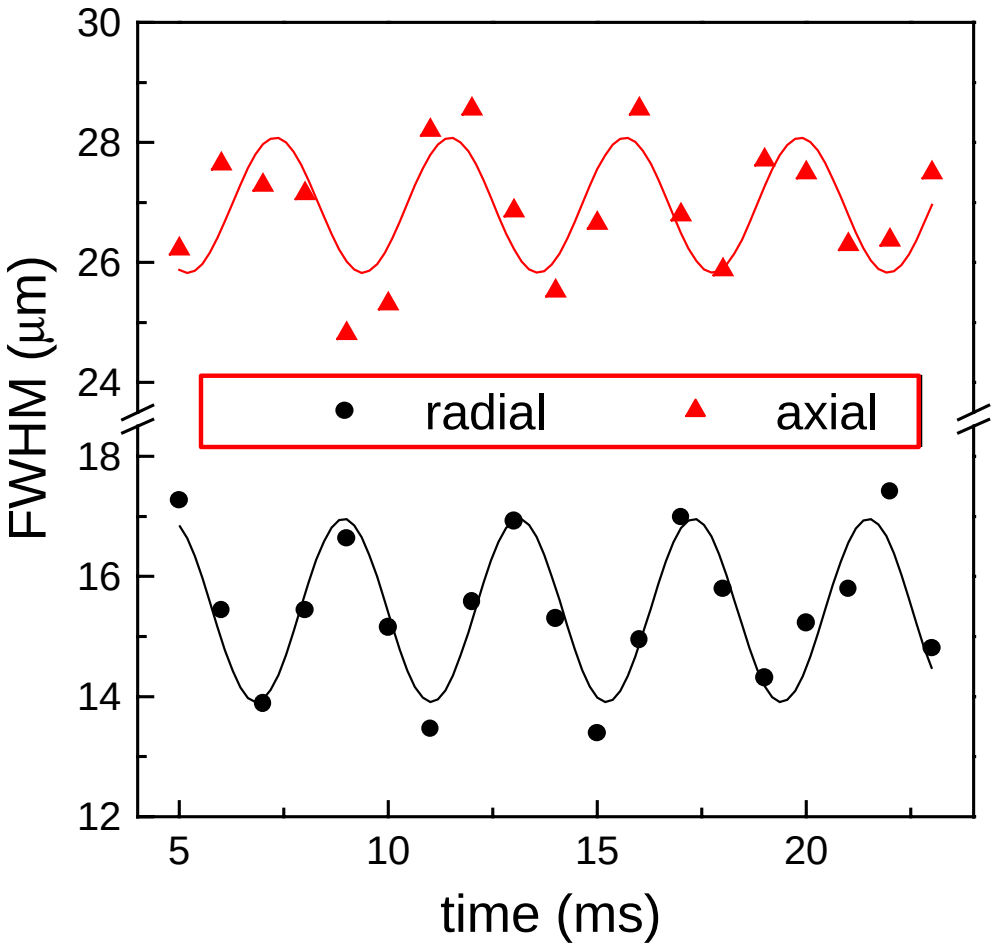


Figure 3.2: We applied a weak $m = 0$ drive to a $N \approx 4500$ condensate in a 132 Hz (radial) trap. Afterward, the freely evolving response of the condensate showed radial oscillations. Also observed is a sympathetic response of the axial width, approximately 180° out of phase. The frequency of the excitation was determined from a sine wave fit to the freely oscillating cloud widths. Each data point represents a single destructive condensate measurement. Figure taken from Ref.[8].

The measured excitation frequencies as a function of interaction strength are shown in Fig. 3.3. By using the product $N\sqrt{\nu_r}$ for the dependent variable we combine our different number and trap frequency data into one graph. The solid lines in Fig. 3.3 show the mean-field theory calculation by Edwards *et al.* [9, 10], using the best value of the scattering length for ground state $^{87}$Rb atoms available at the time, $a = 110a_o$ [108], where $a_o$ is the Bohr radius. An extension of this calculation by Esry and Greene is shown with dotted lines [11]. Finally, dashed lines indicate the prediction by Stringari for the "strongly interacting" limit [12], in which the kinetic energy of the ground state is ignored. Our data agreed reasonably well with these mean-field theory results; the measured energies of the low-lying collective excitations of the condensate deviate from the simple harmonic trap spectrum as predicted, with larger deviation for larger interaction strength. Error bars in Fig.3.3 indicate statistical error in the determination of the frequencies, but do not include possible systematic errors such as day-to-day variations in the trap magnetic fields, and therefore frequencies (estimated to be less than 0.5%). A significant systematic also arose from our method of using the $m = 0$ non-condensate mode to calibrate the trap frequency: Measurements of finite temperature excitations [141] indicated this caused our measured excitation frequencies to be low by 1%. Also, the theoretical curves are strictly valid only in the limit of zero temperature and zero amplitude.

In the limit of low excitation amplitude, the spectrum of low-lying collective excitations corresponds exactly to the Bogoliubov quasi-particle spectrum [9, 10]. The collective condensate response to our trap perturbation, in the limit of low amplitude, is simply a coherent state of these elementary excitations. To explore the question of whether or not our experiments were

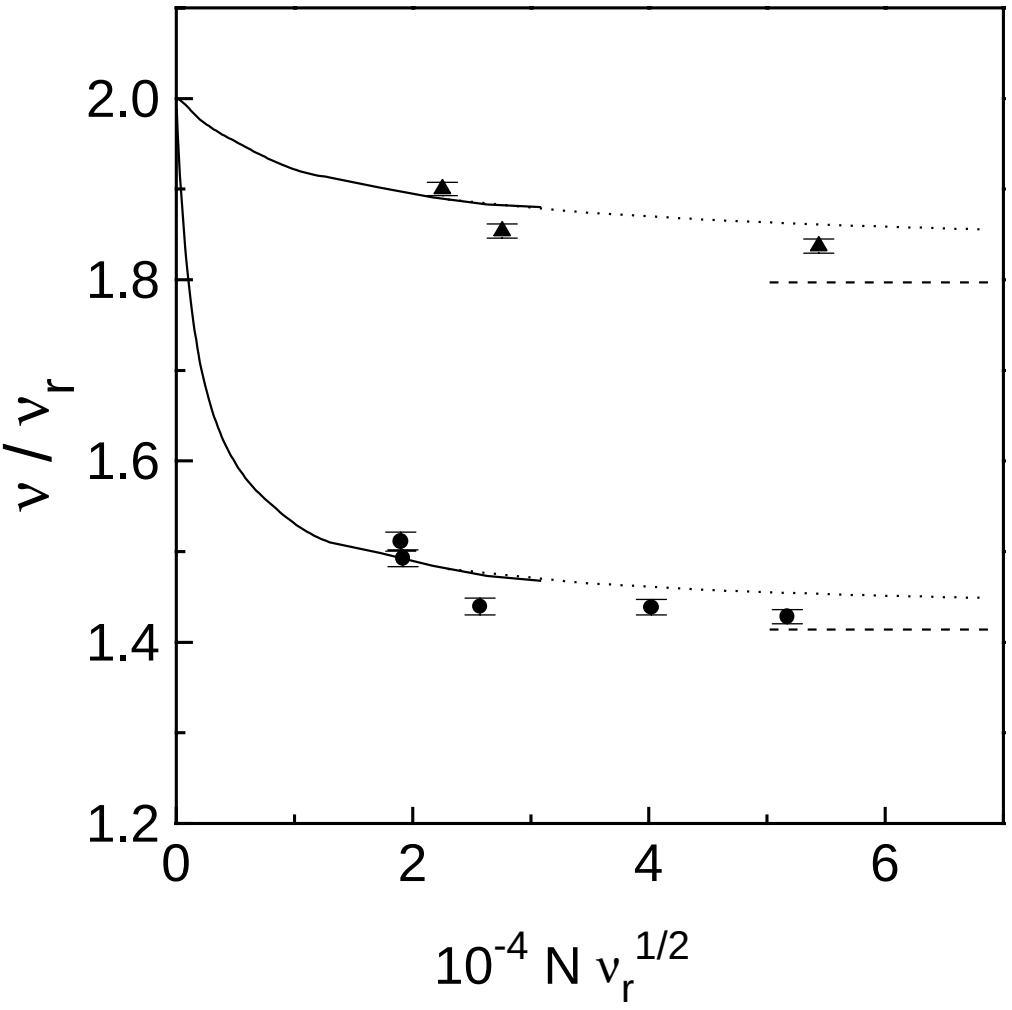


Figure 3.3: We measured the frequency of the $m = 0$ (triangles) and $m = 2$ (circles) condensate modes as a function of interaction strength. The relative interaction strength in the condensate varied as the product of number of atoms, $N$, and the square root of the radial trap frequency, $\nu_r$. Solid lines show the mean-field calculation by Edwards and co-workers [9, 10], dotted lines show the results of similar calculations by B. Esry and C. Greene [11] and dashed lines show the prediction by Stringari for the strongly-interacting limit [12]. Figure taken from Ref.[8].

performed in this limit, we measured the condensate response for different driving force amplitudes. In this test, we drove the $m = 2$ mode in the 132 Hz trap, with $N \approx 4500$. The results are shown in Fig. 3.4 where we plot the frequency of the oscillating radial width as a function of the amplitude of that response. The solid line shows a fit to a parabola, a form which describes an oscillator with anharmonic terms. As our measurements of excitation frequency were performed for a response amplitude between 9 and 14%, which caused a shift of only 1% in the frequency, this data suggests that we are in the regime where the measured spectrum corresponds quite closely to the elementary excitations of BEC in a dilute gas.

## 3.7 Damping

Finally, we examined the damping of a condensate excitation. For comparison purposes we first studied the damping in a noncondensed thermal cloud ($T/T_c \approx 1.3$) in the 132 Hz trap. We excited the 264 Hz $m = 0$ mode, because damping in this mode is not influenced by angular momentum conservation. We fit a sine wave with an exponentially decaying amplitude to the observed oscillations in the radial cloud width. This gave an excitation lifetime of $49 \pm 13$ ms. Since the mean free path in these clouds is long compared to the excitation wavelength and the effect of the trap anharmonicity is small, the excitation lifetime should scale inversely as the atom-atom collision rate. This rate in turn scales with the product of the density times the velocity of the atoms. For a given harmonic oscillator confining potential, this collision rate is proportional to the optical depth of the cloud. Using this scaling principle we predicted that the damping lifetime in a classical cloud with the same optical

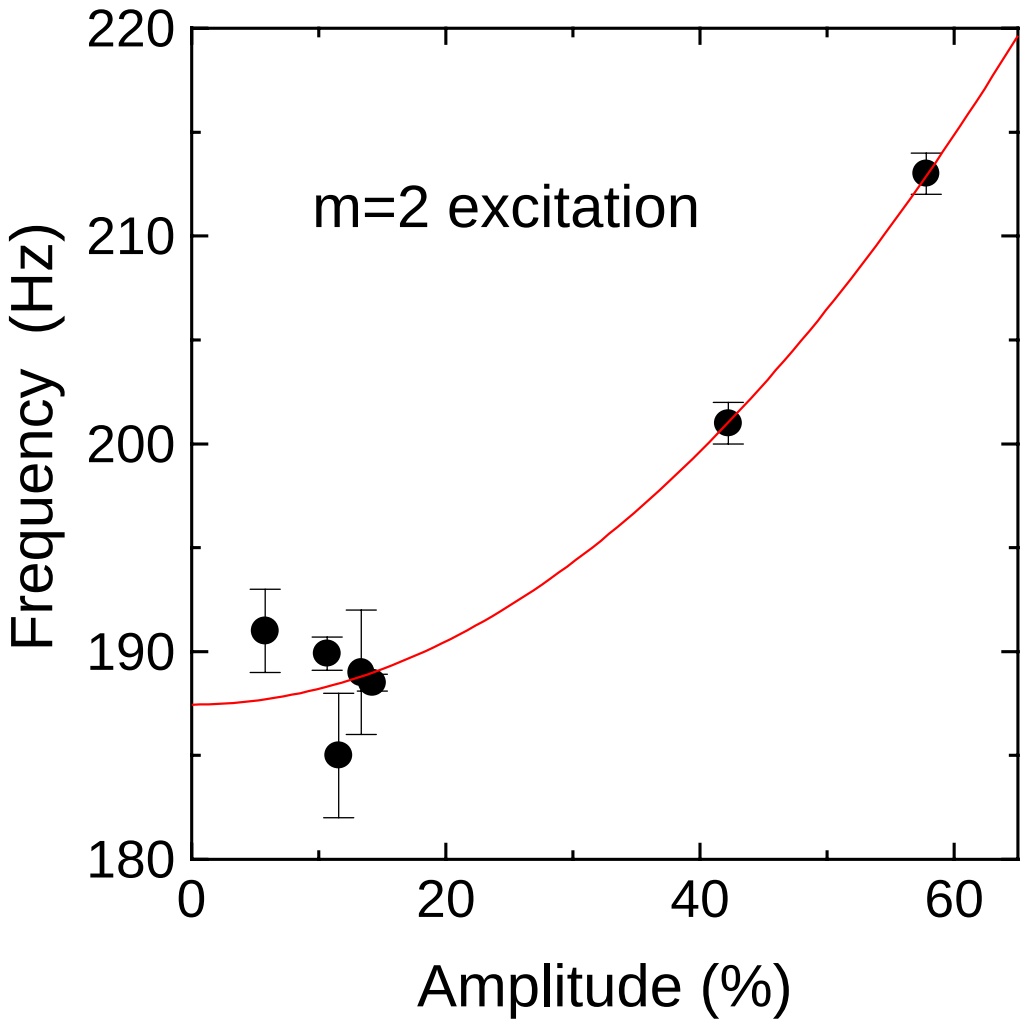


Figure 3.4: The freely oscillating frequency of the condensate is shown as a function of response amplitude. The condensates, consisting of 4500 atoms, were held in a 132 Hz radial frequency trap and driven with $m = 2$ symmetry. The solid line shows a parabolic fit to the data. Figure taken from Ref.[8].

depth as the condensate would be $28 \pm 8$ ms.

But when we performed the same experiment on the 4500 atom condensate we obtained an excitation lifetime of $110 \pm 25$ ms. Thus, the condensate excitation persisted nearly four times longer than can be explained in a classical picture.

In summary, we observed low-lying collective excitations of BEC in a dilute atomic vapor. Both $m = 0$ and $m = 2$ modes were identified, and their frequencies measured as a function of relative interaction strength. The data were taken in a linear regime where the collective modes should correspond to the elementary excitations of BEC in this system, and reasonable agreement was found between the experiment and mean-field theory results. The damping lifetime of the $m = 0$ excitation was measured and found to be significantly longer than the prediction of a classical model. We believe further study of these elementary excitations, particularly at different temperatures, will help deepen the understanding of the quantum phenomena of Bose-Einstein condensation of a gas.

# Chapter 4

# Bose-Einstein Condensation in a Dilute Gas: Measurement of Energy and Ground-State Occupation

## 4.1 Introduction

The ability to create Bose-Einstein condensation (BEC) in magnetically trapped alkali gases [22, 119, 142, 122] provided an opportunity to experimentally study the thermodynamics of bosonic systems in which the interactions are (i) weak, (ii) binary and (iii) experimentally adjustable [8, 121, 6]. One goal of experimental and theoretical work in this field was to understand a variety of low-temperature phenomena from both macroscopic and microscopic points-of-view, with a quantitative reconciliation of these two approaches. The experimental studies of collective excitations of zero-temperature condensates ( [8, 143] and Chap. 3). were a step in this direction. The purpose of the present chapter is to explore the nature of the BEC phase transition by performing quantitative measurements of BEC in a different regime – near the critical temperature [144].

In this chapter we analyze a series of images of ultra-cold clouds of rubidium gas to determine the critical temperature and to extract ground-state occupation and total energy as a function of temperature. Total energy (or its derivative, specific heat) has a certain historical significance because it

was Fritz London's comparison [38] of the specific heats of liquid helium and an ideal Bose gas that began the rehabilitation of BEC as a useful physical concept. Moreover, measurements of thermodynamic quantities such as specific heat are essential in studying any phase transition. Ground-state occupation and critical temperature of a Bose gas are interesting because in liquid helium the former is very difficult to measure, while the latter is almost impossible to calculate accurately.

## 4.2 Experiment

The apparatus and procedures for creating BEC were the same as used in Sections 2.3 and 3.2. The imaging procedure used here differs in two specific ways. First, the atoms were always allowed to expand freely for a time of 10 ms before probing by the resonant probe beam. Secondly, we applied point-by-point corrections for imperfect polarization and saturation effects in our digital analysis to render the true 2-d projection of the velocity distribution in the expanded cloud.

## 4.3 Data Analysis

These distributions contain a wealth of thermodynamic information. For instance, the integrated area under the distribution is proportional to the total number, $N$, of atoms in the sample. The condensate appears as a narrow feature centered on zero velocity [22]; the number of atoms in the ground state, $N_o$, is then proportional to the integrated area under this feature. From the mean square radius of the expanded cloud and the expansion time, we get the mean square velocity, or average energy, of the cloud. Finally, as discussed

below, the temperature, $T$, is extracted from the images, even though the temperature is not merely proportional to mean energy in a degenerate Bose cloud.

We went to some lengths to extract these thermodynamic quantities in a model-independent way. For instance, if we were to fit the observed velocity distributions to a Bose-Einstein distribution, we could hardly avoid coming to the conclusion that the specific heat is discontinuous - the singular behavior is built-in to the assumed functional form. Moreover, such a fit would preclude our being able to observe effects due to interactions, finite $N$, critical fluctuations, etc. Fortunately, useful thermodynamic information about the sample can be extracted from direct calculation of various moments of the velocity distribution, without specific reference to the nature of the distribution. The total number and energy of the atoms, as mentioned above, are simply proportional to the zeroth and second moments, respectively, calculated directly by summing over the velocity distribution images [145].

We defined the number of atoms in the ground state to be the number of atoms contributing to the narrow, central feature in the optical depth images [22]. To avoid biased and noisy results we provided the least-squares fitting routine with a tightly constrained template to use in its search for a condensate. With an independent set of measurements on condensates near zero temperature, we found that the condensate shapes were well-fit with 2-d Gaussians whose widths, aspect ratios and peak-heights, for a given trap frequency and expansion time, were functions only of the total number of atoms in the feature [6, 7]. The width, for instance, was parameterized by $\sigma = \sigma_o(1 + \alpha N_o)^{1/5}$, where $\sigma_o$ is the predicted non-interacting condensate width and $\alpha$ was extracted empirically. The procedure yielded robust values of $N_o$, as long as the temper-

ature was high enough that the non-condensate atoms formed a distribution that was significantly broader than the sharp condensate feature. At temperatures below $T/T_o = 0.5$, both $T$ and $N_o$ measurements became suspect as it was no longer possible to cleanly separate the condensate and the non-condensate components without recourse to a detailed model, which was contrary to the spirit of this treatment.

Our thermometry differed from previously reported methods for ultracold trapped gases [22, 119, 142, 8, 121, 6, 143]. For an ideal gas far from quantum degeneracy the velocity distribution is a Gaussian whose width is proportional to $T^{1/2}$. As the cloud is cooled closer to the BEC phase transition, higher densities and lower temperatures cause a rapid increase in the significance of quantum statistics and of residual atom-atom interactions. Rather than attempt to model these effects, we assumed that the high-energy tail of the velocity distribution (i) remained in thermal equilibrium with the rest of the cloud and (ii) was characterized by a purely ideal Maxwell-Boltzmann (MB) distribution. The latter is plausible because these highest energy atoms spend most of their trajectories in the low-density, and therefore weakly interacting, outer part of the trapped cloud. Furthermore, the occupation numbers of the corresponding energy states are much less than one. Finally, during the free expansion, the high-energy atoms underwent on average much less than one collision. Guided by these assumptions, we determined the temperature by fitting a 2-d Gaussian to only the wings of our velocity-distribution images, excluding the central part of the cloud, where degeneracy, interactions, fluctuations, etc. may be significant. To test the assumption of thermal equilibrium we checked that the measured temperature of clouds were independent of the size of the exclusion region, outside of the degenerate regime [146].

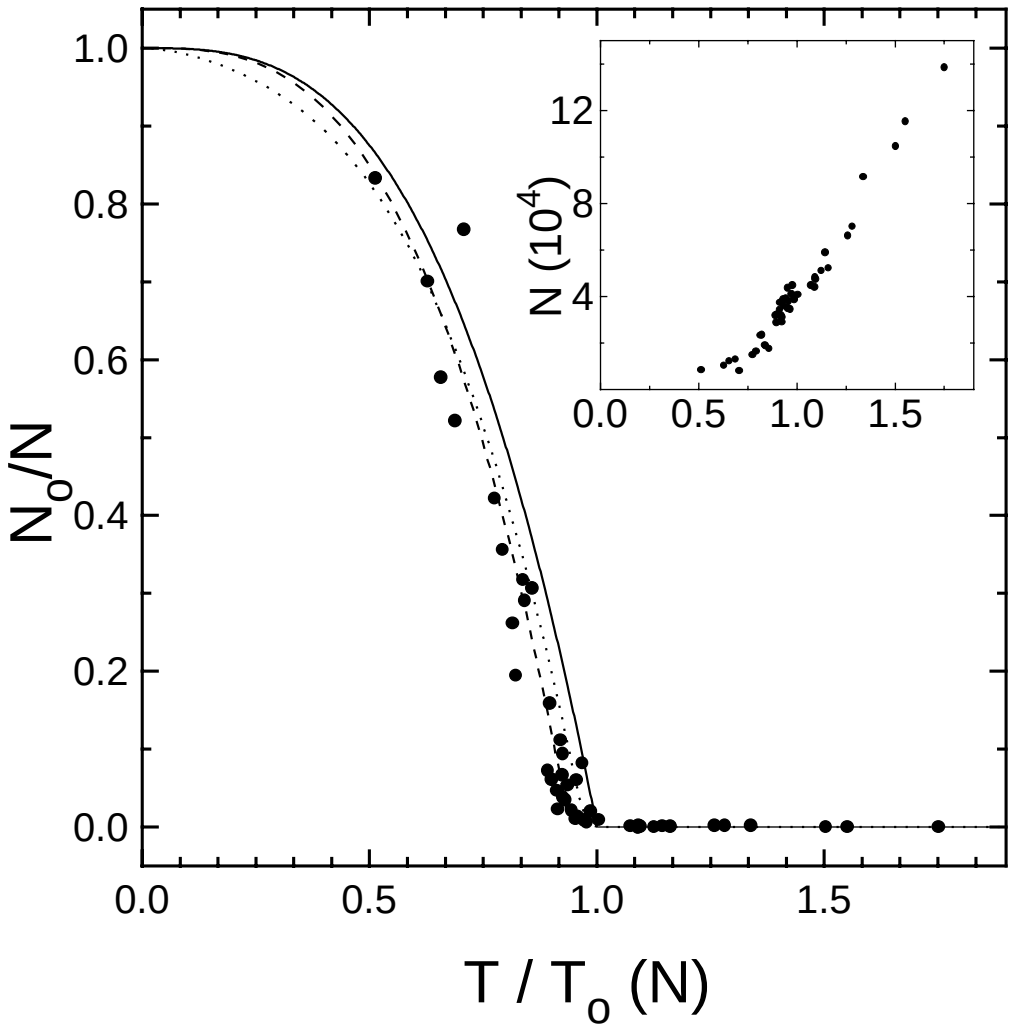


Figure 4.1: Total number $N$ (inset) and ground-state fraction $N_o/N$ as a function of scaled temperature $T/T_o$. The scale temperature $T_o(N)$ is the predicted critical temperature, in the thermodynamic (infinite $N$) limit, for an ideal gas in a harmonic potential. The solid (dotted) line shows the infinite (finite) $N$ theory curves. At the transition, the cloud consisted of 40,000 atoms at 280 nK. The dashed line is a least-squares fit to the form $N_o/N = 1 - (T/T_c)^3$ which gives $T_c = 0.94(5)T_o$. Each point represents the average of three separate images. Figure taken from Ref.[13].

## 4.4 Ground-State Fraction

The first quantity we examined is the ground-state fraction, $N_o/N$, as a function of scaled temperature $T/T_o$ (Fig. 4.1). The temperature scaling removed the trivial shift in the transition temperature which occurred because as we evaporatively cool through the transition we also reduced the total number of atoms, $N$ (Fig. 4.1, inset). We chose our scaling temperature to be $T_o(N) = \hbar\bar{\omega}/k_B(N/\zeta(3))^{1/3}$ where $\bar{\omega}$ is the geometric mean of the trap frequencies and $\zeta$ is the Riemann Zeta function. $T_o(N)$ is also the critical temperature, in the thermodynamic limit, for non-interacting bosons in a harmonic potential [147, 84]. For this case the temperature dependence of the ground-state fraction is $N_o/N = 1 - (T/T_o)^3$ below $T_o$ (solid line, Fig. 4.1). We emphasize that, in contrast with the recent work of Mewes *et al.* [121], this line contains no free parameters and was not fit to the data, and so comparing this line to our data provides a detailed test of theory.

From our data we found a critical temperature of $T_c = 0.94(5)T_o$. The uncertainty was dominated by the systematic uncertainty in our measurement of the scaled temperature stemming mostly from a 2% uncertainty in the magnification of our imaging system. Our measurements were thus only marginally different from the theory for non-interacting bosons in the thermodynamic limit. Finite-number corrections [14, 15] will shift the transition temperature $T_c(N)$ down about 3% (dotted line, Fig. 4.1). Mean-field [84, 148] and many-body [149] interaction effects may also shift $T_c(N)$ a few percent.

## 4.5 Energy

The second result we present is a measurement of the energy and specific heat. Ballistic expansion, which facilitates quantitative imaging, also provided a way to measure the energy of a Bose gas [121, 6, 8]. The total energy per particle of the trapped cloud consists of harmonic potential, kinetic, and interaction potential energy contributions, or $E_{pot}$, $E_{kin}$ and $E_{int}$, respectively. As the trapping field was non-adiabatically turned-off to initiate the expansion, $E_{pot}$ suddenly vanished. During the ensuing expansion, the remaining components of the energy, $E_{kin}$ and $E_{int}$, were then transformed into purely kinetic energy, $E$, of the expanding cloud: $E_{kin} + E_{int} \rightarrow E$, where $E$ is the quantity we actually measured. According to the virial theorem, if the particles are ideal ($E_{int} = 0$), $E$ will equal half the total energy, i.e. $E = 1/2E_{tot}^{ideal}$. However, for a system with interparticle interactions the energy per particle due to $E_{int}$ can be non-negligible and then $E = \alpha E_{tot}$, where $\alpha$ is not necessarily $1/2$.

The scaled energy per particle, $E/Nk_BT_o$, is plotted versus the scaled temperature, $T/T_o$, in Fig. 4.2. $E/N$ was normalized by the characteristic energy of the transition $k_BT_o(N)$ just as the temperature was normalized by $T_o$. The data shown were extracted from the same cloud images as those analyzed for the ground-state fraction. Above $T_o$, the data tended to the straight solid line which corresponded to the classical MB limit for the kinetic energy. Most interesting was the behavior of the gas at the transition. By examining the deviation, $\Delta$, of the data from the classical line we saw (Fig. 4.2, inset) that the energy curve clearly changed slope near the empirical transition temperature ($0.94T_o$) obtained from the ground-state fraction analysis discussed above.

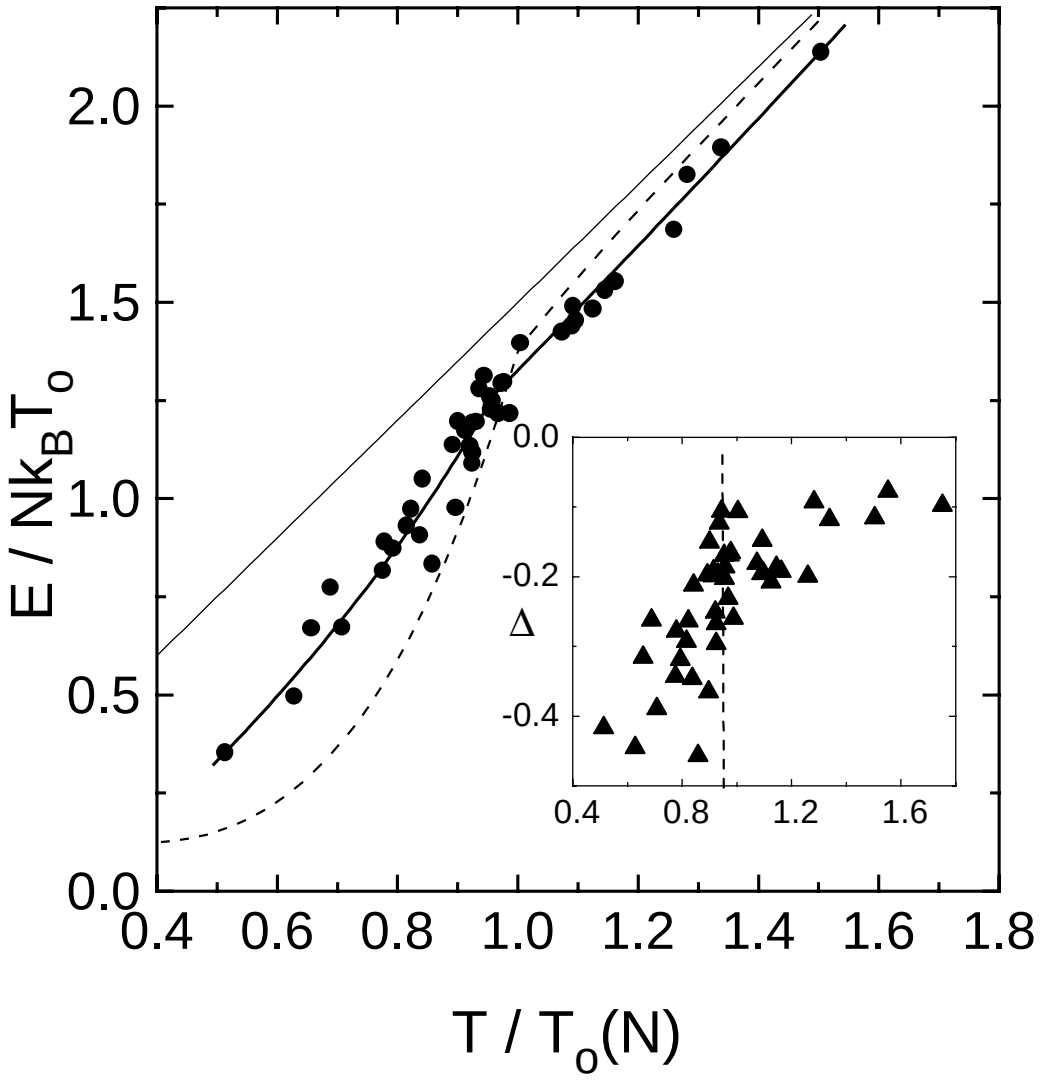


Figure 4.2: The scaled energy per particle $E/Nk_BT_o$ of the Bose gas is plotted vs. scaled temperature $T/T_o$. The straight, solid line is the energy for a classical, ideal gas, and the dashed line is the predicted energy for a finite number of non-interacting bosons [14, 15]. The solid, curved lines are separate polynomial fits to the data above and below the empirical transition temperature of $0.94T_o$. (inset) The difference $\Delta$ between the data and the classical energy emphasizes the change in slope of the measured energy-temperature curve near $0.94T_o$ (vertical dashed line). Figure taken from Ref.[13].

## 4.6 Specific Heat

The specific heat is usually defined as the temperature derivative of the energy per particle, taken with either pressure or volume held constant. In our case the derivative was the slope of the scaled energy vs. temperature plot (Fig. 4.2), with neither pressure nor volume, but rather confining potential held constant. To place our measurement in context, it is instructive to look at the expected behavior of related specific heat versus temperature plots (Fig. 4.3). The specific heat of an ideal classical gas (MB statistics), displayed as a dashed line, is independent of temperature all the way to zero temperature. Ideal bosons confined in a 3-d box have a cusp in their specific heat at the critical temperature (dotted line) [38]. Liquid $^4$He can be modeled as bosons in a 3-d box, but the true behavior is quite different from an ideal gas, as illustrated by the specific heat data [16, 17] (dot-dash line): the critical (or lambda) temperature is too low, and the gentle ideal gas cusp is replaced by a logarithmic divergence. We compared our data with the calculated specific heat of ideal bosons in a 3-d anisotropic simple harmonic oscillator (SHO) potential [147] (solid line). Note that because we did not measure $E_{pot}$, we had to divide the SHO theory values by two to compare with our measured expansion energies. The specific heat of the ideal gas is discontinuous and finite at the transition.

In order to extract a specific heat from our noisy data, we assumed that, as predicted, there was a discontinuity in the slope at the empirically determined transition temperature and fit the data to separate polynomials on either side of $T_c$ (curved, solid lines in Fig. 4.2). We extracted the specific heat curve shown in Fig. 4.3 (bold line in inset). The observed step in the specific

heat at the critical temperature was considerably smaller than predicted by a finite number, ideal gas theory [14, 15] (Fig. 4.3, inset, thin line). A more sensible comparison is to avoid taking the model-dependent derivative and instead to compare theory and experiment directly in the energy-temperature plot (Fig. 4.2). The major deviation between the data and the SHO ideal gas theory (dotted line) occurs at scaled temperatures of 0.85 and below. The difference is probably due in part to the effects of interactions. Mean-field repulsion will tend to increase the energy at a given temperature.

## 4.7 Summary and Epilogue

We measured the critical temperature, ground-state occupation and energy of a dilute Bose gas of $^{87}$Rb atoms. Our analysis was unique in that it did not rely on detailed models of the quantum degenerate cloud shape. We were thus able to examine the thermodynamics of the Bose gas in an unbiased and quantitative way. The measured ground-state fraction and transition temperature agreed well with the theory for non-interacting bosons. However, the qualitative features of the energy data are significantly different from the non-interacting theory.

Recent theoretical results [18, 150, 151] that consider the effects of mean-field interactions at finite temperature are in good agreement with our data. The theories adapt the standard Gross-Pitaevskii treatment [129, 5] to include the condensed and non-condensed components of the gas. Generally, mean-field interactions reduce the ground-state occupation and increase the energy per particle compared to the non-interacting Bose gas (in the thermodynamic limit) at the same temperature. A downward shift in the critical

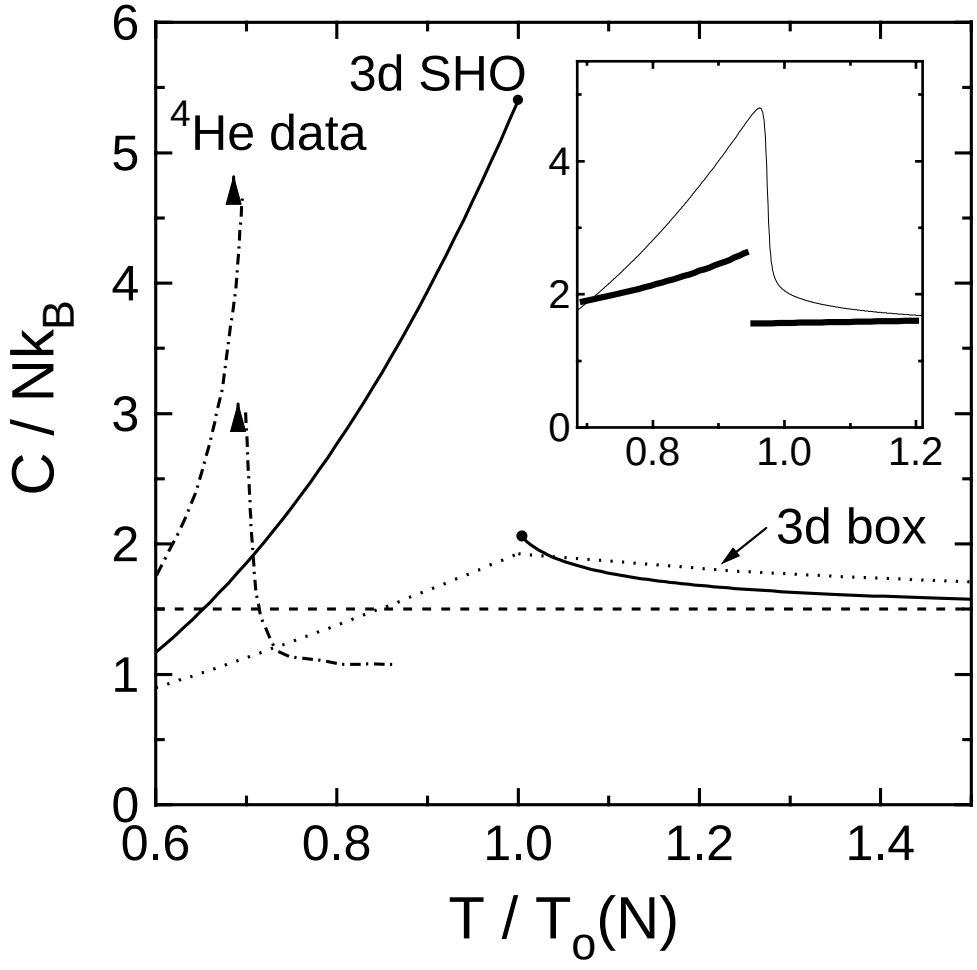


Figure 4.3: Specific heat, at constant external potential, vs. scaled temperature $T/T_o$ is plotted for various theories and experiment: theoretical curves for bosons in a anisotropic 3-d harmonic oscillator and a 3-d square well potential, and the data curve for liquid $^4$He [16, 17]. The flat dashed line is the specific heat for a classical ideal gas. (inset) The derivative (bold line) of the polynomial fits to our energy data is compared to the predicted specific heat (fine line) for a finite number of ideal bosons in a harmonic potential. Figure taken from Ref.[13].

temperature due to finite number and mean-field is also predicted. Our data for the ground-state occupation lie between the mean-field predictions and the ideal gas model [18, 151]. Due to systematic uncertainties in our temperature measurement, the differences between our measurements and the recent theory are marginal, however. The predicted energy per particle is in excellent agreement with our measurements (Figure 4.4), including the observation of a feature in the specific heat.

In future work we will attempt to elucidate the role interactions play in the phase transition and the specific heat. For example, we can control the interactions by adjusting the magnetic trap spring constants and changing the number of trapped atoms [8]. In addition, with larger clouds [122] we can reduce our uncertainty in $T_c$, allowing us to investigate finite-number and mean-field effects at the 1% level.

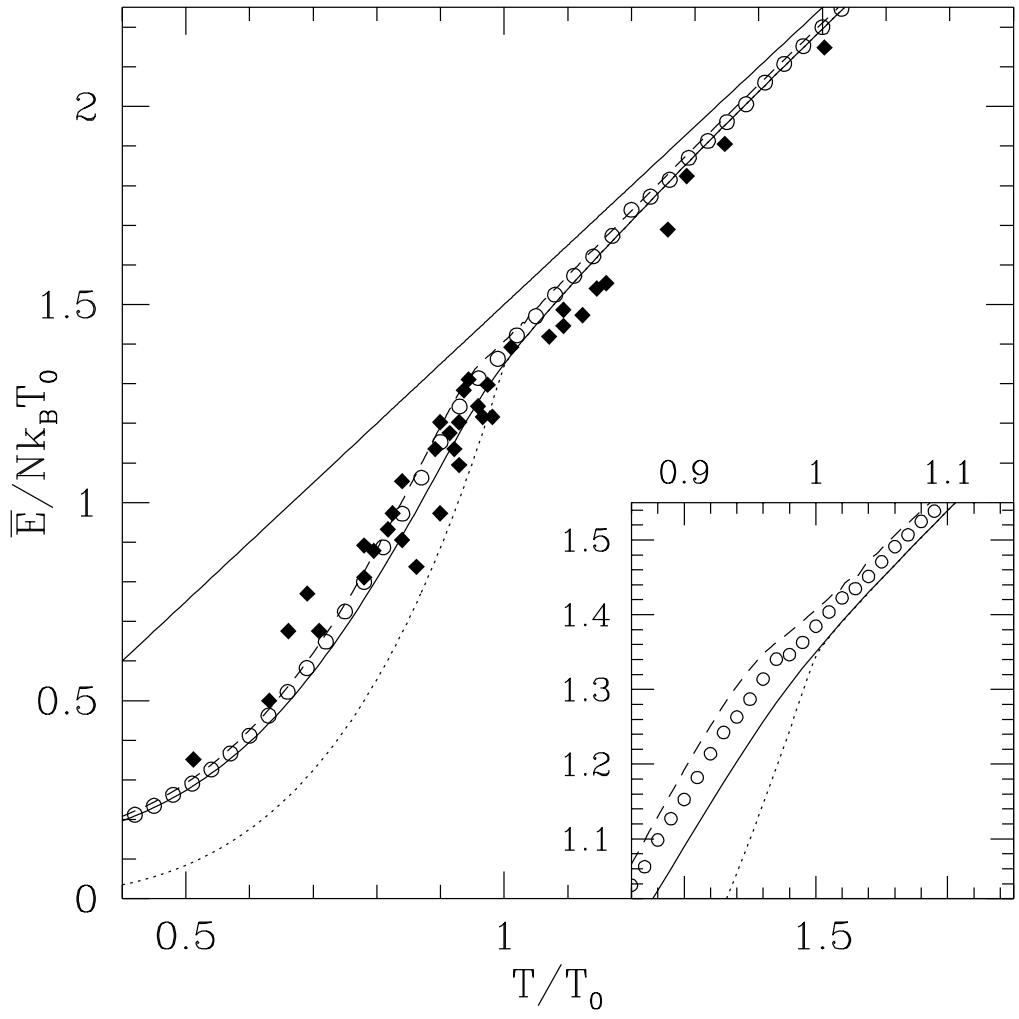


Figure 4.4: The sum of kinetic and interaction energy, as defined in the [18], obtained in the two-fluid model, compared with the data of Ensher *et al* [13] (diamonds) and with the ideal gas result (dotted curve). Results obtained from the zero-order solution (full curve), from the first-order perturbative treatment (dashed curve) and from the complete numerical solution (circles). The straight line is the classical Maxwell-Boltzmann result. The inset is an enlargement of the region around $T_c$. Figure taken from Ref.[18] with permission of S. Conti.

# Chapter 5

# The Third Generation BEC Machine at JILA

In this chapter I describe the latest and most sophisticated apparatus constructed at JILA to quickly ($1 - 1.5$ min) produce large BECs (typically $10^6$ atoms). The chapter focuses on experimental details ranging from fundamental design considerations to actual experimental conditions. The apparatus uses a double-MOT system to quickly load a purely magnetic trap in a low-background pressure environment, in which radio-frequency (rf) evaporative cooling is performed to reach BEC. I begin with a description of our vacuum system, followed by discussion of the Collection MOT (Magneto-Optical Trap), the Science MOT and the transfer of atoms from Collection MOT to Science MOT. Next, I discuss construction of the TOP magnetic trap, transfer from the Science MOT into the TOP magnetic trap and rf evaporation. The chapter concludes with a description of the absorption imaging system.

## 5.1 Vacuum System

The heart of the BEC apparatus is the double-MOT vacuum design first implemented by Myatt, *et al.* [93, 152]. The system uses a glass cell maintained at $10^{-9}$ Torr of Rb for rapid loading of a MOT with many atoms ($\sim 10^8$ atoms in $1-2$ sec). We refer to this as the Collection Cell and the MOT

it contains as the Collection MOT. A long transfer tube connects the Collection cell to a second glass cell maintained at much lower pressure ($10^{-11} - 10^{-12}$ Torr). The low-pressure cell, which we refer to as the Science Cell, allows long MOT and magnetic trap lifetimes. The Science cell is also designed for small magnetic field coils that create a high-confinement magnetic trap with minimized power dissipation. Finally, many windows with optical-quality glass allow for excellent access to the atoms in the Science Cell.

### 5.1.1 The Collection Cell

The collection cell is designed to collect a large number of atoms into a MOT simply and quickly. Two features are essential for rapid loading of the MOT with many atoms: large beam size and large amounts of trap light [153]. The high power laser used for trapping will be discussed in Section 5.2.1. The Collection cell accommodates large trap beams with six, 35 mm dia windows that provide access along each cardinal direction (Figure 5.1). Even larger windows would be beneficial, but the cost is a loss of simplicity. A larger glass cell requires larger coils and more amp-turns for the quadrupole potential of the MOT and the magnetic shim fields. At the present coil sizes, we supply enough current with simple 30V, 6A power supplies using air-cooled coils made from magnet wire. There is little heating of the glass due to the power dissipated from the coils. Another trade-off with large volume is the need for greater pump speeds.

Two other features of the Collection cell are worth noting. First, there are three, 10 mm diameter viewing windows. Two windows, facing opposite each other and perpendicular to the transfer tube axis, are used for monitoring atoms with a charged-coupled device (CCD) camera and a photodiode (PD).

The third window faces down the transfer tube and permits a laser pulse to push the MOT atoms down the tube. The second feature is the Rb metal dispenser used as a low-maintenance, high-flux source of atoms. Three dispensers are installed in each of two glass arms with vacuum feedthroughs, made of wire, leading to the dispensers. The dispensers emit Rb atoms, as discussed in Section 5.1.7.

### 5.1.2 The Science Cell

The Science cell (Fig.5.2) holds a large MOT of $> 10^9$ atoms, which we refer to as the Science MOT, yet is compact enough to keep magnetic field coils close to the atoms for high-confinement magnetic trapping. There are five main features of the Science Cell. (i) Six, 2.5 cm dia windows of good quality permit up to 2.5 cm dia MOT beams, which is necessary to contain a large number of atoms in the MOT. (ii) A "2-d" design of the cell, such that the cell is compact in the vertical direction, permits placement of quadrupole coils very near the atoms (for high magnetic field gradients). The small distance between cell windows in the horizontal directions provides more clear angles to the atoms and permits placement of the TOP coils nearer the atoms (for large magnetic fields). (iii) Three, 1 cm dia, high-quality windows in the horizontal plane permit clean optical probing and monitoring. One window, facing down the transfer tube, was initially used to align atom transfer and presently is used for a monitor PD. The other two windows, facing perpendicular to the axis of the transfer tube, are used for optically imaging the atoms. These latter two windows are 3.5 cm away from the atoms and create a window-defined $f/\#$ of 3.5. (iv) The glass arm that connects the Science cell to the transfer tube has two features. The length of the tube allows the main trap volume, at the center

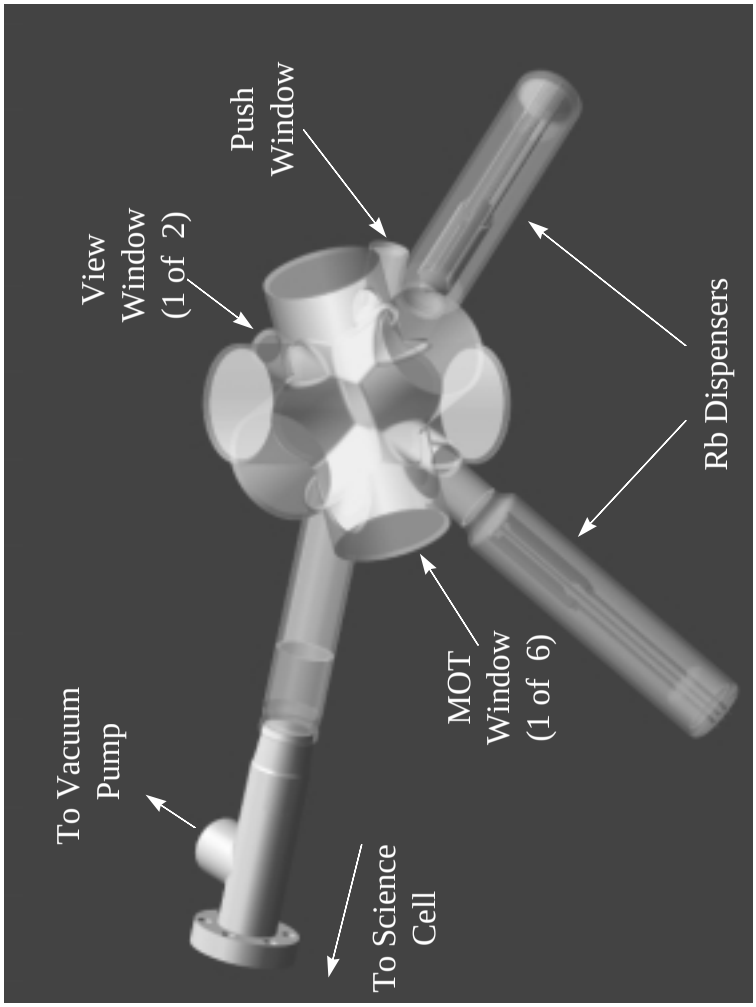


Figure 5.1: Schematic of the Collection Cell

of the large windows, to be far away from the magnetic fields of the transfer tube. The bellows-to-conflat connection reduces stress on the long glass arm and permits some degree of freedom in the construction of the vacuum system. (v) The 2.5 cm dia glass arm, which connects the Science cell to the large vacuum assembly, maintains a relatively high conductance path to the vacuum pump and the window at its end permits entry of one of the MOT beams into the cell. The length of the arm strikes a compromise between structural stability and the need to keep the vacuum apparatus away from the glass cell for more convenient placement of optics.

### 5.1.3 Transfer Tube

The transfer tube is a 37 cm long, 1.3 cm dia stainless steel tube that connects the Science cell to the Collection cell. Because the tube possesses a conductance of only 0.5 L/sec it maintains a large ($\approx 20\times$) differential pressure between chambers while allowing atoms to be optically pushed from Collection MOT to Science MOT. Near the Collection MOT, a short section of tube branches off the main transfer tube and connects the Collection cell to a 20 L/sec ion pump. Just beyond this branch is another short tube branch that contains a glass-encased magnet (the glass capsule is $\approx 3-4$ cm long). The magnet can be moved from outside the vacuum, using a solenoid, to obstruct the tube and effectively "valve-off" the two vacuum chambers. Along the entire length of the tube we inserted a spiral-wound wire that rests against the inside wall. The wire prevents shallow-angle scattering of light down the tube from the Collection MOT light, which would limit transfer efficiency by optically depumping the atoms from a magnetically trapped transfer state.

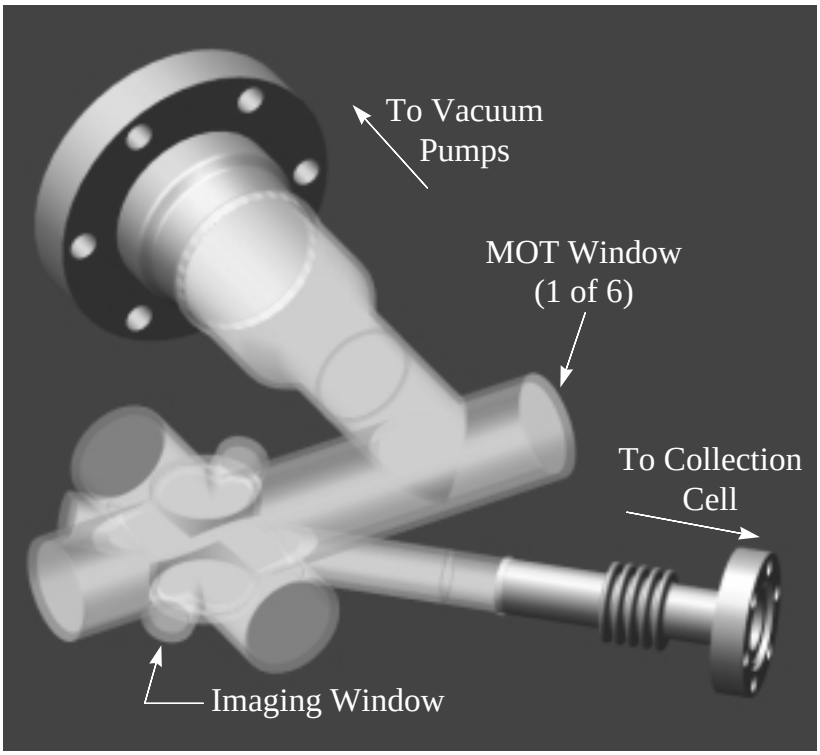


Figure 5.2: Schematic of the Science Cell

### 5.1.4 Pumps

We maintain sustained differential pressures between the Collection MOT and the Science MOT with two ion pumps on either end of the transfer tube. At the Collection cell end, we use a 20 L/sec ion pump that is actually overkill given the limited conductance to the Collection cell. The effective pump speed, at the cell, is only a few L/sec and the resulting pressure is of order $10^{-9}$ Torr. On the Science cell end, we are very concerned about maintaining high vacuum so we use a 30 L/sec ion pump and Titanium Sublimation Pump (TSP). The pumps are contained in a 4-way stainless-steel cross that is separate from the Science cell. The arms of the cross are 6.4 cm dia and provide a large surface area over which Titanium is periodically coated using sublimation from the TSP filaments. The entire cross is hence a passive ion pump. The large diameter arms also create a high conductance path from the 30 L/sec active ion pump to the glass cell for an effective pump speed at the cell of about 10 L/sec. On the fourth arm of the cross a bakeable mechanical valve is attached for the initial rough pump-down of the system and future vacuum servicing.

We make one final note concerning the pumps. Ion pumps use large permanent magnets that generate substantial stray magnetic fields. We purposefully place the 30 L/sec pump as far from the Science cell as practical without limiting the pump speed. We observe little effect on the atoms in the Science MOT from this pump. Unfortunately, the 20 L/sec pump is placed very near the Collection MOT, since it's effective pump speed is limited by tube conductance. The stray fields are a nuisance for the Collection MOT, as they require larger shim coils that dissipate more heat.

### 5.1.5 System Layout

Several key ideas are incorporated into the layout:

•Minimize overall size to leave room on optical table for lasers, optics and cameras

•Place cells near table edges for easy access to optics and coils

•Set cell heights consistent with standard height of the lasers on the table. Keep the lasers mostly in one plane for eye safety.

•Preserve optical access by limiting obstruction by pumps and cells

•Design space for extensive light baffles and shields.

•Place system on a separate breadboard to construct and bake the system away from optics and lasers [154].

•Create thermal isolation between the vacuum system and the table for high temperature bake-outs.

The overall layout of the double MOT is very compact, as it requires a minimum of large and costly vacuum components (Figure 5.3). The system occupies only 86 cm $\times$ 60 cm on the table. The absence of large and heavy components means that the entire system is mounted simply on an optical breadboard using only aluminum supports under the heaviest and most sensitive joints. At the Collection cell end, the system is supported by holding the 20 L/sec pump. At the Science cell end, the four-way cross is supported under each arm by aluminum stands. The heavy 30 L/sec pump is supported in part by its connection to the cross, and also by a stand under its neck near the conflat joint. In each of the ion pump mounts we allow for removal of the permanent magnets (for baking the vacuum system and the pumps themselves). Finally, we support the conflat joint where the Science cell meets the

transfer tube to prevent accidental breakage of the fragile glass tube. Under all the mounts we place glass sheets or microscope slides to thermally isolate the aluminum mounts from the breadboard.

### 5.1.6 Construction, Pump-down and Bake-out

Before construction of the vacuum system all the pieces, except the ion pumps and cells, are degreased, cleaned in two ultrasonic baths, rinsed with methanol and finally rinsed with deionized water and left to air dry. The stainless components are then baked in air at 400 °C for 3 hours to purge water from the surfaces and form an oxide layer to bind surface sites where water may adhere. The system is constructed with UHV clean protocol. An important detail is we use non-magnetic and silvered screws in the conflat joints. The non-magnetic screws minimize stray magnetic fields near our atoms. The silvering allows us to use very little anti-seizing compound, greatly simplifying and sanitizing the construction. Once built, we pump down and bake-out the system using a grease and oil-free rough pumping station. The permanently attached 20 L/sec and 30 L/sec ion pumps are off during the entire bake-out.

The point of the initial bake-out is to clean out the system by heating of the residual water vapor and adsorbed gases from the system components into "dirty" vacuum pump that is later removed. In Table 5.1 we list some of the temperature limits of the components. We also outgas the dispensers (briefly) and TSP filaments during the bake since these contain large amounts of embedded impurity gases that could outgas during use and compromise operating pressures.

After the initial rough pumpdown we outgas the TSP filaments by slowly increasing current through each: 30 A for 10 min, 40 A for 15 min

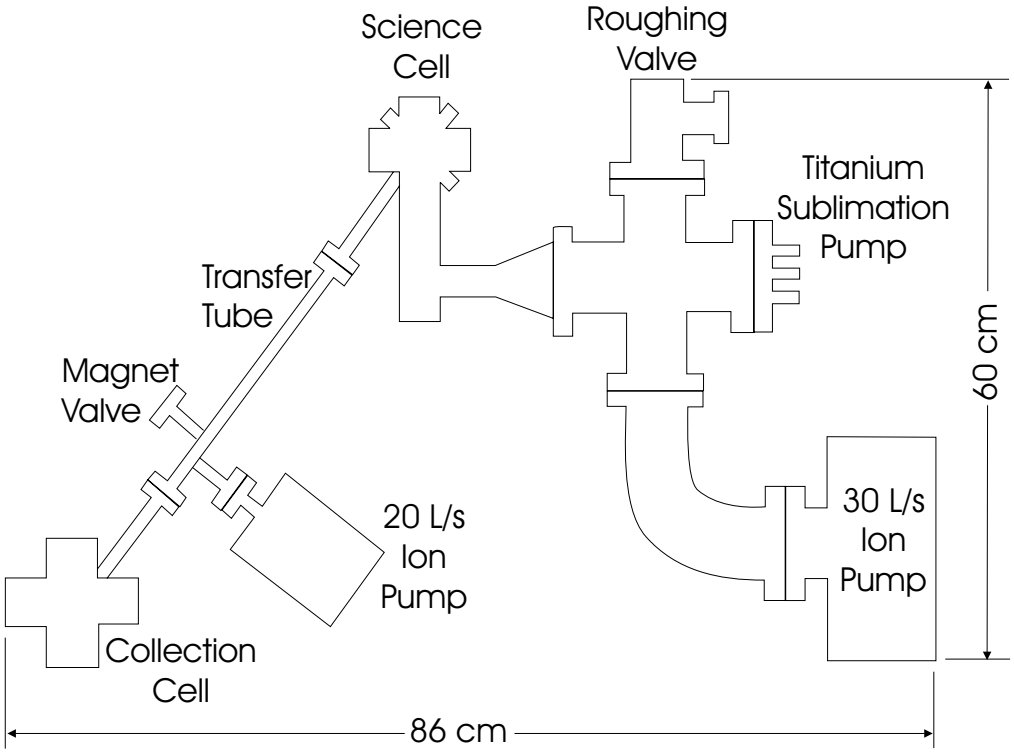


Figure 5.3: Layout of the JILA III Double MOT Apparatus

| component | temperature limit (°C) |
|---|---|
| glass-to-metal seals | 300 |
| Ti:Sub filaments and ceramic connectors | 350 |
| ion pumps: | |
| magnets | 250 (max) |
| | 300 (10-15% demagnetization) |
| High Voltage (HV) Connectors and metal body | 400-450 |
| bakeable HV cable | 250 |
| bakeable valve: | |
| open | 450 |
| closed | 300 |
| magnet "valve" | 250 |

Table 5.1: Temperature limits of vacuum components

($800 - 900$ °C) and finally a ramp up to 55 A over 1 min, followed by a quick rampdown of the current. The slow ramping prevents strain of the roughing pumps due to excess pressure from the outgas. Next, we outgas each alkali metal dispenser. We run them at 4.5 A for 5 min. During this process we notice the wire leads glow visibly, though the dispensers only heat to about 600 °C and outgas about 0.1 mg/cm (4%) of their total Rb.

Now we discuss the full system bake-out. We heat the system by wrapping heater tapes around the components to cover as much surface area as possible. We are careful not to overlap tapes because the heat generated can burn the tapes. At all temperature-sensitive joints and components (e.g. magnets, glass-metal seals) we place thermocouples to monitor bake temperatures. It is best to remove the ion pump magnets, but we left the magnets on for convenience and heated the pumps up to the maximum of 250°C. The entire system is wrapped in layers of fiberglass and aluminum foil to contain heat from the heater tapes. We specifically adjust the temperature at any given point on the system by locally adding or removing insulating layers.

We begin the bake by ramping up the heater tapes over $8 - 12$ hours to minimize the thermal shock to the vacuum components and moderate initial outgassing that could overwhelm the roughing pumps. We also run 20 A through one TSP filament to heat the vacuum system from within. The system is baked at near the maximum allowable temperatures for 48 hrs. We then cool the ion pumps over 6 hrs, after which we close the system from the roughing pump and then turn on the main ion pumps. The pumps operate on the system for 16 hrs while the rest of the vacuum system is still at high temperature. Finally, we cool the entire system down over 8 hours observing steadily decreasing pump currents (pressure). In all, the bake-out takes 90 hrs

to complete. Afterwards, the pumps register zero current, indicating pressures $\lesssim 10^{-10}$ Torr.

### 5.1.7 Rb Dispensers

The source of Rb atoms for our system are dispenser strips in which rubidium is chemically bound to the surface. The dispensers (purchased from Saes Getters) are 1.2 cm long and contain roughly 2.8 mg/cm each of Rb. The dispensers emit atoms when an electric current heats the metal strip and induces a chemical reaction that releases the Rb atoms. We placed six dispenser strips in the Collection MOT and use only one at any given time. Three dispensers each are connected in parallel, in one of two glass arms (Fig.5.2). Vacuum feedthroughs allow electrical connections to any single dispenser. Current is controlled by a 6 A, 30 V power supply. The equilibrium Rb vapor pressure is determined by the amount of current passing through the dispenser (and the equilibrium temperature the dispenser reaches). According to the specifications, maximum operating currents are $6-8$ A, for which the dispenser will yield 1/3 to 1/2 of its total Rb content in 20 min.

A period of curing of the glass surface is needed before any rubidium is observed in the glass Collection cell. Our detection scheme uses a double-passed beam from a diode laser whose frequency is swept through the $^{85}$Rb and $^{87}$Rb resonances (as determined by a separate vapor cell). Absorption of the beam by Rb vapor in the Collection cell is determined by the signal from a photodiode. We cured the cell with rubidium by operating each dispenser at $3-4$ A for about 5 min over the course of an hour. For one of these current tests we ran 5 A through a single dispenser for $5-10$ min. We noticed a blue-black film formed on the windows near the dispenser that we interpreted

was a layer of Rb metal. The film returned to the vapor when we heated the glass with a heat gun. Shortly afterwards we observed fluorescence of the probe beam with an IR viewer and absorption on the photodiode.

We have studied how the pressure in the MOT changes as a function the time the dispenser is turned-on or off, over a typical working day. The initial fill rate of the MOT is proportional to the pressure in the cell (Eq. (1.5)). By monitoring initial fill rate we can infer how pressure in the cell changes as a function of time (Fig. 5.4). At the beginning of the day the dispenser is turned-on with 2.5 A (Fig. 5.4a). The MOT fill rate rises by a factor of 75 and saturates at $1.5 \times 10^9$ atoms/sec after 4-5 minutes. The solid line is a guide to the eye. These data confirm that the dispenser rapidly increases the Collection cell pressure until a steady state is reached. After several minutes we turned off the dispenser current and observed the decay of the fill rate (Fig. 5.4b). The fill rate drops only a factor of 4.4, which is fit to an exponential decay curve (solid line) with a $1/e$ time of 0.37 min. We then turn-on the dispenser current and operate the experiment for 10 hours with the dispenser current running continuously. At the end of the day we turned off the dispenser current and again measured the initial fill rate as a function of time. The rate decays slightly, reaching a steady state of $5 \times 10^8$ atoms/sec in 7 min. The data are fit to an exponential (solid line) with a 2 sec $1/e$ time. The steady-state pressure of the cell, without the dispenser on, is nearly the same before and after long dispenser usage. The rate of decrease of the cell pressure may be slower after long periods of use, an effect that may be explained by gradual accumulation of rubidium in the cell. Once the dispensers are left off, the cell pressure is gradually reduced by the ion pump (on a time scale longer than 10 minutes, but less than 8 hours) such that in the morning cell pressure

is very low.

We have observed no deterioration in Rb vapor pressure, as inferred by MOT fill time, for the single dispenser we have used since construction of the apparatus. We therefore infer that the dispenser lifetime is at least 2 years when run approximately $10-12$ hrs/day at $2.2-2.6$ A. We note that this is the estimated lifetime in a glass cell environment. In our experience, Rb dispensers exhibit shortened lifetimes in steel-(rather than glass-)based vacuum chambers. The steel apparently consumes the Rb and the dispenser lifetime depends on the amount of steel surface area and the configuration of the dispensers relative to the surfaces.

## 5.2 Collection MOT

### 5.2.1 MOPA Trap Laser

We achieve rapid filling of large atom numbers in the Collection MOT through large beam size but also high total power. The large power exceeds the output of even the most powerful diode lasers, and typically implies the use of a Ti:Sapphire laser to reach the desired $0.5-1$ Watt. We instead introduced a substantial simplification for generating high-power infra-red light by using a solid-state Master Oscillator Power Amplifier (MOPA) system. The Master Oscillator (MO) is a low-power diode. Some of the light from the diode passes through a Power Amplifier (PA) chip, which is basically a semiconductor gain medium, that amplifies the power by nearly a factor of 100 and gives almost 0.5 Watts of total output power.

The layout for the system is shown in Figure 5.5. The master diode laser beam first passes through an optical isolator and a lens then focuses it

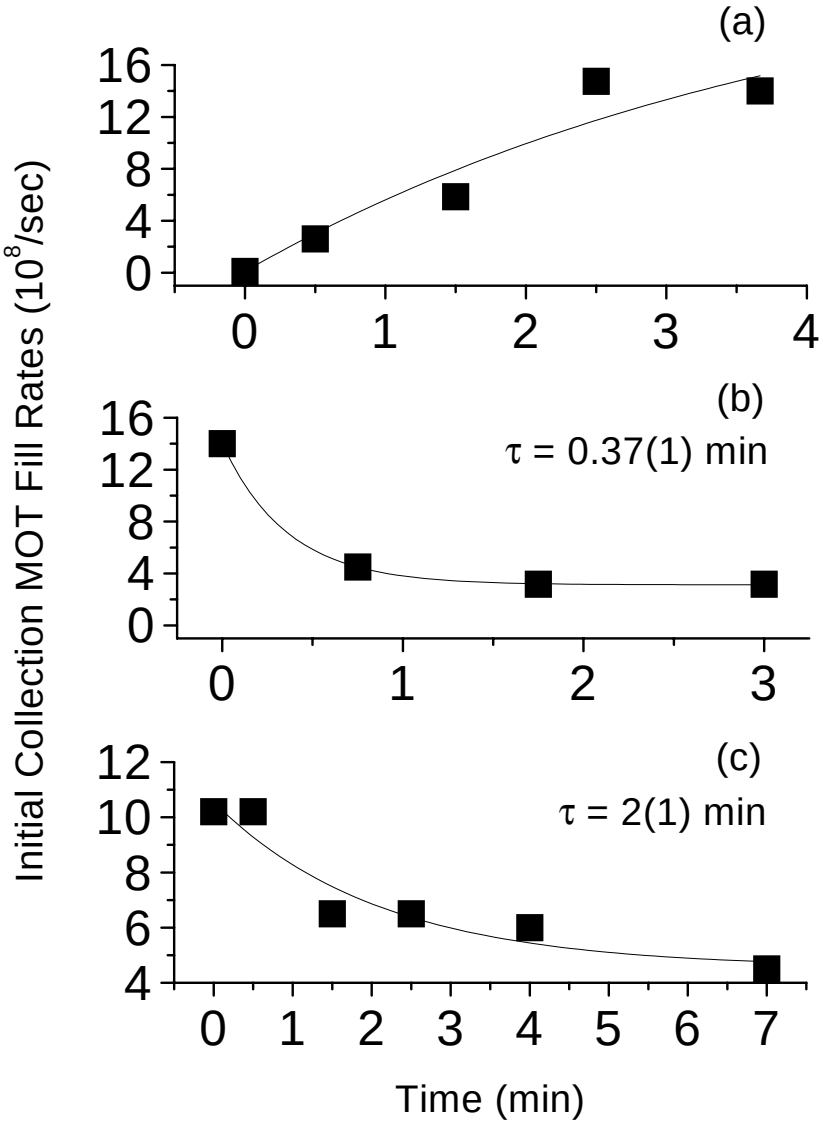


Figure 5.4: Change in the Collection MOT initial fill rate as a function of time the dispenser is on or off. (a) Rise in fill rate when dispenser is turned-on at 2.5 A at the beginning of the day. Five minutes after initially turning on the dispenser, the fill rate saturates. The solid line is a guide to the eye. (b) We then measure the decrease in the rate after the dispenser is turned off. (c) Decrease in the Collection MOT fill rate when the dispenser current is turned-off, after 10 hrs of continuous dispenser operation. The solid lines in (b) and (c) are exponential fits to the data with $1/e$ times given in the figures.

through an AOM (Acousto-Optic Modulator). The frequency shifted beam (8 mW) created by the AOM is deflected into the power amplifier chip. The undeflected and non-frequency shifted beam is further subdivided into a component used for saturated absorption spectrometry and one used as a probe beam for the Science MOT. An anamorphic prism pair is not used between the master diode and PA because the elliptical beam of the diode is suitable for coupling light into the rectangular face of the PA. The output of the PA is at high power and has a highly elliptical ($4-5:1$) beam profile. We use cylindrical lenses to remove the ellipticity. Alignment of master diode and power amplifier is made robust by mounting the entire MOPA system onto a single breadboard. The breadboard is vibrationally isolated from the optical table by thin strips of rubber. However, good alignment of diode light into the amplifier makes the diode susceptible to optical feedback (from back reflections off the PA front facet and amplified spontaneous emission from the PA). Feedback is minimized with a 35 dB optical isolator.

The master laser is an external-cavity stabilized diode laser (ECDL) with a net output power of 19 mW. The design of the laser is discussed elsewhere [155]. As mentioned above, the beam from the master diode that is undeflected by the AOM (11 mW) is used for laser stabilization and probing. After the AOM, the beam passes through anamorphic prism pair to eliminate ellipticity in the beam profile. A small amount of power is split off by a plate beamsplitter and is sent to a standard saturation absorption spectrometer [155]. The rest of the beam power is devoted to a beam for probing the atoms and is discussed in detail below. The laser is frequency modulated, at a frequency of 300 kHz and small depth of modulation, using a dither of the diode current to create a derivative error signal about peak features in the

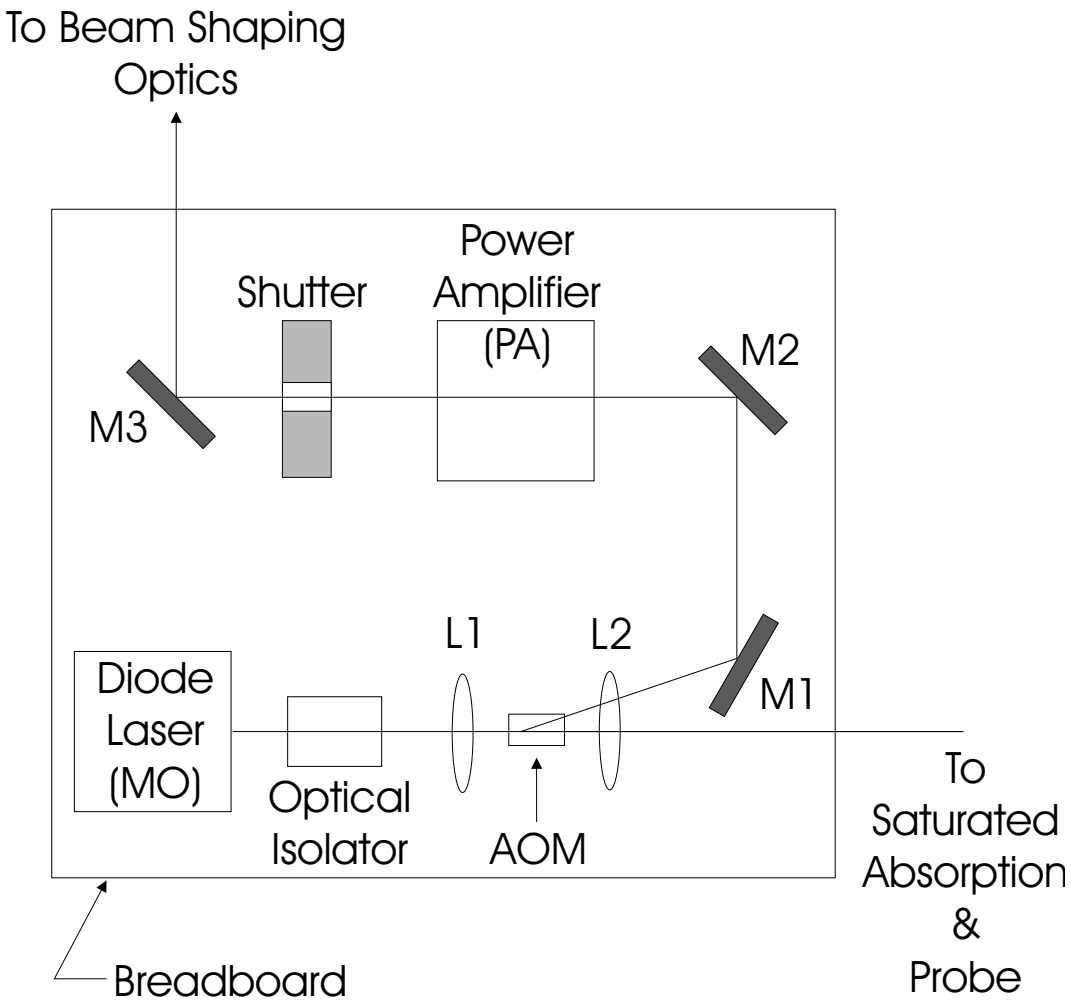


Figure 5.5: Layout of the MOPA laser system used for trap light in the Collection MOT and probe light cold atoms in the Science MOT. M = mirror; L = lens

saturated absorption spectrum. We stabilize the laser frequency by using the slope of the dispersion curve to servo the MO laser PZT and diode current about the desired absorption peak. Since we use the MOPA for MOT trapping and near-resonant probing we peak-lock to the cross-over transition between the $5S_{1/2}F = 2 \rightarrow 5P_{3/2}F' = 2$ and $5S_{1/2}F = 2 \rightarrow 5P_{3/2}F' = 3$ transitions that lies 133.5 MHz to the red of the "cycling" $F = 2 \rightarrow F' = 3$ transition. The MOT detuning is set by choosing the frequency shift of the deflected beam ($\sim$ 120 MHz).

### 5.2.2 Repump Light

Our system requires much less power on the $5S_{1/2}F = 1 \rightarrow 5P_{3/2}F' = 2$ repumping transition. We generate enough repump light for both Collection and Science MOTs from a single ECDL with total output of 17 mW. We divide the beams with a $\lambda/2$ plate and polarizing beam splitter cube and send 2 mW to the Collection MOT. As described above, the frequency of the repump laser is also stabilized to the $F = 1 \rightarrow F' = 2$ saturated absorption peak using a 300 kHz current dither. We found that both MOTs operate well at zero detuning so that a direct peak-lock is sufficient. After the saturated absorption spectrometer, an optical isolator prevents feedback to the diode. Lastly, the diode laser and spectrometer is enclosed in a black-cardboard housing to contain scattered photons. We have found this eliminates optical depumping of $F = 1, m_F = -1$ state during evaporative cooling.

### 5.2.3 MOT Configuration

To take full advantage of the 38 mm window diameter we use 50 mm optics throughout the MOT set-up. We combine the MOPA and repump

light, and then use two telescopes and one polarizing beam splitter plate to produce three beams that are roughly rectangular-shaped with approximate $1/e$ dimensions of $25 \times 20$ mm. The irregular shape and profile is the result of (non-optimal) beam shaping optics and AOMs. The imperfections in the beam do not prevent us from rapidly accumulating large numbers of atoms in the MOT. We use 50 mm mirrors and $\lambda/4$ plates, which minimize beam clipping and power loss, to direct the beams into the cell in a standard 3-beam retro-reflected MOT configuration. The quadrupole field for the MOT is generated by a pair of air-cooled coils wound from magnet wire and placed in anti-Helmholtz configuration. Stray magnetic fields, especially from the nearby ion pump, are compensated by three, unpaired shim coils. We monitor the MOT number with a PD and position of the MOT with a low-cost CCD camera.

### 5.2.4 Alignment and Operation

Alignment of the Collection MOT is non-critical because the trap beams are so large and low temperature in the MOT is not important for transfer. The basic goal is to occupy as much of the clear aperture of the windows as possible with MOT light. We balance the beam intensities and then roughly retro-reflect the beams to achieve reasonable MOT fill-rate and total number. We optimize the rate and number by adjusting the retro-mirrors while monitoring the PD signal. This procedure also places the atoms nearly along the transfer tube axis. We then optimize the transfer by slight adjustments to the currents in the shim coils; these adjustments do not degrade either MOT fill rate or total number. Typically we run the MOT at 10 G/cm, using a total of $\sim 300$ mW in the trapping beams once they reach the Collection cell, running

the dispenser current at $2.3 - 2.8$ A for a background pressure of roughly $10^{-9}$ Torr. We achieve a maximum total fill of $1.5 \times 10^9$ atoms in the MOT with a $1/e$ fill time of $1 - 2$ sec.

## 5.3 Science MOT

### 5.3.1 General Considerations

The purpose of the Science MOT is to provide an environment for loading a purely magnetic trap, at the lowest temperatures and highest densities possible, in a low-background pressure. The sufficient conditions are: (i) hold $> 10^9$ atoms; (ii) optically cool atoms to sub-Doppler temperatures in a molasses; (iii) optically compress the atoms in a Compressed MOT (CMOT); (iv) allow alignment of optical trap and magnetic trap for smooth transfer of atoms; and (v) optical access to probe small atom clouds (10's of $\mu$m).

### 5.3.2 Lasers

The trapping light for the Science MOT is generated by a single ECDL that is offset peak-locked to the cross-over transition between the $F = 2 \rightarrow F' = 2$ and $F = 2 \rightarrow F' = 3$ transitions. The scheme is completely identical to the lock used for the MOPA laser except that the deflected beam is sent to the spectrometer and the undeflected beam is sent to the MOT. The reason is that we did not want to affect the MOT alignment by changes to the AOM frequency, which in turn also shift the beam position. The net beam power out of the laser is 55 mW while the power after the optical isolators and AOM's, but before division of the beam into the separate MOT beams, is 20 mW.

Repump light on the $F = 1 \rightarrow F' = 2$ transition is provided by

our single repump laser. The total power sent to the Science MOT is 2 mW. Initially this laser was locked to the side of the saturated absorption feature and proved more than adequate to make reproducible Bose condensates in the $F = 2, m_F = 2$ state. We switched to a peak-locked repump only after we began to produce condensates in the $F = 1, m_F = 1$ state, when we require frequency-stable repump light for optically pumping the atoms during the probe pulse. We also modify the delivery of the repump light to the Science MOT for the CMOT stage. We divide the repump beam into a main beam of 6 mW and a bypass beam of only 35 $\mu$W. The set-up for the repump bypass is shown in Figure 5.6.

### 5.3.3 Quadrupole Coils

The quadrupole field for the Science MOT serves two ends. In the MOT loading phase, it generates the modest field gradient (axially, $B'_z = 17$ G/cm) for the MOT. In the magnetic trap phase, the coils must safely generate significantly higher gradients, handling kW's of power and still possess a rapid turn-off time. The quadrupole coils are constructed with $\frac{1}{8}$" hollow copper tubing that is wound into two coils. Each coil is 3 turns tall by 4 turns deep and forms an annulus with rectangular cross section of 1.5 cm tall by 1.75 cm deep (Figure 5.7). The inner diameter of the coil is 1.27 cm and the inner surface separation of the coils is 3.5 cm. The windings are electrically insulated from each other by sheathing the copper in heat-shrink tubing. The coils are made structurally solid by potting them in epoxy. We water cool the coils with a wall-pressure flow of room temperature water through the hollow copper tubing.

The coils are connected in series, in a nearly anti-Helmholtz config-

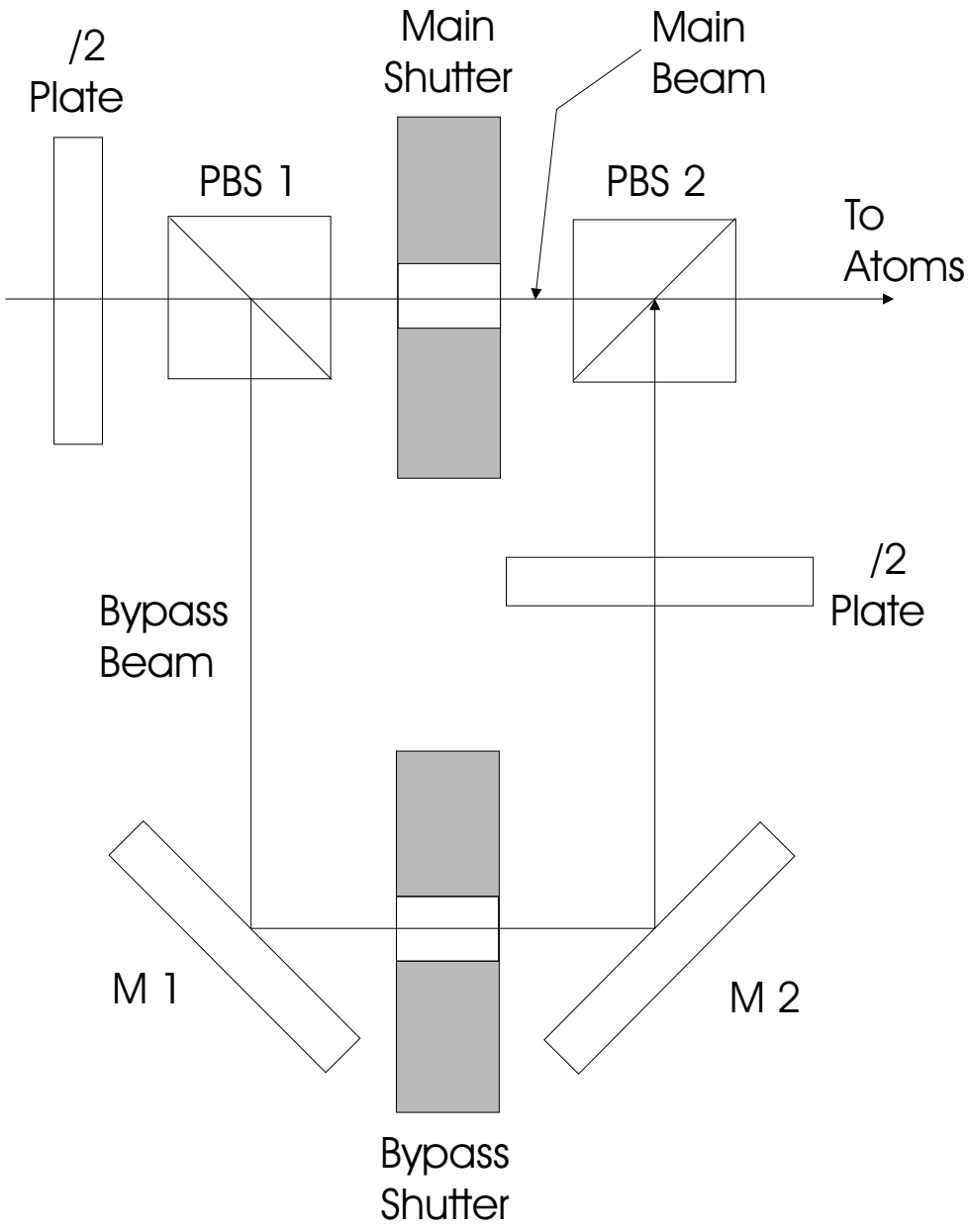


Figure 5.6: Bypass scheme for the repump light to the Science MOT. PBS = Polarizing Beam Splitter Cube; M=mirror

uration. Since maximizing gradient is our primary goal, the coils are placed as close to the atoms as possible, with a distance generally limited by optical access. Each coil has a resistance of about 6.8 m$\Omega$. We supply the coils with a 6 V, 300 A power supply. The supply voltage and lead resistances limit the ultimate field gradients to be $B'_z = 305$ G/cm at around 260 A. At 6 V and 13.6 m$\Omega$ the max current is 441 A and max power dissipation is 2700 Watts. However, finite resistance in wires and connectors limits the maximum voltage drop across the coils to 3.5 V and power dissipation to 1600 W. From the coil geometry we calculate the inductance $L$ of the coils [156] is equal to 4.9 $\mu$H. Treating a single coil as an inductor in series with a resistance of $R = 6.8$ m$\Omega$ gives the $1/e$ decay time of the current: $\tau = L/R = 720$ $\mu$sec. We measure 900 $\mu$sec. The currents (and hence fields) are stabilized using a bank of water-cooled power FET's as described in [157].

### 5.3.4 Shim Fields

Stray magnetic fields inevitably shift the zero point of the magnetic field from the center of the MOT beams, and alter the delicate overlap between MOT and magnetic trap. We minimize stray fields by assiduously avoiding magnetic bases and magnetic metals (screws, mounts, vacuum components) near the glass cell. Stray fields are shimmed by three, unpaired coils. The divergence of the shim field is so slight as to be insignificant to operation of the MOT, molasses or magnetic trap. We also switch the currents through the shim coils to different values. One set of currents is optimized for loading the MOT to maximum fill from the Collection cell. The other set of currents optimizes the molasses cooling and TOP loading, usually by observing the isotropy of the molasses expansion, but sometimes also by optimizing number

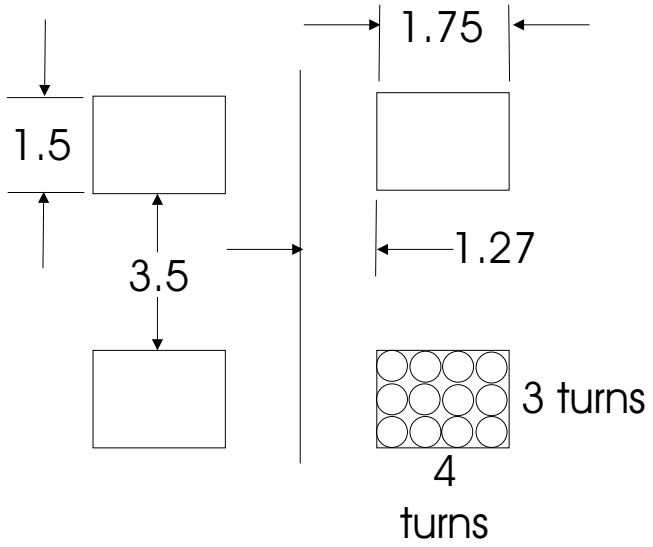


Figure 5.7: Cross-section of the Quadrupole Coils. There are two coils, with symmetry axis parallel to gravity (and the long edge of the page). Dimensions are in cm.

in the condensate.

### 5.3.5 MOT Configuration and Alignment

The Science MOT uses a configuration of six independent beams. Although the 6-beam approach is more cumbersome to align, previous experience suggested that 3-beam Rb MOTs did not fill to as large a number or perform as robustly [152]. One factor is optical attenuation: With $10^9$ atoms in a MOT cloud of 0.5 cm diameter and trap light detuning of 3 linewidths the absorption of a single pass through the cloud is 30%! Losses from scattering off uncoated optical surfaces (4%) can also shift the equilibrium position of the MOT away from the zero-point in quadrupole magnetic field, due to imbalances in beam intensity. Therefore MOT stability is reduced, as is the efficiency of molasses cooling.

Because alignment is more challenging, we emphasize ease of coupling light into the cell, from all directions, with the least amount of loss. We use two-inch optics wherever possible and especially far from the cell, where small beam clipping means significant loss of power. The larger optics also simplify alignment because the MOT beams are much smaller in diameter than the optics. Other notes on optics and design:

• Near the cell, large optics limit optical access so we more carefully align 25 mm dia PBS cubes and $\lambda/4$ plates immediately before the cell.

• Use of Dielectric mirrors throughout the optical layout minimize loss of power and preserve wavefront integrity. Nonetheless, the AOM's and optical isolator degrade the wavefront quality substantially.

• Mounts are very minimal short posts and post-holders. Larger mounts limit access to the cell without improving MOT stability.

We align the MOT with the following procedure. We balance the power for each direction and optimize the throughput. We designate three especially difficult-to-align directions as the "Cardinal" directions, and align those three beams to be centered and normally-incident on the cell windows. Aperturing the beam sometimes helps, but it is most important that the majority of the irregular beam profile is centered on the window. This ensures that most of the power reaches the atoms. Next, we align the three "anti-Cardinal" beams to overlap with the "Cardinal beams". The overall procedure usually produces a MOT of many $10^8$ atoms with an irregular cloud shape. The problem may be in the irregular profiles of the MOT beams. In any event, we optimize total number of atoms in the MOT by monitoring a PD signal and adjusting the anti-Cardinal beam alignment only . This tends to produce MOT clouds that are more round-shaped, and which contain large, stable numbers of atoms ($3-9\times10^9$ max). The molasses also performs best in this alignment.

### 5.3.6 MOT Operating Characteristics

Even with only $10^6$ atoms, most MOTs operate in the constant density regime. Thus, adding more atoms necessarily means increasing the cloud diameter. The ultimate limit to the total number of atoms contained in a MOT is therefore the size of the MOT beams and the shape of the intensity profile. Specifically, integrity of the beam profile and details of the beam quality at the edge of the beams, which comprise large trap volumes, can strongly affect number in the MOT. With $10^9$ atoms in our MOT, operating at a detuning of 18 MHz, the cloud diameter is $5-7$ mm (defined as the full-width at half-maximum (FWHM)) and the mean density is approximately $10^{10}-10^{11}$ atoms/cm$^3$. Each beam has a total power that is typically 2 mW, with a

FWHM equal to roughly 1.5 cm (although the profiles are fairly non-Gaussian) giving an average intensity of 0.9 mW/cm$^2$

We make several observations about our MOT, from which we connect large sensitivity of max MOT fill and low optical cooling temperatures to beam alignment and spatial profile. We note that:

•Significant re-alignment of the beams, even after the MOT beams **seem** aligned and retroreflected, is necessary to reach the maximum MOT fill. This suggests that details of the beam profile, in addition to beam alignment, are important.

•Small beam power imbalance can seriously degrade the total fill, the molasses temperatures, or both.

•An intermediate alignment of the beams can produce MOT clouds of $1-2\times10^9$ atoms that are highly unstable. The clouds have large, wispy arms and lose many atoms at irregular intervals. Using this fairly large, unstable MOT we can still produce BEC's, but with generally fewer atoms and less repeatability than in our best MOT alignment.

•The best MOT numbers and temperatures are obtained when the cloud appears very regular and round. Number of atoms in the condensate is largest, and most reproducible, under these conditions.

Lastly, I mention the issue of MOT lifetimes. The MOT lifetime is a useful diagnostic for inferring the background pressure of the Science cell. The time rate-of-change of the number of atoms in the MOT is well-understood in terms of a loss rate due to background gas collisions, which is proportional to number $N$, and a loss rate due to light-assisted collisions between atoms in the MOT, which is proportional to density squared (see Eq. (1.6)). In the low background pressures of the Science MOT, the MOT collection rate

is negligible and we observe no formation of a MOT directly from the vapor. Hence, knowledge of the background pressure is determined from the loss of atoms from the MOT. However, a simple analysis shows that light-assisted collisions complicate the interpretation of the MOT lifetime in terms of the background vapor pressure. For a Rb MOT whose trap beams are red-detuned several linewidths from resonance, and which has total beam intensity equal to several times the saturation intensity, the light-assisted decay rate constant is $\beta \approx 10^{-12}$ cm$^3$/sec [158]. A MOT with rather modest density of $10^{10}$ atoms/cm$^3$ will therefore have a light-limited lifetime of 100 s. With approximately $10^8$ atoms in a MOT whose trap beams are red-detuned 20 MHz, and which have a total intensity of 10 mW/cm$^2$, we measure lifetimes of about 150 sec. We expect that our background collision rate is much smaller than that. We suppressed light-assisted losses by reducing the number of atoms, which decreases the MOT density. Using only $2 \times 10^6$ atoms, we measure MOT lifetimes of $450 - 500$ sec. Reducing the total MOT intensity also increases the observed MOT lifetime. The longest observed lifetimes are consistent with a background pressure below $10^{-11}$ Torr.

## 5.4 Collection MOT to Science MOT Transfer

### 5.4.1 General Scheme

Atoms are transferred from the Collection cell to the Science cell by applying a near-resonant laser beam that pushes atoms down the transfer tube separating the Science cell from the Collection cell. The transfer efficiency is bolstered by using a hexapole magnetic field along the transfer tube that provides radial magnetic confinement. Several strategies work in the transfer.

Typically we accumulate atoms in the Collection MOT, turn off the MOT, apply a short pulse of the push laser, and then recapture the atoms in the continuously operating Science MOT. We repeat the process until the Science MOT reaches the desired number of atoms. We have also successfully transferred atoms using a continuous push beam and a Collection MOT cloud (the cloud is slightly offset from the axis of the transfer tube and push beam). This creates a sort of Low-Velocity Intense Source [159] loading, whereby atoms are continuously pushed out of the MOT and travel down the tube. Although we have not compared the two approaches in detail, we have observed the pulsed mode tends to have better transfer efficiency and requires less time to fill the Science MOT. In the following sections I describe our standard procedure for transferring in the pulsed mode.

### 5.4.2 Hexapole Magnets

The transfer efficiency is boosted considerably by a hexapole magnetic field along the transfer tube. The magnetic potential is harmonic in the radial direction of the tube and prevents atoms, with slight radial velocities, from colliding with the walls and hence being lost during transfer. The hexapole field is created by six strips of permanent magnets which form a hexagonal arrangement around the tube. To provide maximum confinement, the magnets rest directly on the tube and are conveniently held together around the tube by their self-attraction. Small breaks in the magnet strips, due to conflat joints or transverse tubes for the ion pumps/magent valve, do not cause enough tranverse displacement on the atoms during their flight down the tube to degrade efficiency.

### 5.4.3 Push Beam

The push beam is 6.5 mW derived from the main MOPA beam used for the Collection MOT. The beam is directed down the transfer tube, through the access window of the Collection cell, and is brought to a shallow focus near the Science MOT. Just before the transfer window, the beam is circularly polarized with a $\lambda/4$ plate. No magnetic field is used to create a quantization axis during the optical push. The push pulse duration is controlled with a mechanical shutter whose minimum cycle time to turn on and off is about $1-2$ ms.

### 5.4.4 First-Time Alignment

The best approach to observe transfer is to build both MOTs, assigning the polarizations and quadrupole field directions of the Science MOT based on a working Collection MOT. The transfer signal is then an unambiguous cloud that is observed with a CCD camera. Even small numbers of transferred atoms are well-detected by simply repeating the push cycle and watching the Science MOT cloud accumulate. Without building the Science MOT, we monitored the atoms that reach the Science cell, causing them to fluoresce with a probe beam transverse to their velocities, and detecting the fluorescence with a PD. This method gives information about the velocity distribution and group velocity of the atoms, but tends to undercount the total number transferred. Generally, use as many atoms and as much push power as possible during first alignment. The beam direction and Collection MOT position are easily chosen by sending the push beam through both transfer windows and adjusting the shim coils of the Collection MOT until you see the

cloud, in the Collection MOT, become distorted by the push light. The initial detunings and intensity are set by maximizing the distortion of the MOT cloud.

### 5.4.5 Transfer Procedure

We transfer atoms by applying the push beam to the Collection MOT and turning off the MOT trap light. The atoms are accelerated up to 20 m/sec (and out of resonance with the push beam) in under 1 msec and reach the Science MOT in approximately 20 msec. The push light remains on during the entire flight of the atoms, after which (at 30 msec) the push turns off, and the trap light and field gradient of the Collection MOT turn-on again. The hyperfine repump light remains on during the entire cycle, initially so that atoms scatter sufficient photons to be pushed down the tube, and later out of convenience. The Collection MOT then rebuilds for 750 msec in preparation for another transfer. The details of the timing are given in Figure 5.8.

We monitor the progress of the fill of the Science MOT by triggering a storage scope to record the MOT fluorescence every fourth transfer. The fluorescence, collected on a PD, is proportional to the number of atoms in the Science MOT. Our computer checks the fluorescence to determine when the MOT has filled to the desired number of atoms, and hence when to terminate loading. When the number in the Science MOT is within about $2\times10^8$ atoms of the total fill, the computer switches to a an abbreviated rebuild time, between transfers, of only 250 ms. The timing of events is suitably compressed to detect fluorescence at the time given in the bottom panel of Figure 5.8. The shorter build time allows a gradual approach to the desired fill and reduces the variation in the final number loaded into the Science MOT.

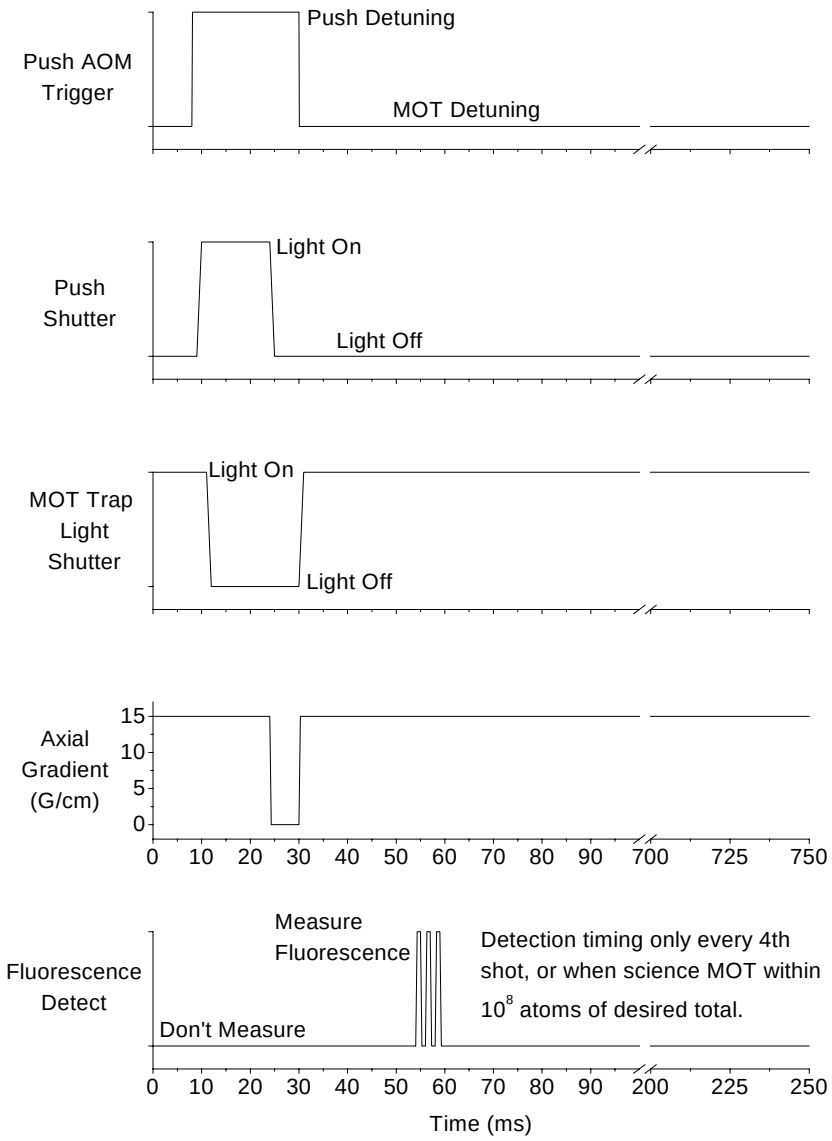


Figure 5.8: Timing of the Collection MOT to Science MOT Transfer. (a) Pulse AOM briefly shifts MOPA frequency to push detuning. (b) Status of push shutter. (c) Collection MOT trap light shutter. (d) Collection MOT axial quadrupole magnetic field gradient. (e) Trigger to record fluorescence signal on photodiode for monitoring progress of Science MOT fill.

### 5.4.6 Final Notes on Transfer

We estimate the transfer efficiency is about 25%. We tend to undercount the Collection MOT number because the Collection MOT is larger than the field-of-view of our imaging PD. Optimal transfer of atoms generally is achieved by adjusting the power, detuning polarization and alignment of the push beam, as well as the position of the Collection MOT. The beam occupies most of the input window to the Collection cell. When the beam is passed too close to the Science MOT it is clearly visible because each transfer produces a transient displacement of the Science MOT cloud, which limits the transfer efficiency for large MOT clouds.

The magnetic valve is left open during the entire transfer cycle, and throughout the day while the experiment is active. When the experiment is not in use, we slide the magnet plug across the transfer tube to minimize the integrated flux of Rb down the tube. In principle, we can open/close the valve each shot, or every experimental cycle, but we have never observed a degradation of the Science MOT pressure leaving the tube open even for 24 hours.

## 5.5 TOP Magnetic Trap

The TOP trap is made of six coils. The spherical quadrupole magnetic field is generated by the quadrupole coil (Section 5.3.3) whose symmetry axis is parallel to the direction of gravity. The rotating bias field is created by two pairs of coils, each of which creates a uniform magnetic field in the center of the cell, driven 90° out-of-phase. Each coil is actually shaped as an ellipse in order to wrap them directly to the glass cell (as explained below). The coil diameters

are 3 cm (horizontal) and 1.5 cm (vertical), and the coils are placed 1.7 cm from the center of the trap. The field shimming coils, described in Section 5.3.4, cancel stray magnetic fields and align the MOT with the magnetic trap. The theory of the TOP trap is given in Chapter 6 and Appen. C.

The TOP coils are also water cooled using a substantially different design than the quadrupole coils. We require less cooling capacity but more winding flexibility for the TOP coils compared to the quadrupole coils. Some cooling is necessary because we dissipate up to 180 Watts through the coils. As a second requirement we also wanted to wrap the coils very close to the cell to maximize the TOP bias field per amp-turn, requiring much more freedom and flexibility in the coil winding than allowed by hollow copper tubing. The recipe for the TOP coils is as follows. We insert three sections of 22 AWG magnet wire into a polyflo tube of $\frac{1}{8}$" outer diameter. The wire sections are electrically connected in series. The polyflo is wound directly onto the experimental glass cell to form a pair of approximately Helmholtz separated coils with three (nine) polyflo (magnet wire) windings in each coil. A second polyflo/magnet wire tube is prepared and similarly wrapped, though 90° offset from the first coil pair, around the glass cell. Room temperature water is pushed through the polyflo at wall pressure to cool the wires. The net flow is extremely small, but is sufficient to handle the maximum power when generating rotating bias fields of up to 50 G.

The TOP coils are driven from a high-fidelity sine wave that is amplified through a voltage-controlled gain. The sine wave is divided into two channels which have separately adjustable gain and adjustable relative phase. The channels are separately amplified by a two-channel audio amplifier. The maximum output power of the audio amp is 180 W and must be impedance

matched to the TOP coils. We use a pair of home-built transformers wound around magnetic ferrite cores to both impedance match and step down (up) the voltage (current). Small differences in coil size and relative phase-shifts require a careful calibration of the actual TOP field. We detect the rotating field with two identical 25 turn, 2.5 cm dia pick-up coils whose axes coincide with the TOP coil pairs. The detection coils are placed at the same distance from the atoms as the TOP coils. The induced EMF is integrated and output to a scope to create a Lissajou figure whose amplitude and phase are proportional to the rotating magnetic bias field. Monitoring the Lissajou, and using our gain and phase adjustments, we can create a nearly circular (within 5%) or a highly elliptical rotating field. The rotating field is a natural quantization axis for the experiment. We utilize the field by synchronizing critical probing and optical pumping timing to the TOP rotation and computer triggers. The synchronization is achieved with a home-built triggerable pulse-generator or a commercially-produced pulse sequencer.

## 5.6 MOT-to-TOP Transfer

### 5.6.1 General Considerations

The protocol for transferring atoms from the Science MOT to the TOP magnetic trap consists of:

$$\text{MOT} \rightarrow \text{CMOT} \rightarrow \text{optical molasses} \rightarrow \text{optical pumping} \rightarrow \text{TOP}$$

The MOT collects and holds the atoms until the desired initial number is reached. The CMOT compresses the atoms into a smaller, more uniform cloud and initiates the ramp-down of magnetic field for molasses. The optical

molasses precools the atoms to sub-Doppler temperatures. Pulses of optical pumping light transfer most of the atoms into the desired state for magnetic trapping. Finally, the TOP is turned on by quickly turning-on the rotating bias and increasing the quadrupole gradient.

### 5.6.2 Prelude to Transfer

After the final load of atoms arrives from the Collection MOT, but before initiating the following procedure to load the TOP trap from the MOT, we wait 250 msec. The lifetime of the MOT is longer than 100 sec so little of the gas sample is lost during the short wait. The wait permits the MOT to thoroughly settle after the last injection of atoms. The wait time is also useful for technical housekeeping such as setting program flags and initiating equipment for later use.

### 5.6.3 CMOT

The CMOT is one of the least well-characterized stages of the experiment. The previous comprehensive study of the CMOT [19] operated with only $\sim 10^7$ atoms, using different detunings, trap light intensities and field gradients. The CMOT we use is optimized to transfer the most atoms, at low temperature, into the TOP trap and little careful study has been done. The CMOT stage lasts 30 ms. First, the detuning of the trap laser is shifted to 32 MHz red of the cycling transition (Fig. 5.9a). Immediately (1 ms) later, we dramatically reduce the repump light intensity by allowing only the repump bypass to illuminate the atoms (Fig. 5.11a). Next, we ramp down the axial quadrupole gradient from 17.4 to 5.2 G/cm in ten, 1 msec steps. We leave the atoms in this reduced gradient for 10 ms, and finally ramp the gradient off in

ten, 1 ms steps. See Fig. 5.10a. The trap laser is then red-detuned 45 MHz from resonance to begin the molasses stage (Fig. 5.9a). During the second 10 ms period, we change the currents in the Science MOT shim coils from their values optimized for MOT loading to values optimized for the TOP loading (Fig. 5.10c). Recently, we have also found that **not** increasing the trap laser detuning during the CMOT enhances the final number in the condensate, despite little change in the observed efficiency of transferring atoms into the TOP. We speculate that the beneficial effects of (i) reduced repump light intensity, (ii) reduced field gradient, and (iii) reduced detuning may be understood qualitatively in terms of increasing the region of the trap over which the Stark shift is large compared to the Zeeman shift of the atoms. In this region, the cloud that experiences strong polarization gradient (sub-Doppler) optical forces, as opposed to the weaker, spontaneous scattering (Doppler) optical forces which affect the rest of the cloud. All three effects in the CMOT therefore improve the initial conditions for evaporation by cooling and/or compressing the cloud.

### 5.6.4 Molasses Cooling

The molasses lasts 10 msec. During the molasses, the quadrupole field gradient remains off (Fig. 5.10a) and the only repump light is supplied by the bypass beam (Fig. 5.11, a and b). Because of technical problems we are unable to re-lock the laser at the molasses detuning (Fig. 5.9c), but over the brief duration of the stage we observe very little drift in frequency.

### 5.6.5 Optical Pumping

Next, we perform optical pumping on the atomic sample to transfer most of the atoms into the $F = 2, m_F = 2$ or $F = 1, m_F = -1$ or both states.

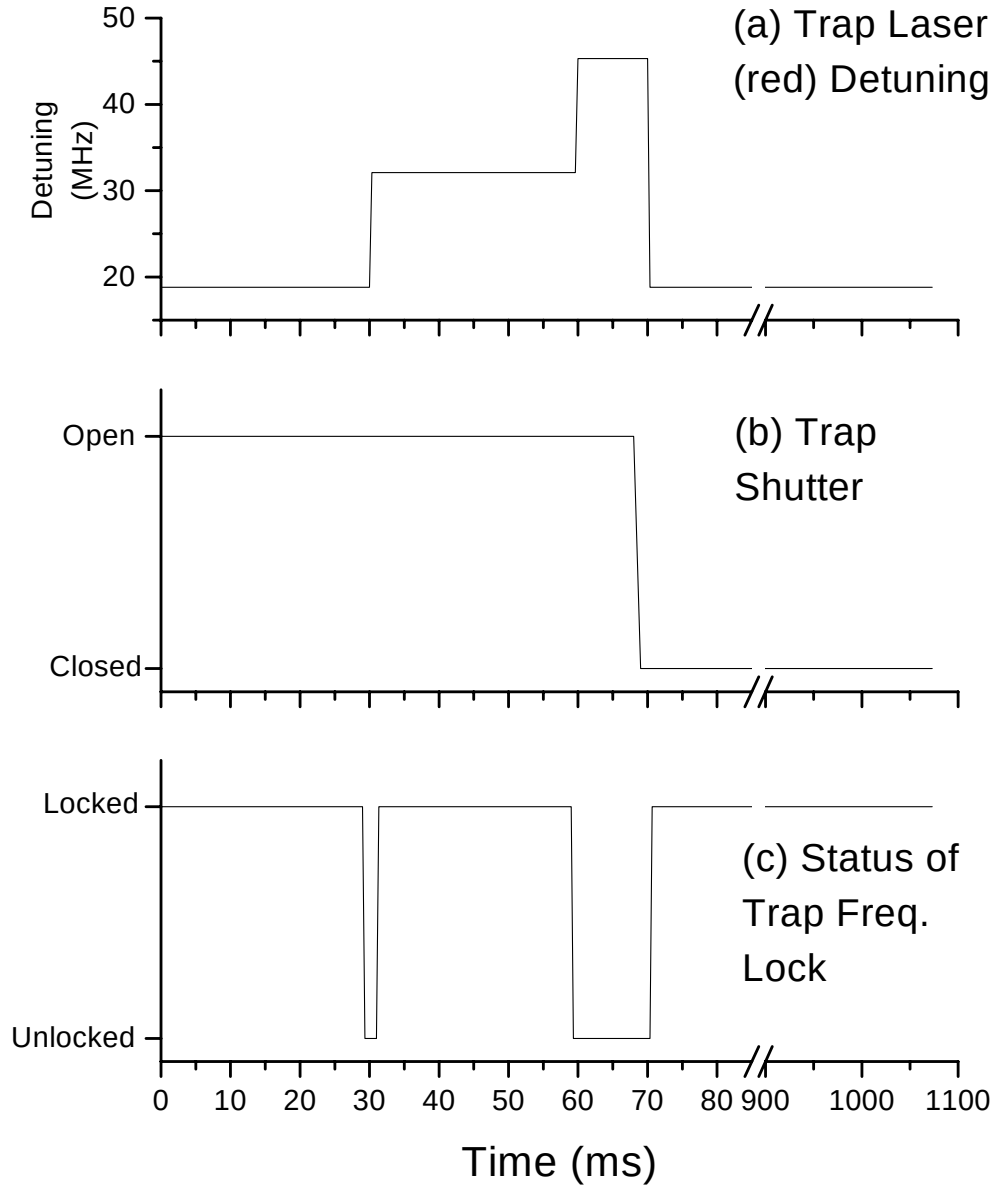


Figure 5.9: Timing of the Trap Laser Parameters during MOT to TOP Transfer

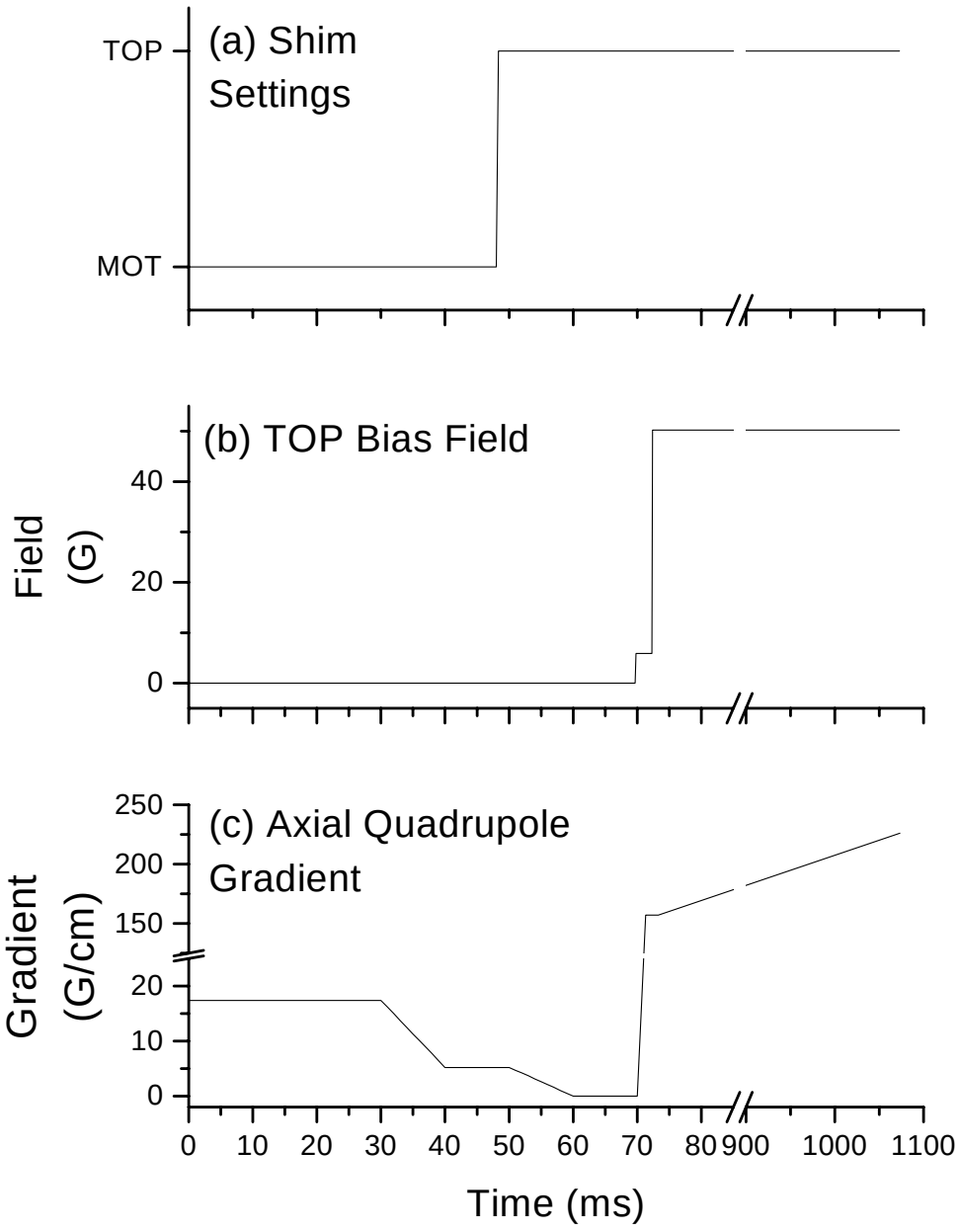


Figure 5.10: Timing of the magnetic fields during MOT to TOP Transfer. (a) Values for the shim coils, optimized either for Science MOT loading or TOP magnetic trapping. (b) Amplitude of the TOP rotating bias field. (c) Axial Quadrupole gradient.

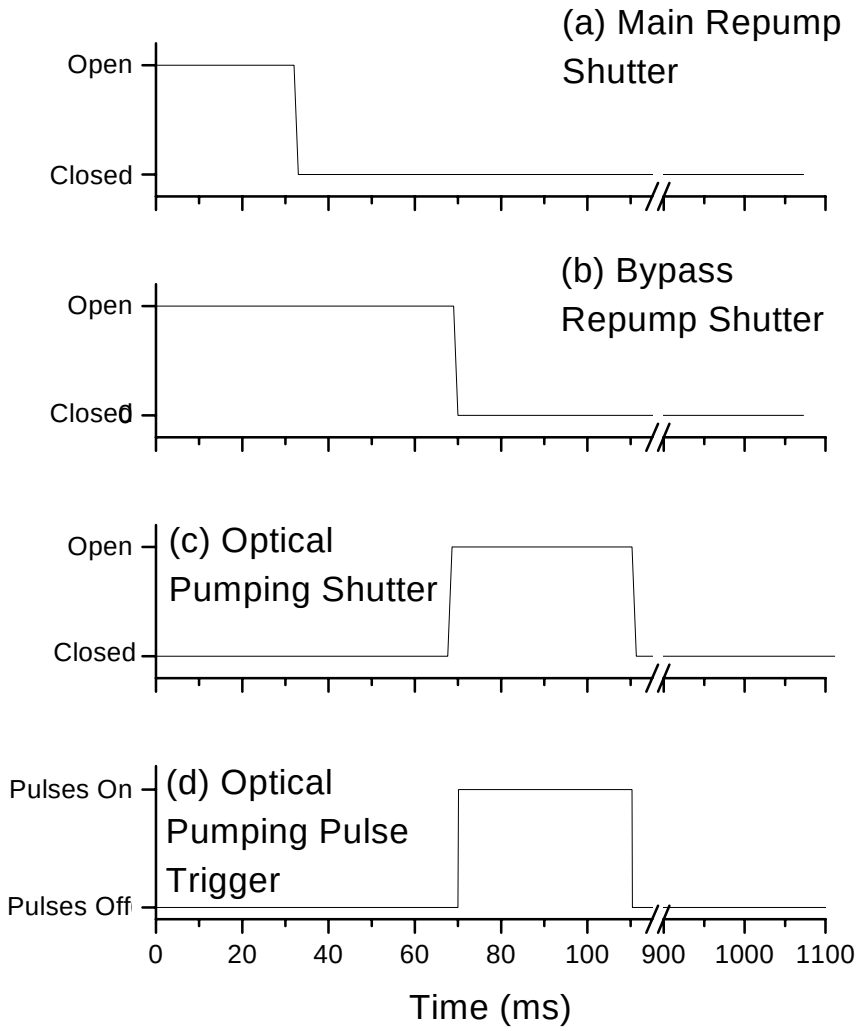


Figure 5.11: Timing of the Repump and Optical Pumping during MOT to TOP Transfer. Frame (a) shows the status of the shutter for the main repumping light; when the shutter is open, light illuminates the atoms. Frame (b) is the shutter for the bypass repumping light. Again, when the shutter is open, bypass repump light illuminates the atoms. (c) Status of Optical Pumping Shutter. (d) Optical Pumping Pulse Trigger. Optical pumping light illuminates atoms in multiple pulses, but only for the time when the trigger pulse is high.

Because we use the TOP rotating bias field as a quantization axis (5.9 G, see Fig. 5.10b), synchronization of optical pulses with the field is critical. We initiate a pulse generator that triggers AOM's at specific delay times with a certain phase relative to the TOP rotation. The duration of the AOM pulse is also adjustable. We use the following different pulse sequences to reach the:

• $F = 1$ **state**: Turn off the $F = 2 \rightarrow F = 3$ MOT light 1 ms before turning off the $F = 1 \rightarrow F = 2$ bypass repump light (figs. 5.9b and 5.11b, resp.), followed by 72 pulses (each 400 $\mu$s long, 550 $\mu$s apart when the TOP trap rotation frequency is 1800 Hz) from a 1 mW beam blue-detuned 9 MHz from the $F = 2 \rightarrow F = 2$ and $\sigma-$ polarized. The 2-2 light depumps the $F = 2$ state preferentially into the $F = 1, m_F = -1$ state.

• $F = 2$ **state**: Keep repump light on while the $F = 2 \rightarrow F = 3$ light is turned-off and apply approximately 10 pulses (each 125 $\mu$s long) of 2-2 light with $\sigma+$ polarization to populate the $F = 2, m_F = 2$ state.

• $F = 1$ **and** $F = 2$ **states**: Modify the $F = 1$ sequence, reducing the time-delay between turn-off of the $F = 2 \rightarrow F = 3$ and the $F = 1 \rightarrow F = 2$ bypass repump light to less than 1 msec and reduce the number of $2 - 2$ pulses to achieve the desired relative mixture of states.

The fractional efficiency of transferring the initial atom sample into the TOP trap, in either the $F = 1$ or the $F = 2$ atomic state, is about 40-45%. This number is a lower estimate to the optical pumping efficiency since other factors associated with the TOP trap limit the transfer (see below).

### 5.6.6 TOP Trap

Finally, we turn-on the TOP magnetic trap. There are several important considerations for selecting the initial trap parameters. First, we must

match the frequency of the TOP to the characteristic frequency for the atom cloud defined by the spatial size and velocity spread of the atoms. Otherwise, breathing modes are excited in the cloud that can be transformed into heat, via anharmonic mixing. Second, the TOP trap must be sufficiently deep to contain most of the molasses-cooled atoms. The depth of the TOP trap is $\frac{1}{2}\frac{\mu}{k_B}B_{TOP}$, where $\mu$ is the magnetic moment of the trapped state, and so a large trap depth requires a large bias field. Third, the quadrupole gradient must be small enough that the radius of the orbiting quadrupole zero ($B_{TOP}/B'_z/2$) is much larger than the atom cloud, which prevents spin-flip losses induced by the field zero. We begin the TOP trap, for $F = 1$ atoms, with an axial field gradient of 157 G/cm and a rotating bias field of 50 G (Fig. 5.10, a and b) to create a trap depth of 840 $\mu$K, orbital radius of quadrupole zero of 3200 $\mu$m and trap frequency of 20 Hz axially (7 Hz radially). We then adiabatically ramp the gradient to 226 G/cm over 1 sec (Fig. 5.10a), increasing the trap frequency to 29 Hz (10 Hz), to slightly increase the elastic collision rate as a prelude to evaporative cooling. At the end of the transfer, we observe $40 - 45\%$ of the original $1 - 2 \times 10^9$ MOT atoms are loaded into the TOP trap.

## 5.7 RF Evaporative Cooling

### 5.7.1 Forced Evaporative Cooling through Induced RF Transitions

The TOP and Ioffe-Pritchard magnetic traps confine atoms in the low-field seeking states near the minimum in the magnetic potential. However, most of the spin states of the atoms are either untrapped or antitrapped by the field minimum (see Fig.1.1 and discussion in Section 1.1.5). These

non-trapped states provide a natural mechanism for releasing atoms from the magnetic trap by driving Zeeman transitions from the trapped and into the non-trapped states. For the typical magnetic fields involved (up to $50 - 100$ G) we can use RF radiation techniques, as opposed to microwave or optical methods that are more difficult to implement. Evaporation is performed by tuning the RF to induce transitions in atoms in the largest magnetic fields, which corresponds to the highest energy trapped atoms, and allowing the remaining sample to rethermalize to lower temperature. By ramping the RF to lower frequencies we remove more energy from the sample so that it rethermalizes to lower temperature. The general principles of evaporative cooling for atomic systems were first discussed by H. Hess in 1986 [53]. The process of RF evaporation was proposed by D. Pritchard [115].

### 5.7.2 Coupling rf to the atoms

In our experiment, the rf magnetic field is applied to the atoms with an amplified rf drive to one of the anti-Helmholtz coils of the quadrupole field. This generates a magnetic field that oscillates parallel to the coil symmetry axis and orthogonal to the quantization axis of the atoms (defined by the rotating bias field). The rf field can therefore drive transitions between the trapped and untrapped Zeeman sublevels.

The entire coupling circuit is shown in Figure 5.12. The RF is generated by a $0 - 100$ MHz GPIB controlled frequency synthesizer. The amplitude is adjusted with a voltage controlled attenuator, and then the signal is amplified by a constant 30 dB RF amplifier. The output is connected to the anti-Helmholtz coil through a pair of 0.68 $\mu$F capacitors. For a typical frequency of 5 MHz, the coil inductance has an impedance of 150 $\Omega$, compared to

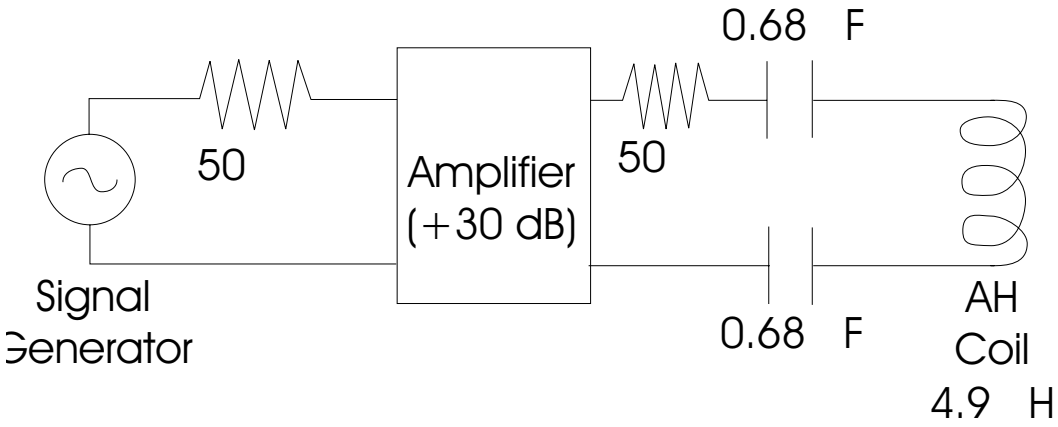


Figure 5.12: Circuit for coupling an rf magnetic field to the atoms for forced evaporative cooling

only 50 mΩ for the capacitors. At higher frequencies the impedance continues to be dominated by the coil inductance. At the low frequency end, we rarely go below 4 MHz during evaporation. Thus, the effective load is always seen as purely inductive.

### 5.7.3 Control of RF frequency and amplitude

One encounters several typical problems in this RF coupling scheme. First, the impedance decreases during the RF ramp-down. We compensate for the increased power delivered to the atoms by increasing the attenuation as the frequency is lowered. Second, RF frequency generators have a finite time response to commands for changing their output frequency, which is typically $10 - 50$ msec. We exercise care to allow the generator frequency to stabilize during the ramp. Last, due to different internal circuits that cover different frequency ranges, frequency generators sometimes exhibit unusual frequency jumps as the frequency changes. We found the best solution is to use another synthesizer.

### 5.7.4 Initial Conditions for Evaporation and Limitations to Efficiency

The key to making runaway evaporative cooling is having a ratio of the cloud's rethermalization rate to loss rate that is at least $100 - 200$. The rethermalization rate is simply the elastic collision rate divided by a factor of $\approx$ 2.8 (as determined by Monte Carlo simulations [157]). In the UHV environment of the Science cell the loss rate due to background gas is typically 0.002 $\text{sec}^{-1}$. Another loss process is the scattering of stray photons by magnetically trapped atoms. Scattering can heat the atoms out of the trap and cause spin-flips into

untrapped states. We found that this can be a serious limitation to magnetic trap lifetimes. We darken the Science cell, during the magnetic trapping phase of the experiment, using the following measures:

• Multiple layers of cardboard light baffles between lasers and apparatus

•Black plastic enclosure around the Science cell

•Cardboard enclosures around most mechanical shutters

•Isolate the repump laser in a separate cardboard enclosure to suppress unintended optical pumping of atoms from the $F = 1$ state into the $F = 2$.

The other inelastic loss important to $^{87}$Rb is due to three-body recombination. The rate constant is $3.5 \times 10^{-30}$ cm$^6$/sec, suggesting a recombination lifetime in the initial stages of evaporation (when the density is perhaps only $10^{12}$ atoms/cm$^3$) of 8 hrs! However, because the 3-body rate scales as the square of the density this inelastic rate becomes important at densities approaching those typical of a BEC of $10^6$ atoms ($10^{14}$/cm$^3$)

When the trap losses are limited only by background collisions, the minimum rethermalization rate necessary for runaway evaporation is about 0.3 sec$^{-1}$, or an elastic rate of 0.7 sec$^{-1}$. Fortunately in $^{87}$Rb, the elastic collision cross-section is temperature-independent for the temperature range obtained via optical cooling. Thus, we can enhance the collision rate by adiabatically compressing the atoms because the elastic collision rate will scale as the square of the trap frequency.

### 5.7.5 Evaporation Protocol

Once the minimum conditions on collision rate are met, evaporative cooling works repeatably and is relatively insensitive to the exact details of the profile of RF frequency sweep and magnetic trap compression. We ini-

tially ramp up the quadrupole gradient and then use several exponential ramp sections to ramp down the RF frequency and TOP bias field. Exponential ramping the RF cut value, in which the ramp rate is time-independent, has the feature that, as the RF is swept down, the change in cut energy is always a constant fraction of the total energy per unit time. For each ramp stage we adjust the ramp rate and power of the RF. We increase the attenuation of the RF as the frequency is ramped down to compensate for the decreasing impedance of the RF coil. We are not overly generous in the amount of RF power. Using more RF power than necessary to drive the RF transitions has the effect of power broadening the transition probability, which reduces the energy selectivity of the RF knife and the evaporation efficiency. The RF ramp can proceed only as fast as the cloud rethermalizes and cools. Ramping faster unnecessarily removes atoms that would rethermalize, also reducing efficiency.

In the computer program which runs the experiment, the workhorse procedure for our evaporation is a routine called coolexp. This routine ramps the RF frequency and TOP bias field, simultaneously, or either one separately. Coolexp is called with seven arguments: Coolexp $V_i$, $V_f$, $f_i$, $f_c$, $f_f$, $\alpha$, $\beta$. The first two parameters $V_i$ and $V_f$ are the initial and final control voltages for the ramp of the TOP bias field. $f_i$ and $f_f$ are the initial and final RF frequencies of the ramp, while $f_c$ indicates the frequency corresponding to the center of the trap. When $f_c = 0$ Eqs. (5.1) show that the RF and bias field ramp together. The profiles look like:

$$f_{RF}(t) = (f_i - f_c)exp((\alpha_r + \beta_r t)t) + f_c \tag{5.1a}$$

$$B_{TOP}(t) = B_{TOP}(0)exp((\alpha_t + \beta_t t)t) \tag{5.1b}$$

$$\alpha_r = \alpha \tag{5.1c}$$

$$\beta_r = \beta \tag{5.1d}$$

$$\alpha_t = \alpha \ln\left(\frac{V_f}{V_i}\right)\ln\left(\frac{f_f - f_c}{f_i - f_c}\right) \tag{5.1e}$$

$$\beta_t = \beta \ln\left(\frac{V_f}{V_i}\right)\ln\left(\frac{f_f - f_c}{f_i - f_c}\right) \tag{5.1f}$$

Notice that the exponential ramp in coolexp actually employs a rate constant that increases linearly with time: $\alpha_i + \beta_i t$. This allows additional flexibility to increase the ramp rate during a single Coolexp ramp.

In Tables 5.2 and 5.3 I present the specific evaporation steps we typically use for cooling atoms in the $F = 1$ and $F = 2$ states, respectively. The differences in profiles arise largely from two facts. First, atoms in the $F = 2$ state experience trap frequencies which are a $\sqrt{2}$ larger than for atoms in the $F = 1$. Hence, collision rates are higher in the $F = 2$ for clouds of comparable number. Secondly, loss rates for the two states differ slightly, favoring slightly different ramp rates to obtain optimal efficiency. Due to the long magnetic trap lifetimes, we can begin evaporation at any time after the atoms are loaded into the trap. We use this flexibility to initialize various flags, long-time-constant filters and GPIB command sequences. Evaporation then follows the content

of Table 5.2 or 5.3. After the sequences are complete, the RF remains on for 400 msec at the final rf value which allows for passive evaporation and final rethermalization of the cloud. The RF amplitude is then ramped off via the attenuator, and an RF switch with 60 dB attenuation interrupts the signal path from the RF synthesizer to the amplifier.

### 5.7.6 Evaporation Round-Up

Here are some typical numbers for initial conditions before evaporation. For $F = 1$ atoms, we start with $1.5 \times 10^8$ atoms at a temperature of 62 $\mu$K and a peak density of $9.3 \times 10^{10}/\text{cm}^3$ in a $f_z = 45$ Hz, $f_x = 16$ Hz trap to reach initial elastic collision rates of 3.7 $\text{sec}^{-1}$. For atoms in the F=2 state, we start with $1.7 \times 10^8$ atoms at a temperature of 91 $\mu$K and a peak density of $1.2 \times 10^{11}/\text{cm}^3$ in a $f_z = 65$ Hz, $f_x = 23$ Hz trap to reach initial elastic collision rates of 5.7 $\text{sec}^{-1}$.

Let me conclude by discussing the robustness of the evaporation to specifics of the RF and spring constant ramp. If evaporation doesn't produce reliably large BECs there is usually only one problem: Initial conditions have deteriorated. A handful of problems that affect initial temperature and density are:

- Poor molasses or CMOT due to (i) misalignment or intensity imbalances of the MOT; or (ii) poor laser mode
- MOT and TOP not well-aligned and magnetic shims need adjustment
- Poor optical pumping

Second, a couple of problems degrade the magnetic trap lifetime:

- Insufficient baffling of laser light
- Build-up of Rb in Science cell (The TSP must be run briefly to sublimate

| Step No. | Command |
|---|---|
| 1 | RF synth at 0.5 dBm output power |
| 2 | ramp rf attenuator[a] control voltage $0 \rightarrow 3$ in 300 msec [b] |
| 3 | coolexp 0.85, 0.85, 80, 0, 67, -0.1, 0 [c] [d] |
| 4 | coolexp 0.85, 0.51, 70.2, 0, 42.1, -0.06, -0.001 |
| 5 | coolexp 0.51, 0.1, 42.1, 0, 8.26, -0.04, -0.01 |
| 6 | ramp rf attenuator control voltage $3 \rightarrow 2.68$ in 80 msec |
| 7 | coolexp 0.1, 0.1, 8.26, 4.13, 6, -0.18, -0.02 |
| 8 | ramp rf attenuator control voltage $2.68 \rightarrow 2.8$ in 80 msec |
| 9 | coolexp 0.1, 0.1, 6, 4.13, 4.8, -0.5, -0.06 |
| 10 | ramp rf attenuator control voltage $2.8 \rightarrow 2$ in 80 msec |
| 11 | coolexp 0.1, 0.1, 4.8, 4.13, finalrf, -0.17, -0.017 |

[a] Mini Circuits ZAS 3

[b] The amplitude ramps reduce motion of the cloud in the trap caused by RF transients that distort the magnetic trap.

[c] $B_{TOP} = 59 V_{TOP}$ where field is given in Gauss

[d] RF center frequency determined by the $g_F \mu_B / h B_{TOP}$ where $\mu_B$ is the Bohr magneton and $g_F = 1/2$ for $^{87}$Rb

Table 5.2: Evaporation steps for $F = 1$ atoms

| Step No. | Command |
|---|---|
| 1 | RF synth at $-14$ dBm output power |
| 2 | coolexp 0.85, 0.85, 80, 0, 67, -0.1, 0 |
| 3 | coolexp 0.85, 0.58, 70.2, 0, 47.9, -0.001, -0.005 |
| 4 | coolexp 0.58, 0.51, 47.9, 0, 42.1, -0.0075, -0.005 |
| 5 | coolexp 0.51, 0.11, 42.1, 0, 9.08, -0.05, -0.005 |
| 6 | coolexp 0.11, 0.11, 9.08, 4.54, 6, -0.15, -0.01 |
| 7 | coolexp 0.11, 0.11, 6, 4.54, finalrf, -0.1, -0.02 |

Table 5.3: Evaporation steps for $F = 2$ atoms

additional Titanium into the system and remove the excess Rb.)

## 5.8 Imaging System

### 5.8.1 Absorption

In the work described in this thesis, clouds of atoms are detected by imaging the shadow of the atomic sample, caused by atomic absorption of a near-resonance probe laser, onto a CCD camera. The F=2(1) atoms are illuminated with a short pulse ($10 - 30$ $\mu$sec) of $\sigma$+(-) polarized light with a frequency tuned 0-20 MHz near the $F = 2, m = +(-)2 \rightarrow F = 3, m = +(-)3$ cycling transition. For the $F = 1$ atoms, a brief pulse of light tuned near the $F = 1 \rightarrow F = 2$ transition optically pumps the atoms into the $F = 2$ state, so that they can scatter many photons on the cycling transition. The optical pulses are synchronized with the rotating bias field of the TOP which defines a quantization axis for the atoms.

The atoms are viewed either in the magnetic trap or, more typically, after a period of free-falling ballistic expansion lasting up to 20 ms. The expansion is often necessary because the FWHM spot resolution of the imaging system is approximately 6 $\mu$m while the spatial extent of the condensate in the trap is only $10 - 30$ $\mu$m. Expansion also helps to diminish the high (several 100) on-resonant optical depths of condensates which saturate the absorption image. In addition, high optical depth clouds behave like lenses for the probe beam, greatly distorting the image of the shadow. We refer to this phenomena as lensing. Depending on the choice of expansion time and frequency of trap prior to release of the atoms, we reduce the optical depth, after expansion, by a factor of about $10 - 20$. Similarly, adjusting the detuning of the probe light

from resonance effects a reduction of a factor of $10-30$ in the observed optical depth. Through judicious choice of detuning and expansion we usually observe an optical depth of $1-2$.

### 5.8.2 Optics and CCD Camera

The probe light is taken from the undeflected beam of the Master Oscillator (MO) laser after passing through an AOM. Recall that the AOM is used for offset-locking to the laser. We set the detuning of the probe beam by shifting the probe frequency with another AOM, whose center frequency is near 140 MHz, to counter the offset-lock frequency of 133.5 MHz. The shifted beam of the AOM is coupled into an optical fiber. The fiber spatially filters the probe beam and improves the beam-pointing stability. The beam has a Gaussian transverse profile equal to 1.9 mm FWHM at the Science cell. We typically operate at 230 $\mu$W of total power.

Figure 5.13 shows the imaging system for viewing cold atom samples. Two lenses in a telescope configuration (magnification 9.6) image the shadow of the cloud onto the CCD camera. The first lens is a 2.5 cm dia, $f = 6$ cm placed 5.9 cm from the atoms. For the smallest samples light scattered from the cloud is nearly at the focus of the first lens and is therefore nearly collimated as it travels to the second lens. The second lens of 3.8 cm dia and $f = 50$ cm is 20.5 cm away from the first lens, and 50 cm in front of the CCD array to bring the image into crisp focus. Both lenses are achromatic doublets to minimize spherical aberrations. The speed of the imaging is determined by the aperature of the window projected onto the first lens. That gives $f/\# = 6.0/1.7 = 3.6$ and a diffraction limited FWHM spot size of $1.02 \times 0.78 \times 3.6 = 2.9$ $\mu$m. The larger diameter of the second lens captures all the light from the first and

prevents vignetting of the image. For viewing clouds much hotter than BEC (typical of initial conditions in the magnetic trap) we add a de-magnifying telescope to increase the field-of-view to properly capture the entirety of these hot clouds.

We focus the imaging system on the atoms by viewing the tiniest cloud of atoms, usually a small BEC. It is impractical to move the first lens so we focus the system by moving the camera to find the image plane. We use several criteria to define "in-focus". First, we move the camera along the optical axis until we observe the smallest clouds and the largest optical depth with the probe tuned on-resonance. Because the lensing caused by the atoms is at its worst when the probe is one-half linewidth detuned to either side of resonance, we use small numbers of atoms viewed exactly on resonance. This procedure usually yields a rather wide range of camera positions around the minimum cloud size. We narrow-in on the image plane by exploiting the lensing of the atoms. We detune to either side of resonance and recording the clouds' optical depth, which changes with the camera position due to the lensing effect. Moving the camera in a given direction through the image plane the optical depth either increases or decreases depending on the sign of the detuning. The intersection of the two curves of optical depth vs. position should occur at the image plane. Focusing the system in this way we achieved minimum FWHM spot sizes of 6 $\mu$m. These spots are clearly not diffraction limited. The large minimum spot-size probably results from some residual spherical aberrations in the optical system, but we have not worked to isolate the source or improve upon the present resolution limit.

The shadow of the atom cloud is recorded on a triggerable Charge-Coupled Device (CCD) camera. The camera output is digitized by a separate

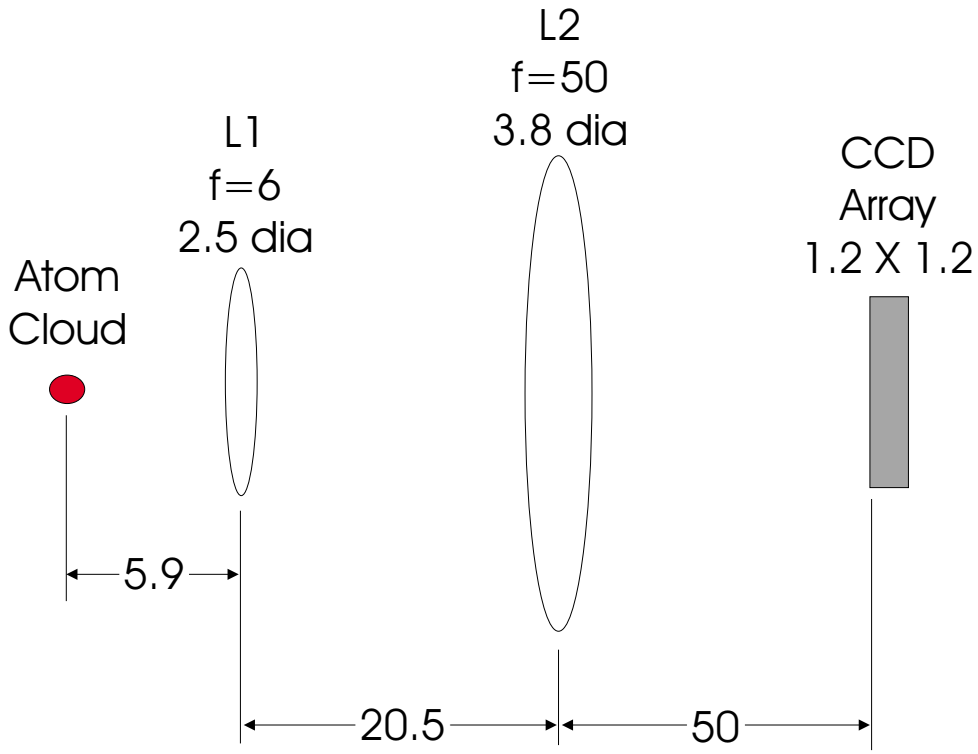


Figure 5.13: Schematic of the imaging system. Dimensions are in cm and the drawing is not to scale.

electronic controller and the images are processed with numerical fitting routines. Camera, controller and software controls are commercially obtained (Princeton Instruments), while the control software was written in-house. The CCD is housed in a vacuum environment and cooled with a thermoelectric cooler(unused). The CCD is a back-illuminated array, manufactured by SITe, has $512 \times 512$ pixels for an overall size of $12.3 \times 12.3$ mm. The pixels are 24 $\mu$m. The combination of back-illumination and a VIS/AR coating make the quantum efficiency 65% at 780 nm. The dynamic range of each pixel is 12 bits. The controller operates in 12 bit (500 kHz) or 16 bit (150 kHz) modes. Finally, the specified readout noise is very low: 4-7 electrons at 50 kHz and 18-21 at 1 MHz.

### 5.8.3 Basic Imaging Procedure

In absorption, the observable is the optical depth ($OD$) of the atomic sample at each point in space. For intensities of probe light, $I_0$, that are small compared to the saturation intensity, $I_s$, the intensity $I(\vec{r})$ transmitted through the cloud is given by Beer's Law:

$$I(\vec{r}) = I_o e^{-OD(\vec{r})} \tag{5.2}$$

where $OD(\vec{r}) = \int n(\vec{r})\sigma_o \mathrm{d}z$, $n(\vec{r})$ is the density distribution of the sample and $\sigma_o$ is the on-resonant optical cross-section at zero intensity. By detecting the normalized transmission of the probe we deduce the spatial profile of the cloud's $OD$:

$$OD(\vec{r}) = \ln\left(\frac{I_o}{I(\vec{r})}\right) \tag{5.3}$$

In practice, we measure optical depth by taking three images. First, we image the atoms with the probe light (Shadow Frame). Second, we dump the atoms from the trap and, approximately 1 sec later, record an image with only the probe light present (Normalization or Light Frame). Finally, with no light present at all, we record a Dark Frame that contains any electronic noise or offsets not due to light or atoms. In the final processing we calculate the $OD$ by subtracting the dark frame from both the light and shadow frames, divide them and take their natural log on a point-by-point basis:

$$OD(\vec{r}) = \ln\left(\frac{I_{\text{light}} - I_{\text{dark}}}{I_{\text{shadow}} - I_{\text{dark}}}\right) \tag{5.4}$$

If the probe light intensity is much more than $0.1I_{\text{s}}$ the optical transition begins to saturate and the fractional absorption is no longer proportional to the $OD$. The clouds look broader and flat-topped as a result and the total number of atoms is systematically under-counted. For a given probe beam intensity, we can correct the optical depth for saturation effects using the appropriate generalization to Beer's Law (in differential form):

$$\frac{\mathrm{d}I}{\mathrm{d}z} = -n(\vec{r})\sigma_o \frac{I}{1+I} \tag{5.5}$$

where I've redefined $I \rightarrow I/I_{\text{s}}$. The useful form for correcting the observed,

saturated $OD_{\rm s}$ to the true $OD_{\rm us}$ is:

$$OD_{\rm us} = OD_{\rm s} + (1 - e^{-OD_{\rm s}})I \tag{5.6}$$

### 5.8.4 Detailed Imaging Protocol

In the following section I explain the experimental implementation of the absorption imaging procedure in our system. After we complete an experiment with a condensate, we want to rapidly turn-off the magnetic trap to create a ballistic expansion of the cloud. The rapid turn-off is necessary to non-adiabatically release the atoms from the trap. In practice, our quadrupole coils turn-off in just under 1 ms - long enough to affect the release of atoms.

We circumvent the slow turn-off of the quadrupole field by initiating the drop with a fast decrease of the TOP spring constant. This is possible because we can rapidly change the TOP bias field ($B_{TOP}$) and hence the trap spring constant scales as $1/B_{TOP}$. In the example shown in Figure 5.14, the atoms are released from a TOP trap with $B_{TOP} = 3.3$ G and $B\prime_z = 89$ G/cm by first increasing $B_{TOP}$ to 50 G (Fig. 5.14a) and then starting the quadrupole gradient turn-off 1/3 msec later (Fig. 5.14b). 1.33 ms after the release is begun, we switch $B_{TOP}$ back to the lower trap field of 3.3 G (Fig. 5.14a), using a filtered control voltage to ensure a quiet, homogeneous magnetic field while the atoms drop and ballistically expand. As shown in Figure 5.14, we image the atoms after a total of 21 msec. The imaging is initiated by triggering the camera 9 msec before the probe beams flash, to allow for camera processing time (Fig. 5.14e). Next, we open the shutters to the probe and optical repump beams $1 - 2$ msec before the beams are flashed on (Fig. 5.14, c and d).

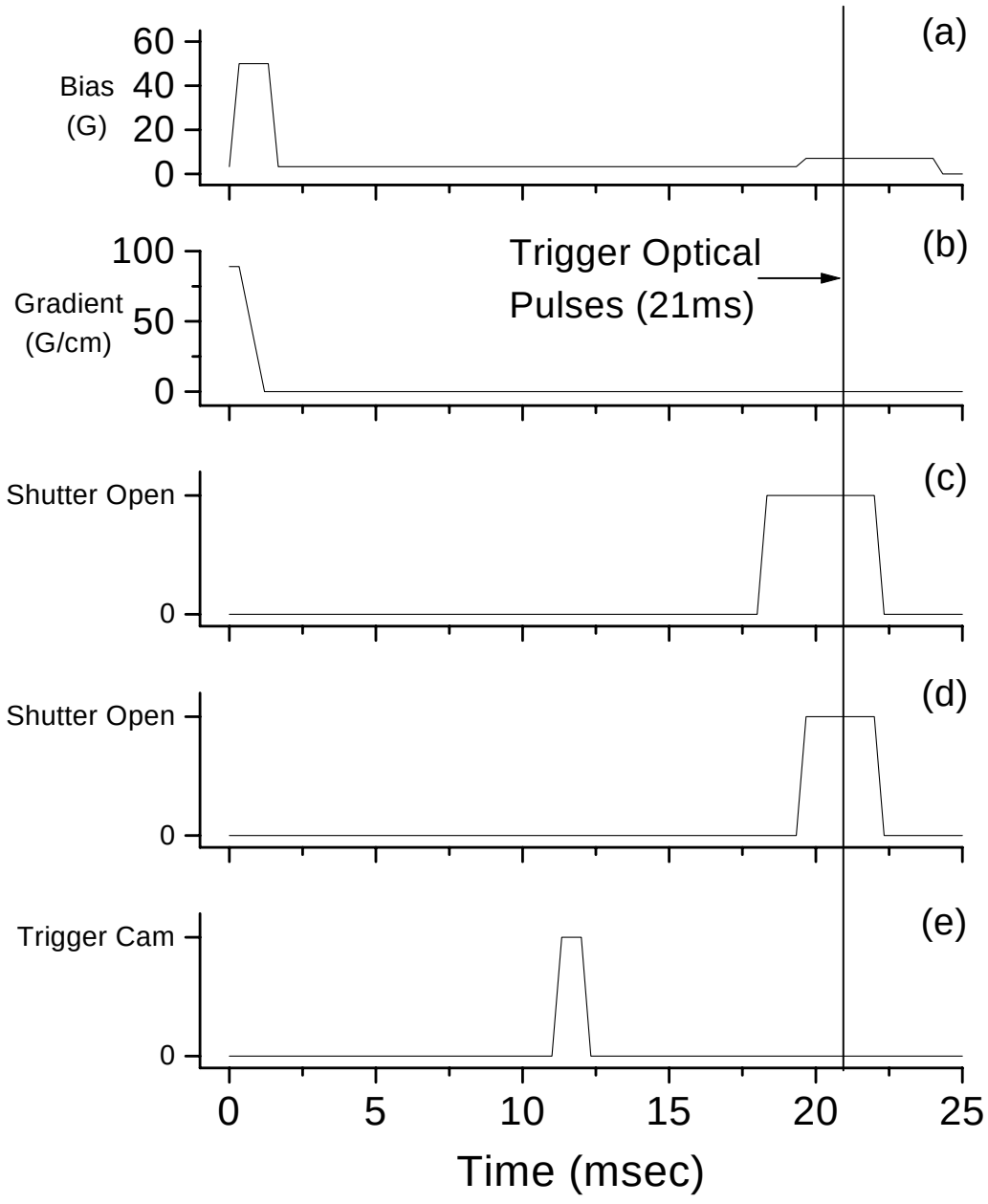


Figure 5.14: Timing of the Shadow Frame. The cloud is ballistically expanded for 21 ms from a TOP trap of $B'_z = 89$ G/cm and $B_{TOP} = 3.3$ G. The frames refer to: (a) TOP Bias field amplitude; (b) Axial Quadrupole field gradient; (c) Probe Repump Shutter; (d) Probe Shutter; (e) Camera Trigger

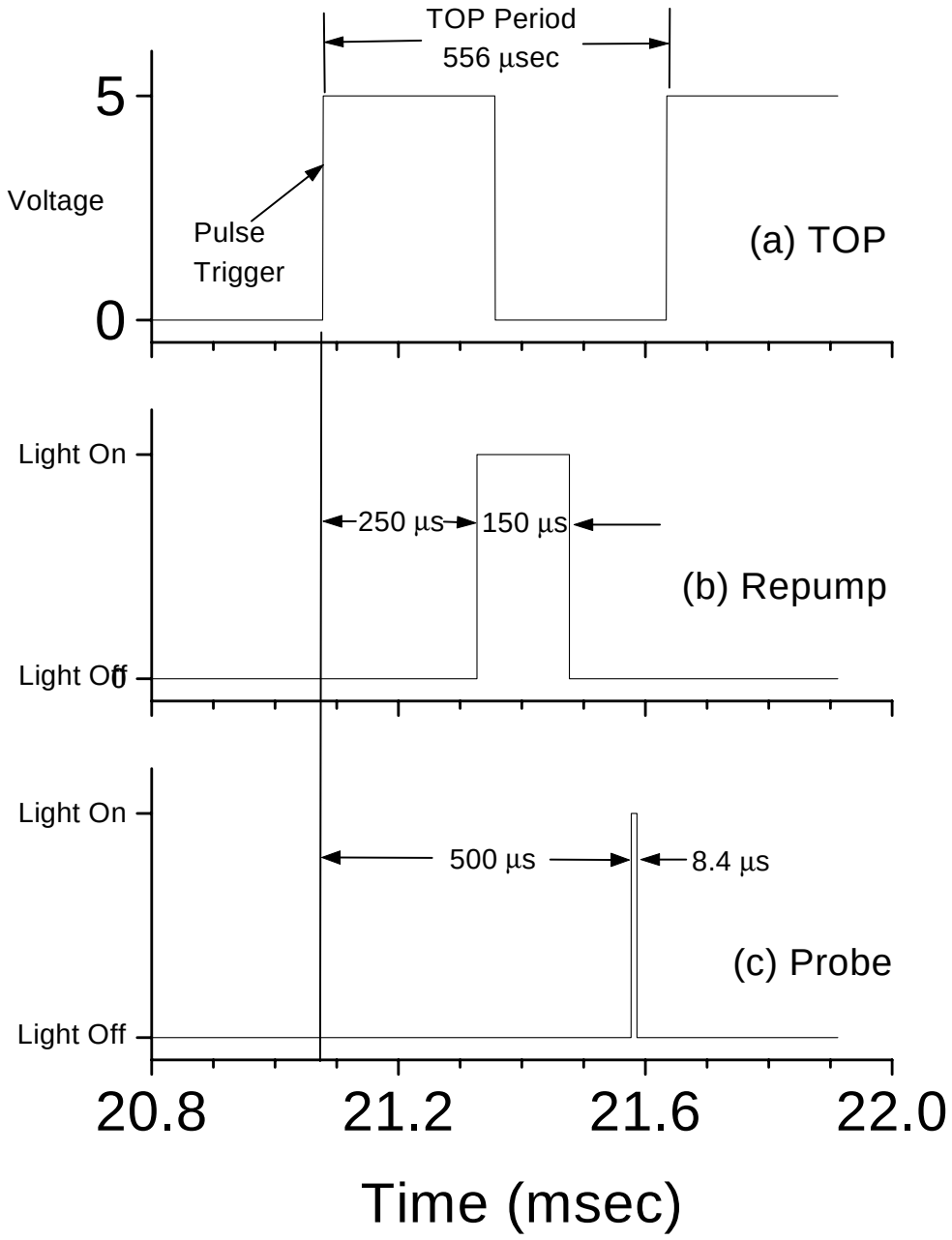


Figure 5.15: Timing of the (b) Repump and (c) Cycling-Transition Probe Pulses, synchronized to the (a) TOP bias rotation frequency (1800 Hz). The timing refers to imaging a dropped cloud of $F = 1, m_F = -1$ atoms as in Fig. 5.14

When the probe pulses are triggered at 21 msec we then enter into a critical timing phase. To insure that the optical beams are parallel with the rotating bias field, we synchronize the turn-on of the repump and probe beams with the TOP field rotation. The repump light turns-on first, 250 $\mu$sec after the first rising edge of the TOP trap Synch signal. The repump light is incident on the atoms, but does not shine into the camera. The repump lasts 150 $\mu$sec to completely pump the atoms into the $F = 2$ state. The probe light turns on 250 $\mu$sec later. To image the $F = 2$ atoms we only omit the initial flash of the repump light.

# Chapter 6

# The Time-Averaged Orbiting Potential Magnetic Trap

## 6.1 Introduction

Magnetic trapping is a powerful technique to manipulate and confine cold atoms. For many experiments, including BEC, a purely magnetic trap circumvents the limitations which prevent the simultaneous achievement of high densities ($\lesssim 10^{12}$ atoms/cm$^3$) and low temperatures (at or below the recoil limit) in optical traps. The first magnetic trap realized for neutral atoms was the quadrupole magnetic trap [83]. Some early experiments to achieve BEC focused on quadrupole traps due to their simplicity, their integral nature as part of a MOT apparatus and their tight confinement [21, 104]. In addition, BEC experiments need long trap lifetimes for successful evaporative cooling. On this count, quadrupole traps fail: Atoms are ejected from the trap by Majorana spin-flips [160] near the central zero-field region [21, 104]. The Time-averaged Orbiting Potential (TOP) magnetic trap [21] successfully modified the quadrupole potential to permit long trap lifetimes and enable the first observation of BEC in a dilute vapor of $^{87}$Rb [22]. Another solution to the Majorana problem is to use a Ioffe-Pritchard (IP) magnetic trap [82] which has a non-zero magnetic field at its potential minimum. Shortly after the success in the TOP trap, several experiments used a variety of different IP

magnetic traps to achieve BEC [142, 121, 122, 161, 162]. In spite of the success of the IP traps, TOP traps continue to be used in several BEC experiments with $^{87}$Rb [163, 164, 165, 166] and $^{23}$Na [167], as well as experiments with $^{133}$Cs [168, 169, 170].

Magnetic fields can exert forces on atoms by interacting with an atom's magnetic moment $\vec{\mu}$. The interaction between a magnetic moment and a magnetic field $\vec{B}$ is given by the familiar Hamiltonian $H = -\vec{\mu} \cdot \vec{B}$. The potential energy of atoms that are spin aligned with the field increases as the magnetic field increases. Thus, atoms experience a force towards lower magnetic fields, and by creating a local minimum in the magnetic field we can confine these so-called "weak-field seeking" states. The Time-averaged Orbiting Potential (TOP) creates a time-average minimum in a time-dependent magnetic field consisting of a static spherical quadrupole magnetic field plus a uniform bias field rotating at frequency $\omega_{\mathrm{T}}$ [21]. The uniform field displaces the zero point of the quadrupole magnetic field from its static position and moves the point in a circular orbit. The TOP will confine the atoms as long as two conditions on the rotation frequency of the bias field are satisfied. First, the bias field must rotate fast compared with the oscillation frequency $\omega$ of atoms in the potential such that the net force of attraction of the atoms will be towards the center of the quadrupole orbit. We call this the time-averaging condition, which we state formally as

$$\omega_{\mathrm{T}} \gg \omega. \tag{6.1a}$$

If the field rotates too quickly the magnetic moments are unable to follow the

field adiabatically. The atoms then make transitions from trapped to untrapped spin-states. The upper bound on $\omega_{\mathrm{T}}$ is determined by the Larmor frequency-splitting between spin states of an atom in a magnetic field $\omega_{\mathrm{L}} = \mu|\vec{B}|/\hbar$. We call the upper bound on the TOP rotation frequency the adiabaticity condition, which is formally expressed

$$\omega_{\mathrm{T}} \ll \omega_{\mathrm{L}}. \tag{6.1b}$$

The subject of the present chapter is a detailed study of the properties of, and the limitations to, the TOP magnetic trap. Historically, IP traps have been studied in much greater detail than the TOP trap [82, 171, 92, 157, 114, 121, 152]. Very little experimental work has appeared in the literature about the TOP trap beyond the initial demonstration [21] and its role in various BEC experiments [22, 8, 172, 164]. There have been some theoretical treatments of the TOP [173, 174, 175, 176, 177]. In the first part of this chapter we present a detailed and improved theoretical description of the TOP that includes the effects of gravity. We find corrections to the trap frequencies that offer control over the trap symmetry through the sag of atoms in the trap. The TOP is only an approximately harmonic trap, so we also calculate anharmonic contributions to the potential. We find that the anharmonicities of the TOP become lower when the trap is made more spherical. We further generalize the TOP theory for non-isotropic rotating bias fields. In the latter section of the chapter we present a series of measurements of the TOP trap. First, we verify the improved theory of the TOP by precisely measuring the trap frequencies and aspect ratios. Next, we determine limitations to TOP performance through

measurements of the loss of atoms from the trap when the TOP is operated in various extremes of operation. As our first experiment, we studied the lifetime of atoms in the TOP as a function of the bias field, from just over 6 Gauss to a very small value of 200 mG. The low-field regime is particularly interesting because recent experiments suggest that a low bias field trap is necessary to observe BEC in $^{133}$Cs [178]. In our second study of extreme operation, we test the fundamental conditions, 6.1, of the TOP by varying the rotation frequency of the bias field. We measure loss of atoms from the TOP trap for a range of rotation frequencies covering nearly three orders-of-magnitude.

## 6.2 Theory of the Time-Averaged Orbiting Potential

### 6.2.1 Basic Theory

The complete potential of a TOP Magnetic trap consists of the sum of the total magnetic potential and the gravitational potential. Previous work neglected the effects of gravity [21] but, as we will show, gravity can have a profound influence on the qualitative features of the trap. We begin by briefly reproducing the results of [21] so we can later contrast them to the results including gravity. The quadrupole magnetic field is cylindrically symmetric about an axis parallel to the vertical defined by gravity. We write the quadrupole field, to lowest order in its spatial coordinates near the center of the anti-Helmholtz coil pair that generates the field, as:

$$\vec{B}_{\rm q} = B'_z(\frac{1}{2}x\hat{x} + \frac{1}{2}y\hat{y} - z\hat{z}), \tag{6.2}$$

where $B'_z$ is the axial magnetic field gradient. The bias field rotates in a plane orthogonal to the axis of the quadrupole field that we write as:

$$\vec{B}_{\rm b} = B_0 \cos(\omega_{\rm T} t)\hat{x} + B_0 \sin(\omega_{\rm T} t)\hat{y} \tag{6.3}$$

where $B_0$ is the bias field and $\omega_{\rm T}$ is the angular frequency at which the bias field rotates. When condition 6.1b is satisfied, the atomic magnetic moments $\vec{\mu}$ adiabatically follow the magnetic field and only the magnitude of the total field is important for calculating the magnetic potential energy:

$$U_{\rm magnetic}(\vec{r}, t) = \mu |\vec{B}_{\rm q} + \vec{B}_{\rm b}| \tag{6.4}$$

$$= \mu \sqrt{(\frac{B'_z}{2}x + B_0 \cos(\omega_{\rm T} t))^2 + (\frac{B'_z}{2}y + B_0 \sin(\omega_{\rm T} t))^2 + (B'_z z)^2} \tag{6.5}$$

In practice the atoms are confined far from the rotating quadrupole zero and very near the trap minimum at temperatures small compared with the trap depth. In other words, the region of interest in the potential is for distances $r$ from the trap center small compared with the radius of the orbit of the quadrupole zero, $R \equiv B_0/B'_z/2$. The radius $R$ is the natural length scale for the problem and we can rewrite $U_{\rm magnetic}$ in terms of $r/R$:

$$U(\vec{r}, t) = \mu B_0 \sqrt{(\frac{x}{R} + \cos(\omega_{\rm T} t))^2 + (\frac{y}{R} + \sin(\omega_{\rm T} t))^2 + (2\frac{z}{R})^2} \tag{6.6}$$

We expand the potential and time-average over a bias rotation period. Keeping the lowest non-zero terms in $r/R$ we obtain:

$$U_{TOP}(\vec{r}) = \frac{1}{2\pi}\int_0^{2\pi} U(\vec{r},t)\,\mathrm{d}t$$

$$= \mu B_0 + \frac{1}{2}\frac{\mu B_z'^2}{8B_0}(x^2+y^2) + \frac{1}{2}\frac{\mu B_z'^2}{B_0}z^2 + \ldots \tag{6.7}$$

The bias field at the center of the trap is the applied TOP bias $B_0$. The time-average potential is harmonic in all three dimensions and the spring constants are analytic functions of the magnetic moment, quadrupole gradient and TOP bias field. Radial symmetry about the TOP rotation axis is preserved and the axial ($z$) spring constant is 8 times larger than the radial ($x, y$) spring constants. It is useful to consider typical parameters of bias field and field gradient to choose $\omega_{\mathrm{T}}$. For a field gradient of $B_z' = 200$ G/cm and applied TOP bias $B_0 = 5$ G, the axial trap frequency $f_z = 80$ Hz and the Larmor frequency $f_{\mathrm{L}} = 3.5$ MHz. Therefore, a TOP bias rotation frequency of a few kHz satisfies both criteria of time-averaging (6.1a) and adiabaticity (6.1b) by two orders-of-magnitude. The first TOP trap [21] achieved long trap lifetimes ($\gtrsim 100$ sec) using $\omega_{\mathrm{T}} = 2\pi \times 7.6$ kHz. In Section 6.6 we describe a systematic study that experimentally tests the TOP criteria 6.1.

### 6.2.2 Effects of Gravity

The previous treatment breaks down when gravity causes the minimum of the total magnetic plus gravitational potential to sag significantly from the center of the quadrupole field. The total potential including gravity is

$$U(\vec{r},t) = \mu\sqrt{(\frac{B'_z}{2}x + B_0\cos(\omega_{\rm T}t))^2 + (\frac{B'_z}{2}y + B_0\sin(\omega_{\rm T}t))^2 + (B'_z z)^2} + mgz \tag{6.8}$$

where $m$ is the mass of an atom and $g$ is the acceleration due to gravity. The equilibrium position for atoms is the position which minimizes $U(\vec{r},t)$:

$$\vec{r}_{\rm min} = -\frac{R}{2}\frac{\eta}{\sqrt{1-\eta^2}}\hat{z} \tag{6.9}$$

For convenience I define $\eta \equiv \frac{mg}{\mu B'_z}$. Physically, $\eta$ is the ratio of the weight of an atom to the magnetic force from the axial quadrupole gradient that supports it. We expand $U(\vec{r},t)$ in powers of $|\vec{r}-\vec{r}_{\rm min}|/R$ and time-average:

$$U_{\rm TOP}(\vec{r}-\vec{r}_{\rm min}) = \frac{1}{2\pi}\int_0^{2\pi} U(\vec{r}-\vec{r}_{\rm min},t)\,{\rm d}t$$

$$\begin{aligned} = \quad & \mu B_0\sqrt{1-\eta^2} + \frac{1}{2}\frac{\mu B'^2_z}{8B_0}(1+\eta^2)\sqrt{1-\eta^2}(x^2+y^2) + \\ & \frac{1}{2}\frac{\mu B'^2_z}{B_0}(1-\eta^2)^{3/2}z^2 + \ldots \end{aligned} \tag{6.10}$$

Several new features emerge. First, the total offset in the potential vanishes as the atoms sag more in the trap ($\eta \to 1$). This occurs because the potential energy due to the magnetic bias field is cancelled by the decrease in gravitational potential energy as the atoms sag. Second, the potential remains harmonic to lowest order in the axial and radial directions and is cylindrically symmetric, but gravitational sag introduces factors depending on $\eta$ into the spring constants. The presence of factors like $1-\eta^2$ force the spring constants to vanish as $\eta \to 1$. As we expect, the potential can hardly be confining if it cannot support the atoms against gravity.

An even more important feature of the gravitational corrections is that the axial and radial spring constants are not identical functions of the quadrupole gradient. The aspect ratio is an analytical function of $\eta = \eta(B_z')$:

$$\frac{k_z}{k_r} = 8\frac{1-\eta^2}{1+\eta^2} \tag{6.11}$$

In the limit of large gradients the trap asymmetry approaches 8 and agrees with the calculation of Petrich, *et al.* [21]. By reducing $B_z'$, the aspect ratio is continuously decreased towards zero as the gradient is lowered towards the minimum to cancel gravity. The aspect ratio does not depend on the applied TOP bias field although the **net** bias field, at the center of the trap, does increase as the gradient decreases due to an increasing vertical component to the magnetic field from the quadrupole field. The net bias field is $B_0/\sqrt{1-\eta}$. An important special value of trap symmetry occurs when $\eta = \sqrt{\frac{7}{9}}$: The aspect ratio is 1 and the TOP is spherically symmetric.

| TOP Expansion | |
|---|---|
| term | coefficient |
| $r^2(z-z_{min})$ | $4\eta(1-\eta^2)(3\eta^2-1)\frac{\mu B_z'^3}{B_0^3}$ |
| $(z-z_{min})^3$ | $32\eta(1-\eta^2)^2\frac{\mu B_z'^3}{B_0^2}$ |
| $r^4$ | $1/4(1-\eta^2)^{3/2}(1+6\eta^2-15\eta^4)\frac{\mu B_z'^4}{B_0^3}$ |
| $r^2(z-z_{min})^2$ | $8(1-\eta^2)^{3/2}(1-12\eta^2+15\eta^4)\frac{\mu B_z'^4}{B_0^3}$ |
| $(z-z_{min})^4$ | $32(1-\eta^2)^{5/2}(5\eta^2-1)\frac{\mu B_z'^4}{B_0^3}$ |

Table 6.1: Higher-Order Terms in the TOP expansion

### 6.2.3 Anharmonicities

An important consideration for any nearly harmonic trapping potential is the magnitude of anharmonicities. Anharmonic components to the potential can impose serious systematic limitations to experiments by providing a mechanism for damping of excitation modes of a trapped cloud or the conversion of in-trap sloshing into cloud heating. We calculated the coefficients of the higher-order anharmonic terms of the TOP up to the quartic terms in the potential. See Table 6.1. Due to cylindrical symmetry the label $r$ means any direction perpendicular to the symmetry axis.

Reviewing the table we notice that all of the terms depend on the trap sag through $\eta$. Terms $r^2z$ and $r^2z^2$ couple motion in the axial and radial directions. Overall, the cubic and quartic terms introduce fractional corrections to the harmonic trap frequency $\omega_{0i}$ in the direction $i$ that depend on the square of the ratio of the amplitude of oscillation $A_j$, in all three dimensions $j = r, z$, to the radius $R$ [179]:

$$\overline{\Delta\omega/\omega} = \overline{\alpha}\,\overline{A^2} \tag{6.12}$$

where $\overline{\Delta\omega/\omega}$, $\overline{\alpha}$ and $\overline{A^2}$ are matrices defined by

$$\overline{\Delta\omega/\omega} = \begin{pmatrix} \frac{\omega_r - \omega_{0r}}{\omega_r} \\ \frac{\omega_z - \omega_{0z}}{\omega_z} \end{pmatrix} \qquad \overline{\alpha} = \begin{pmatrix} \alpha_{rr} & \alpha_{rz} \\ \alpha_{zr} & \alpha_{zz} \end{pmatrix} \qquad \overline{A^2} = \begin{pmatrix} \frac{A_r^2}{R^2} \\ \frac{A_z^2}{R^2} \end{pmatrix}$$

The $\alpha_{ij}$ are dimensionless coefficients depending on the quadrupole field gradient through the parameter $\eta$. After straightforward, but lengthy algebra we obtain the matrix of anharmonicity coefficients:

$$\overline{\alpha} = \begin{pmatrix} \frac{1}{64}\frac{1}{1+\eta^2}(3 + 7\eta^2 - 23\eta^4 - 3\eta^6) & \frac{1}{4}\frac{1-\eta^2}{1+\eta^2}(2 - 17\eta^2 + 9\eta^4) \\ \frac{1}{32}(2 - 17\eta^2 + 9\eta^4) & -\frac{3}{4}(1 - \eta^2) \end{pmatrix} \tag{6.13}$$

Since the off-diagonal elements are non-zero, the oscillation frequency in $r$ (and $z$) direction depends on the amplitudes of motion in both the $r$ and $z$ directions, *e.g.* $\omega_r = \omega_{0r}(1 + \alpha_{rr}(A_x/R)^2 + \alpha_{rz}(A_z/R)^2)$.

We first consider the off-diagonal elements of $\overline{\alpha}$. These elements arise solely from the mixing terms in the potential, $r^2 z$ and $r^2 z^2$. Recalling that the trap aspect ratio is 6.11, we note that both off-diagonal corrections to the trap frequencies are equal for $r$ and $z$ oscillations of equal energy. Applying similar reasoning, we can directly compare the fractional anharmonic frequency shifts due to both diagonal and off-diagonal terms. In Figure 6.1, we plot the

fractional anharmonic frequency corrections due to off-diagonal and diagonal terms, expressed in units of the square of the ratio of $A_r/R$, as a function of $mg/\mu B'_z$, or $\eta$. In general, the off-diagonal contributions are of the same order as the diagonal elements.

Next, we are interested in the total fractional frequency shift in the axial and radial directions, consisting of both diagonal and off-diagonal elements. Once again, we assume equal energy of motion in all directions and express the fractional frequency shifts in terms of the square of the ratio of radial amplitude to $R$. This allows (i) evaluation of the anharmonic shifts in a single frequency due to amplitudes of motion in both $r$ and $z$ directions, and (ii) comparison of the anharmonicity shifts in axial versus radial directions. The anharmonic frequency shifts are plotted versus $mg/\mu B'_z$ in Figure 6.2. The curves may be interpreted in the following way. Consider a motion in the trap whose total energy is $3/2k_{0r}A_r^2$ and is evenly divided among all three dimensions. Now, for example, let $A_r/R = 1$, which means that the amplitude of motion extends all the way to the orbit of the quadrupole zero. When $mg/\mu B'_z = 1$, Figure 6.2 shows that the fractional shift in the axial (radial) frequency is -0.375 (-0.3125). As expected, for an amplitude of motion far from the center of the TOP expansion there are substantial anharmonic corrections to the trap frequencies.

The changes in trap symmetry and anharmonicity differ slightly from previous experience with IP magnetic traps. Changing the IP trap symmetry from highly asymmetric with cylindrical symmetry to nearly symmetric usually comes with two prices. First, a large bias field is required to reduce the larger spring constant. Second, the anharmonicities in all directions worsen, often quite substantially. In contrast, the TOP trap aspect ratio tunes only

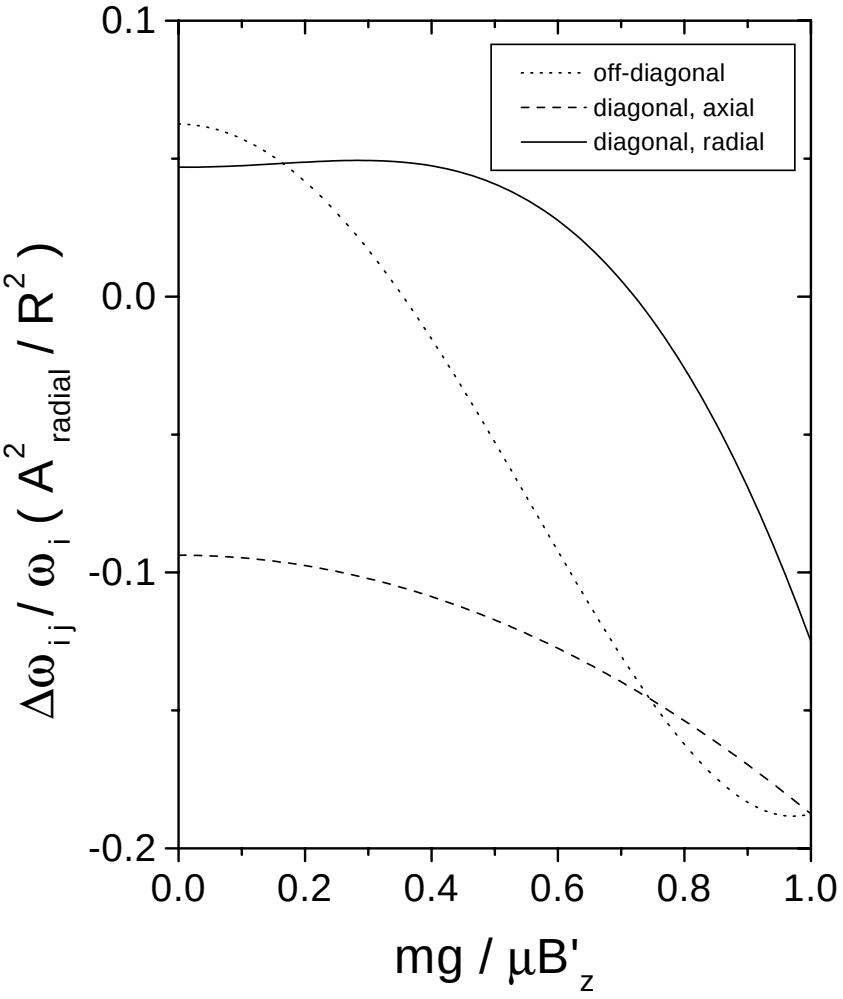


Figure 6.1: Comparison of the diagonal radial ($\Delta\omega_{rr}/\omega_r$, solid line), diagonal axial ($\Delta\omega_{zz}/\omega_z$, dashed line) and off-diagonal ($\Delta\omega_{ij}/\omega_i$, where $i \neq j$, dotted line) contributions to the fractional anharmonic frequency shift, as a function of $mg/\mu B'_z$, the ratio of atom weight to magnetic force. In general, $\Delta\omega_{\rm mn} = \omega_{\rm m} - \omega_{0\rm m}$, where $\omega_{0\rm m}$ is the zero-amplitude oscillation frequency in the mth direction. We assume the same energy of motion in axial and radial directions and express the fractional frequency shift in terms of the ratio $A_r^2/R^2$, where the $A_r$ is the radial oscillation amplitude and $R$ is the orbital radius of the quadrupole zero.

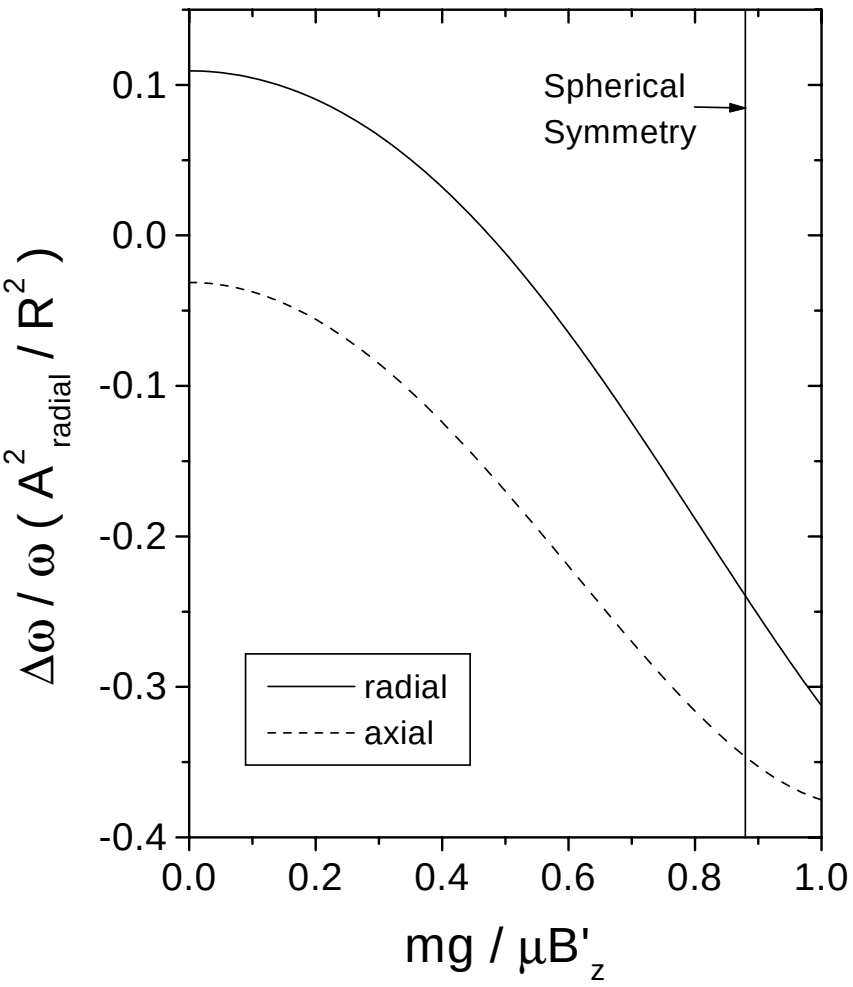


Figure 6.2: Plot of the fractional shift, $\omega_{\rm i} - \omega_{0\rm i}/\omega_{0\rm i}$ in the axial (i=$z$, dashed line) and radial (i=$r$, solid line) trap frequencies as a function of $mg/\mu B'_z$, the ratio of atom weight to magnetic force. To facilitate comparison of axial and radial frequency shifts, we assume the same energy of motion in axial and radial directions and express the fractional frequency shift in terms of the ratio $A_r^2/R^2$, where the $A_r$ is the radial oscillation amplitude and $R$ is the orbital radius of the quadrupole zero. The solid, vertical line indicates where the TOP has spherical symmetry (the zero-amplitude axial and radial frequencies are equal).

with the gradient. The **net** bias is affected, but as a second-order effect of the gradient. Regarding anharmonicities in the TOP, the above discussion shows that the magnitude of the fractional frequency shift generally increases as we decrease the quadrupole gradient and make the potential spherical. The fractional shift, however, is unchanged by the applied TOP field as long as the ratio $A_r/R$ is constant. It is also important to point out the magnitude of the fractional frequency shift can be quite small. For the worst anharmonicities, when $\eta = 1$, oscillation amplitudes less than $1/10\,R$ suffer less than a 1% fractional frequency shift. This is a typical ratio of radial condensate size to $R$, under reasonable experimental conditions.

### 6.2.4 Effect of Eccentricity on the TOP Trap

When the rotating bias field of the TOP is not radially symmetric several corrections occur to the TOP frequencies. Breaking of radial symmetry may be characterized as an eccentricity $e$ in the path of the quadrupole zero point. Eccentricity is almost unavoidable in a laboratory TOP trap because making a bias field that rotates with the same magnitude in all directions to better than 5% is difficult. Broken radial symmetry can subsequently alter the physics of excitations of trapped atom clouds or Bose-Einstein Condensates [8, 141]. Eccentricity also provides a tool for inducing excitations of various symmetries into a trapped atom cloud [180].

Consider a TOP trap in which the bias field in the $y$ direction is $e$ times larger in the $x$ direction, i.e. $B_{0x} = B_0$ and $B_{0y} = eB_0$. The rotating field becomes:

$$\vec{B}_{\rm b} = B_0 \cos(\omega_T t)\hat{x} + eB_0 \sin(\omega_T t)\hat{y} \tag{6.14}$$

For simplicity, we assume a large axial field gradient so we can ignore the sag due to gravity and the gravitational potential. The simplified total potential is

$$U_{\rm magnetic}(\vec{r},t) = \mu\sqrt{(\frac{B'_z}{2}x + B_0\cos(\omega_T t))^2 + (\frac{B'_z}{2}y + eB_0\sin(\omega_T t))^2 + (B'_z z)^2} \tag{6.15}$$

due to the combination of eccentric rotating field and the static quadrupole potential. As before, we expand the potential about its minimum ($\vec{r}_{\rm min} = 0$) and retain terms to second-order in $|\vec{r}|/R$. The eccentricity obviously breaks the cylindrical symmetry of the potential such that the time-averaged spring constants are not analytical functions of $e$. We numerically integrate the potential over a bias rotation period to obtain the time-averaged bias field and spring constants. We are interested in the dependence of symmetry breaking between the $x$ and $y$ spring constants on the eccentricity of the bias field. A complicating effect is that increasing $e > 1$ also increases the time-averaged magnetic field. We remove this complication by calculating the ratio of the $y$ frequency to the $x$ frequency so that the overt field-dependence of the frequencies cancel. The frequency ratio as a function of eccentricity is plotted in Figure 6.3. As the field along $y$ increases relative to the field along $x$, the frequency along $y$ decreases relative to the frequency along $x$. The dependence on eccentricity is rather slow: when $B_y$ is 50% larger than $B_x$ ($e = 1.5$), $\omega_y$ is

only 10% smaller than $\omega_x$. The weak dependence of $\omega_y/\omega_x$ on $e$ is also evident in an analytical expansion in the limit of small eccentricity:

$$\omega_x = (1 + \frac{1}{4}e)\,\omega_y. \tag{6.16}$$

We are also interested in knowing if the eccentricity changes the ratio of the axial frequency to the radial frequencies. A calculation of the ratio of $\omega_z$ to the mean radial frequency $(\omega_x + \omega_y)/2$ shows that the ratio is equal to $\sqrt{8}$ for all values of $e$. This is precisely the ratio expected for a cylindrically symmetric TOP with no eccentricity.

The insensitivity of the ratio of "radial" frequencies to the eccentricity is useful for ensuring near-cylindrical symmetry in the TOP trap. The isotropy of bias field in the rotation plane is typically no better than $5 - 10\%$. However, from Figure 6.3 and Equation 6.16 we note that the corresponding radial frequencies are split by no more than $1.25 - 2.5\%$. In the opposite extreme of large eccentricity, the frequency splitting can be very large (25% at $e = 3$) without a fundamental breakdown of the TOP trap.

## 6.3 Experimental Method

We experimentally study the TOP magnetic trap by creating cold clouds of $^{87}$Rb in a double-MOT apparatus and observing the behavior of the atomic velocity distributions. We will only review the apparatus as details are given elsewhere [172]. See also Chapter 5. A high-pressure ($\sim 10^{-9}$ Torr) vapor cell MOT creates ensembles of several $10^8$ atoms that are pushed with a resonant laser pulse into a second MOT maintained in a glass cell at very

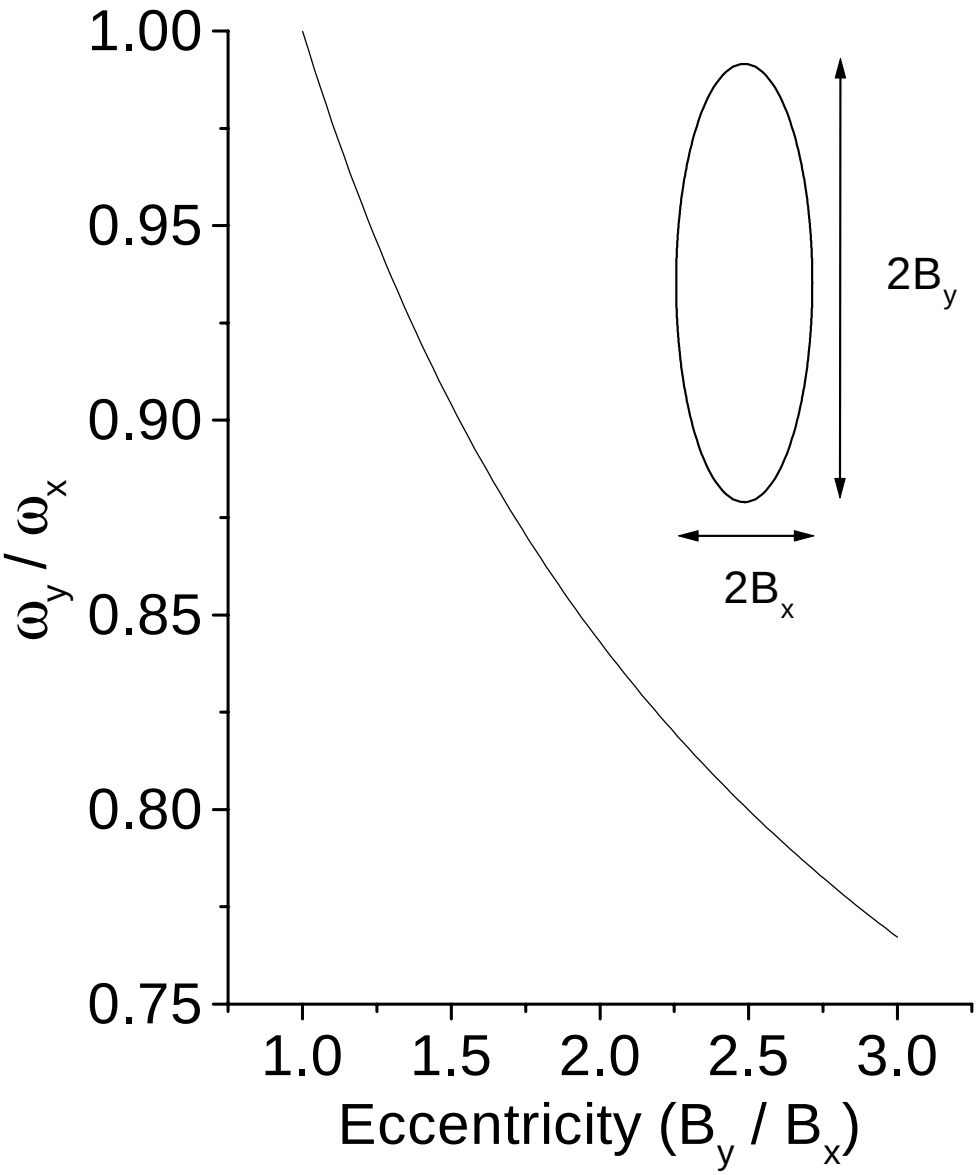


Figure 6.3: Ratio of $y$ to $x$ "radial" trap frequencies in an eccentric TOP trap.

low vapor pressure ($\sim 10^{-11}$ Torr). After twenty to thirty pulsed loading cycles, $10^9$ atoms are optically compressed (CMOT) and cooled (molasses) in preparation for loading into a purely magnetic trap. The atoms are optically pumped into the $5S_{1/2}F = 1, m_F = -1$ ($F = 1$) state of $^{87}$Rb and the magnetic fields for the TOP trap are turned-on. The spring constants of the magnetic trap are adiabatically ramped-up and a radio-frequency (rf) magnetic field is ramped-down in frequency to perform evaporative cooling. The final value of the rf frequency determines the final cloud temperature. After attaining a cloud of desired temperature and density using a standard configuration of magnetic fields and rf frequencies, we adiabatically ramp the trap to a new set of trap parameters (net bias field, amount of sag, frequency, etc.) and conduct experiments for an interaction and wait time (lasting tens of milliseconds to minutes). Exact details of this penultimate stage are described in the following experimental sections. After the interaction and wait, the atoms are released from the trap and ballistically expand for typically 21 msec. The expanded and dropped cloud is optically pumped from the $F = 1$ into the $5S_{1/2}F = 2$ ground-state and probed with an 8 $\mu$s pulse of light at a frequency tuned near the $5S_{1/2}F = 2, m_F = 2 \rightarrow 5P_{3/2}F = 3, m_F = 3$ cycling transition. The release and absorption imaging destroys the cloud. The absorption shadow of the atoms is imaged onto a CCD array and fit to a Gaussian, inverted parabola or double-Gaussian distribution function depending on if the atom cloud is a noncondensed gas, pure BEC, or a mixture of noncondensed and quantum degenerate gases, respectively. From the fits to the 2-D velocity distributions we extract all the relevant information about the sample: Total number, number in the condensate, temperature and position [13].

## 6.4 Trap Frequency and Symmetry Measurements

Accurate knowledge of trap parameters is crucial for extracting quantitative information from experiments with trapped particles. Nearly every physical parameter of interest – temperature, density, phase space density, size of ground state, etc. – is connected to knowledge of the trap frequencies. For example, the temperature of a classical gas is obtained from knowing the root-mean-square size of the gas in the trap and the trap frequency. In the following section we describe measurements of the frequency of oscillation of atoms in the TOP trap and the spatial symmetry of the trap. We compare these data to the improved theory of the TOP frequencies.

We measure trap frequency by exciting small-amplitude oscillations of our smallest clouds in the trap, recording the cloud's center-of-mass (CM) position versus time, and fitting the data to a single-frequency sine wave. We first create pure condensates as described above and then ramp the TOP to a particular field gradient and bias field. CM oscillations of the BEC are created in two complementary ways. First, an axial (vertical) CM oscillation is induced using a field ramp that is slightly non-adiabatic, causing a vertical slosh of the cloud as the atoms suddenly sag against gravity. Second, a radial CM oscillation is induced by a magnetic field applied for several msec with a current pulse through a small, horizontally-oriented coil. We minimize systematic shifts in the oscillation frequency due to anharmonicities by using pure BECs (our smallest clouds) and small excitation amplitudes ($\approx 1/10R$) After the field ramp and horizontal push initiate the CM motion, the atom cloud freely oscillates in the trap for a variable delay time. Immediately following the delay we image the atoms. By repeating the cycle of cloud creation and CM excita-

tion, for varying free oscillation times, we generate a plot of the CM position versus time that is fit to a single-frequency sine wave. The fit frequency is the oscillation frequency of the trap in the direction of CM oscillation.

Typical CM oscillation data is shown in Figure 6.4 for the axial (6.4a) and radial (6.4b) oscillations. Each pair of axial and radial center positions at each time correspond to a single measurement cycle. The data for both directions are well fit by a single frequency sine wave. The frequencies are $f_z = 12.1 \pm 0.1$ and $f_x = 13.0 \pm 0.1$ Hz. The error bars are limited by the statistical uncertainty of the fitting [181]. Finally, we point-out that for the trap parameters chosen ($B_0 = 540$ mG, $B'_z = 34$ G/cm) we observe a dramatic change in the trap aspect ratio from the $\sqrt{8}$ value predicted for the TOP trap in the absence of gravity.

We examine the theory of TOP operation, in the limit of small axial quadrupole gradients, by fixing the magnitude of the rotating bias field to $B_0 = 540$ mG and varying the axial field gradient to change the trap frequency and symmetry. For each field gradient we measure both axial and radial trap frequencies. The data are plotted in Figure 6.5. The error bars on each frequency point are smaller than the points on the graph. At high gradients, the axial frequencies are greater than 200 Hz. The radial frequencies are noticeably smaller at the same large gradients. Decreasing the field gradient causes the axial frequency to decrease much more rapidly than the radial frequency, until at $B'_z = 36$ G/cm the radial frequency (13.0 Hz) is larger than the axial frequency (12.1 Hz). The frequency data are fit to functional forms for the frequency given in Eq. (6.10) for the axial and radial directions, with two fit parameters corresponding to the field gradient and bias field calibrations to the control voltages. The excellent fit to the data verifies the accuracy of the

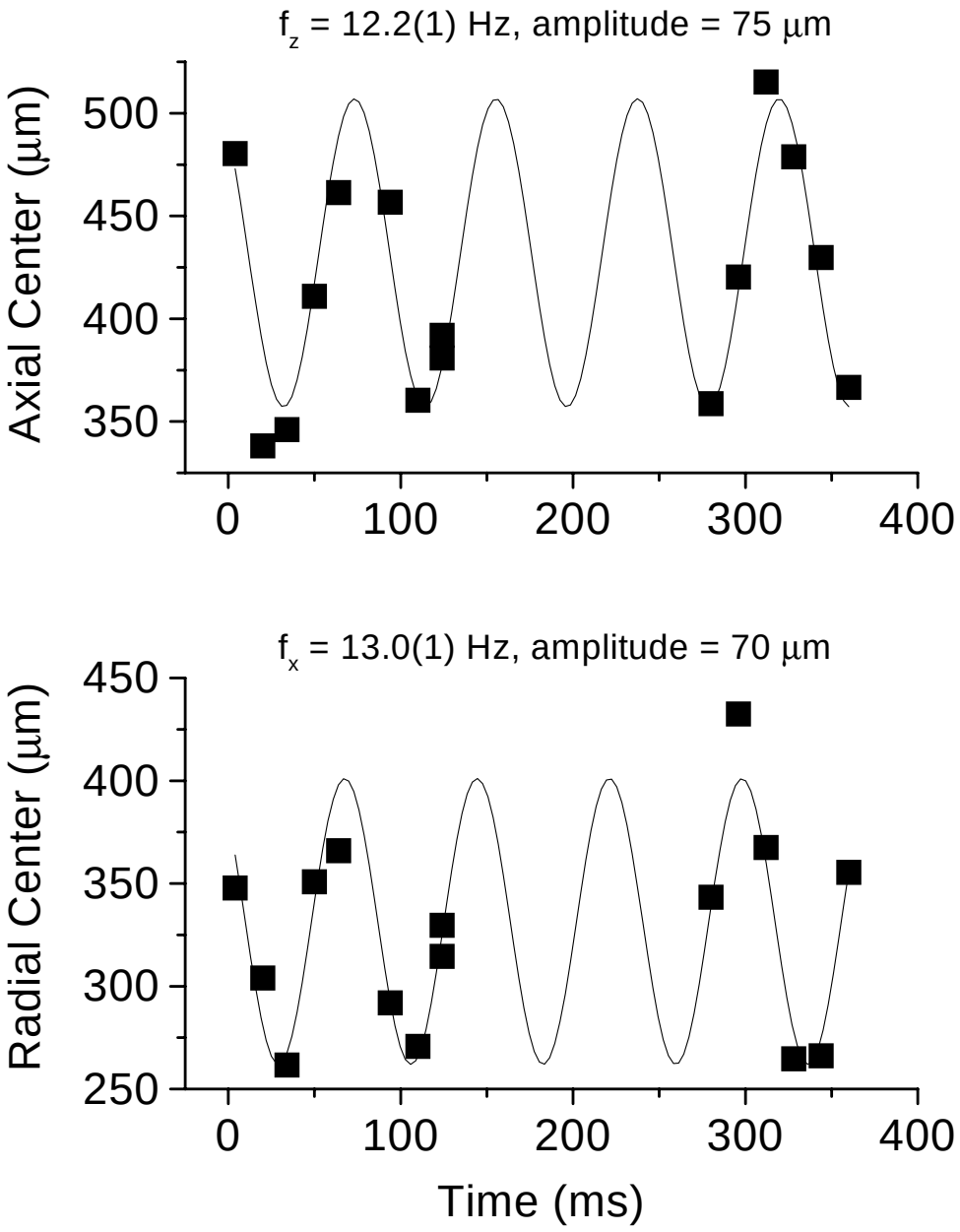


Figure 6.4: Center-of-mass oscillations of atoms in the TOP magnetic trap for $B_{TOP} = 0.54$G and $B'_z = 34$ G/cm.

improved TOP theory. By assuming the functional forms for the frequency are correct, the fits calibrate both field gradient and bias field to a few percent. We can simultaneously and accurately calibrate both trap fields because the trap frequencies vanish rapidly at a specific axial field gradient (30.6 G/cm for the $F = 1$ state). The low-gradient dependence of the trap frequencies therefore strongly constrains the field gradient parameter, while the overall range of trap frequencies dictates the size of the magnetic bias parameter.

We now focus on the change of the trap symmetry with field gradient by plotting the ratio of the axial to radial frequencies versus the axial field gradient in Figure 6.6. At large field gradients, we expect that the ratio approaches the "gravity-free" limit of $\sqrt{8}$ shown by the black horizontal line. As the gradient decreases, the measured frequency ratios decrease from nearly $\sqrt{8}$ (axially symmetric) to below 1 (spherically symmetric). Also plotted on the graph is Eq. (6.11) representing the expected dependence of the frequency ratio on the gradient. Using the gradient calibration from the fit to the data in Figure 6.5, Eq. (6.11) is in very good agreement with the data. The lowest frequency ratio $\omega_z/\omega_x = 4.5/9.4 = 0.48$ demonstrates that we can tune near and around the interesting case of spherical trap symmetry. By further reducing the TOP bias field we can increase the spherical trap frequencies, reaching up to 27 Hz for a bias field of 250 mG.

## 6.5 The TOP trap at Low Magnetic Bias fields

In our next experiments we study the behavior of the TOP trap at low magnetic bias fields. We cite two principle motivations for why operation at low bias fields is interesting for both IP and TOP magnetic traps. First, small

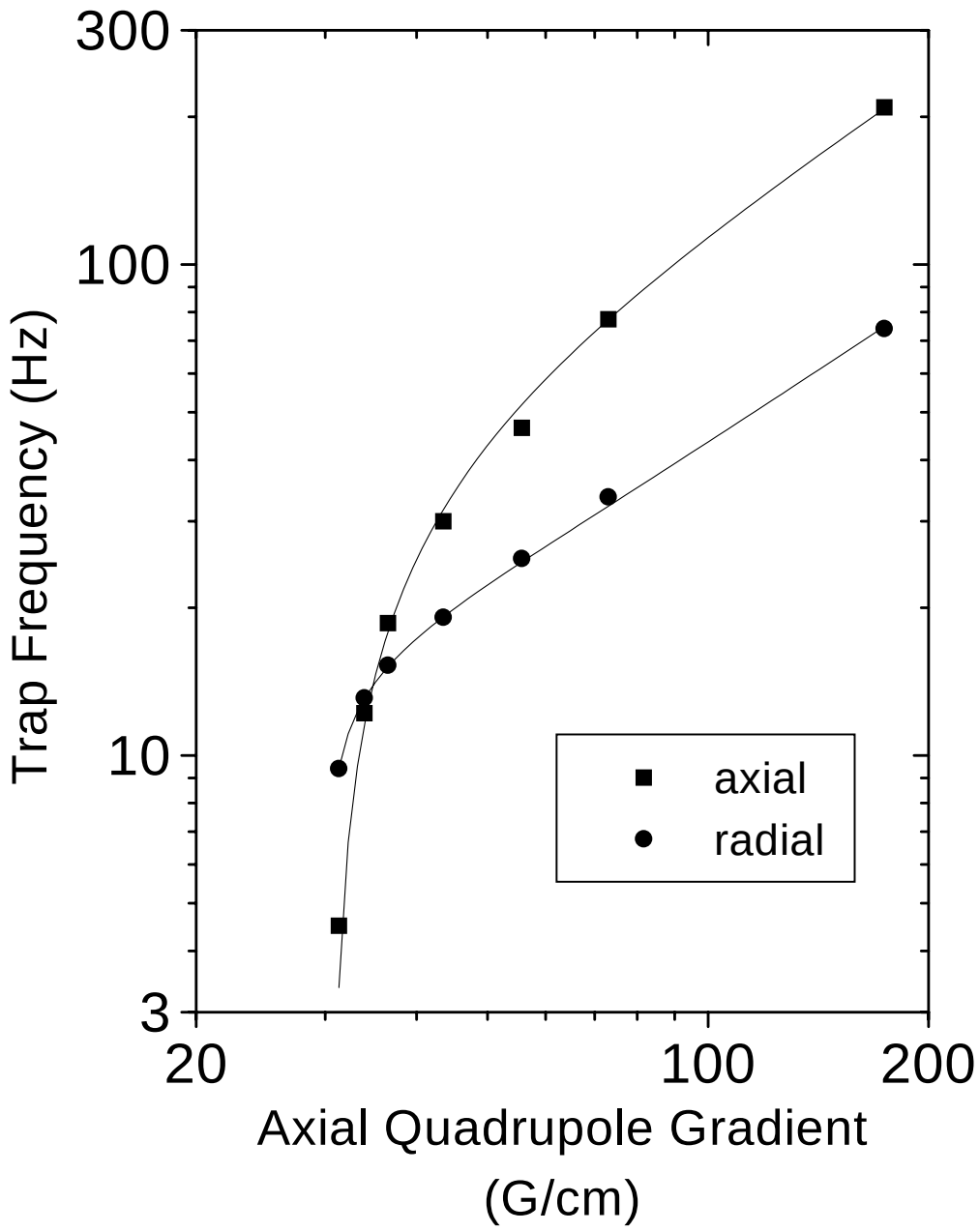


Figure 6.5: TOP Trap frequencies in the axial and radial directions as a function of axial quadrupole gradient. The rotating bias field is 0.54 Gauss for all the data.

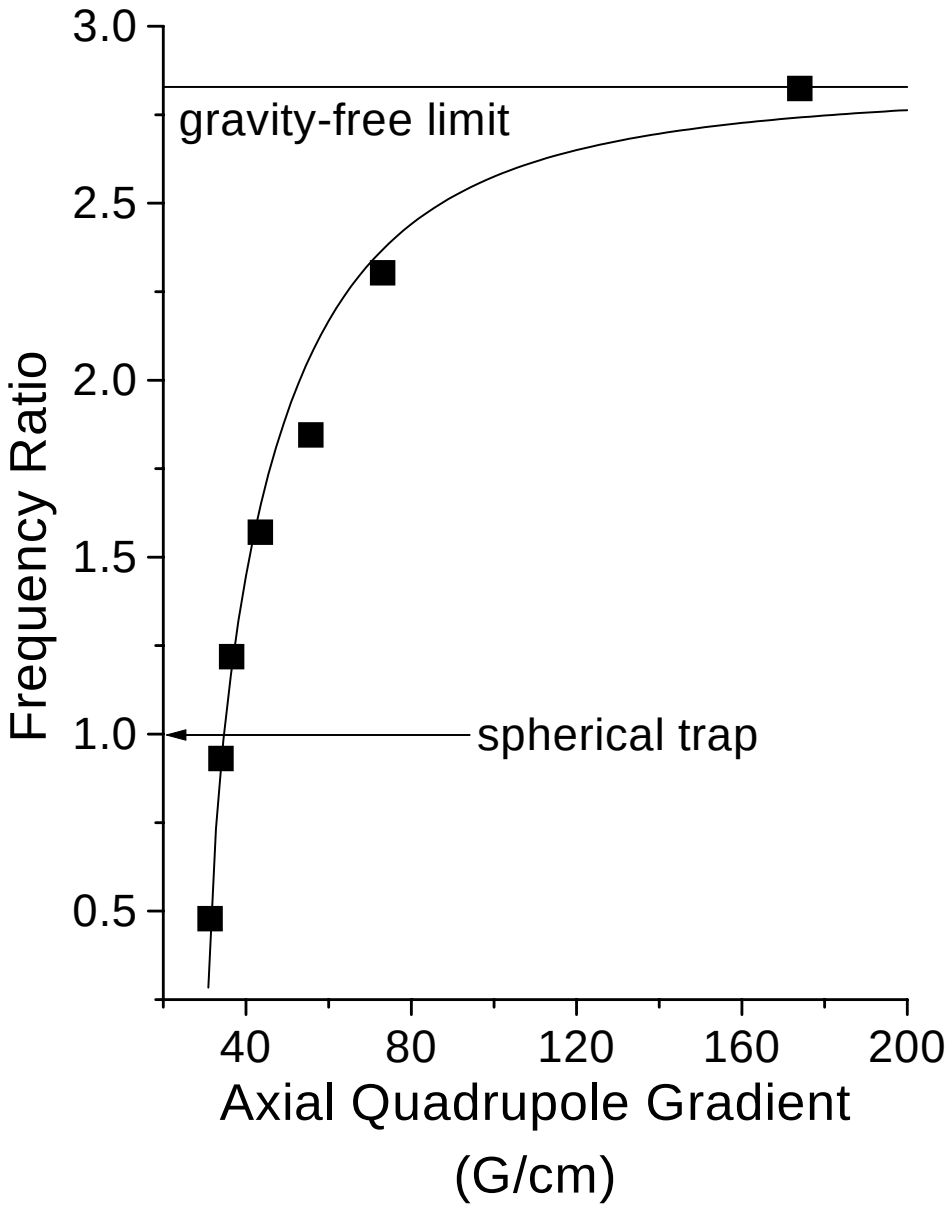


Figure 6.6: Ratio of the axial to radial trap frequencies, shown in Figure 6.5, as a function of axial quadrupole gradient. The solid, horizontal line at $\sqrt{8}$ is the frequency ratio in the absence of gravitational sag. The curved line is the analytical form for the TOP symmetry, Eq. 6.11

bias fields are necessary for high confinement magnetic traps since the trap oscillation frequency $\omega$ scales as $B'_z/\sqrt{B_0}$. This point is especially true in the case of near-spherical symmetry magnetic traps: the field gradient must be lowered to change the trap symmetry, which also implies lower trap frequencies. Therefore, small bias fields are needed for high-confinement spherical traps. For experiments in which number of atoms is not easily increased, increasing the trap confinement is a convenient way to achieve high sample densities. For atoms trapped in a harmonic potential the density of the sample scales in the following ways. In noncondensed clouds, adiabatically increasing the trap spring constants will compress the sample to a density that is proportional to the $\omega^{3/2}$. In Bose condensates with repulsive mean-field interactions, the density scales as $\omega^{6/5}$. A second, compelling motivation for studying magnetic traps at low bias fields is that the rate of dipolar relaxation losses from the lower hyperfine state of a trapped alkali atom should be suppressed at zero magnetic field [182]. Dipolar relaxation is the dominant loss mechanism limiting evaporative cooling of $^{133}$Cs [183]. Recent results also show a suppression of the dipolar rate at low fields and indicate that bias fields as small as 100 mG may be necessary to achieve BEC in Cs [178].

Low magnetic bias operation – at or below 1-2 Gauss – has always presented a problem for magnetic traps. Presently, most traps seem to suffer from very high loss rates at these fields. In IP traps, achieving small yet stable bias fields of $1-2$ Gauss is technically challenging because the near-cancellation of two large bias fields is required. This well-known challenge in IP traps led to some of the only studies of trap lifetime in low magnetic fields [122, 152, 161]. The precise loss mechanisms for low fields have not been identified. To our knowledge, the low-field regime of operation has also never been explored in

a TOP trap. This regime is technically easy to reach in a TOP, since we reduce only a single bias field. In this section we describe measurements of the lifetime of $^{87}$Rb atoms in the TOP magnetic trap to better understand the loss mechanisms in the important low magnetic field regime.

We can focus on the losses in the regime of low magnetic fields because many of the other loss mechanisms are well-characterized. One ubiquitous mechanism is loss due to collisions of high energy background gas with the magnetically trapped sample. The loss rate from background collisions is independent of the sample density, leading to a purely exponential loss of atoms from the trap. Low background pressures of $10^{-11} - 10^{-12}$ Torr, typical of magnetic trapping experiments, can yield lifetimes of 100's to 1000's of seconds. Inelastic collisions between trapped atoms are another source of trap loss. Unlike $^{133}$Cs, for which dipolar relaxation is the dominant inelastic process, for $^{87}$Rb inelastic loss is dominated by three-body recombination [184]. The per atom loss rate scales as the density squared and hence becomes the primary limit to the lifetimes of large $^{87}$Rb condensates. For example, in a condensate of peak density $4 \times 10^{14}$ cm$^{-3}$ the three-body rate for condensates of $6 \times 10^{-30}$cm$^6$/sec [184] implies a lifetime on the order of a few seconds. Another feature of inelastic loss is a highly non-exponential decay of atoms from the trap. During the following lifetime studies, we minimize changes in density so that we do not confuse losses due to changing the bias field with losses due to a changes in the three-body loss rate.

Several other loss mechanisms, intrinsic to magnetic traps and the TOP trap, are worth mentioning. If atoms move too quickly through a region of low magnetic field their atomic magnetic moments are unable to adiabatically follow the field and a Majorana transition to another spin state occurs [160].

The change of spin alignment and/or the gain of kinetic energy leads to trap loss. Majorana transitions occur when the rate of change of the magnetic field seen by the atom is comparable to the Larmor splitting between magnetic spin states: $\vec{v} \cdot \vec{\nabla}\left(\frac{\vec{B}}{B}\right) \approx \frac{\mu B}{\hbar}$. For the temperatures and field gradients of our experiments, this condition is met for magnetic fields of only a few mG and are much smaller than the fields we study.

Another concern relating to trap loss is that the TOP trap has a finite energy depth $E_{\rm d}$, defined by the radius $R$ at which the quadrupole zero orbits the atoms. The trap depth $E_{\rm d} = k_{\rm B}T_d = \mu B/4$ decreases as the bias field decreases. Atoms with energy greater than or equal to the trap depth encounter the quadrupole zero, undergo a spin-flip and are lost from the trap at a rate on the order of the radial oscillation frequency. The fraction of a cloud of atoms that is lost in this way is determined by the fraction of atoms with an energy larger than the trap depth. For example, in a non-condensed gas 65% of the sample is lost in a few radial oscillation periods if the trap depth is equal to the mean energy of the cloud ($3k_{\rm B}T$). If the trap depth is twice the cloud's mean energy then only about 11% are lost in a similar time. Twice the mean energy, $6k_{\rm B}T$, therefore is a useful, approximate definition of the maximum energy of atoms confined in the TOP trap. Equating $6k_{\rm B}T$ to the trap depth $E_{\rm d}$, we estimate the maximum temperature of an atom cloud in the TOP trap. At a bias field of 1 Gauss, the trap depth for $F = 1$ ($\mu = 1/2\mu_{\rm B}$) atoms is 8.3 $\mu$K and implies a maximum temperature for the trapped atoms of $< 1.4$ $\mu$K.

A final concern are trap losses from magnetic field noise, coming from an ambient source, a frequency component of the magnetic field current, or both sources. Noise power at frequencies twice the trap frequencies (10-100's of Hz) can parametrically drive the sample and eventually heat atoms out of

the trap [185]. At higher frequencies, noise power at hundreds of kHz can directly drive spin-flip transitions.

In our first experiments we measured loss of atoms from noncondensed clouds (Figure 6.7). Generally, we observe atom loss that is well-fit by an exponential decay in the number of atoms. We therefore ascribe a $1/e$ lifetime to the atom loss, that is the inverse of the exponential decay rate derived from a fit to the data. Starting in the trap with 6.2 Gauss bias field we observe a lifetime of 348 sec, consistent with losses due to collisions with background gas. The lifetime decreases linearly with decreasing bias field in the trap, reaching 94 sec at 1.1 Gauss. Below 1 Gauss, the lifetime drops more quickly with the field and reaches 0.5 sec at 190 mG. Although the cloud density increases slightly as the bias field decreases, the loss rates are too fast to be explained by three-body recombination. We also examined the trap depth as a loss mechanism. A plot of the ratio of trap depth $E_{\rm d} = k_{\rm B}T_d$ to the initial mean energy $3k_{\rm B}T$ as a function of trap bias (Figure 6.8, solid squares) shows that the TOP is shallower with respect to the mean particle energy at low bias fields. We also find heating of the atoms while they reside in the trap, further narrowing the difference between trap depth and mean energy. The heating rate is initially $5 - 10$ nK/sec and vanishes as the cloud reaches a steady-state temperature. The time-scale for reaching the steady-state on the order of the $1/e$ lifetime. Heating from a shallow trap might explain the very short lifetimes in the 190, 350 and 650 mG traps, where heating leaves the trap depth only 1.3, 2.9 and 3.3 times larger than the mean energy of atoms, for long dwell-times in the trap (Figure 6.8, hollow circles). However, this mechanism seems unlikely to be the loss mechanism for all the data. Above 1 Gauss, where the trap depth is larger than four times the mean energy (after heating), a loss mechanism due

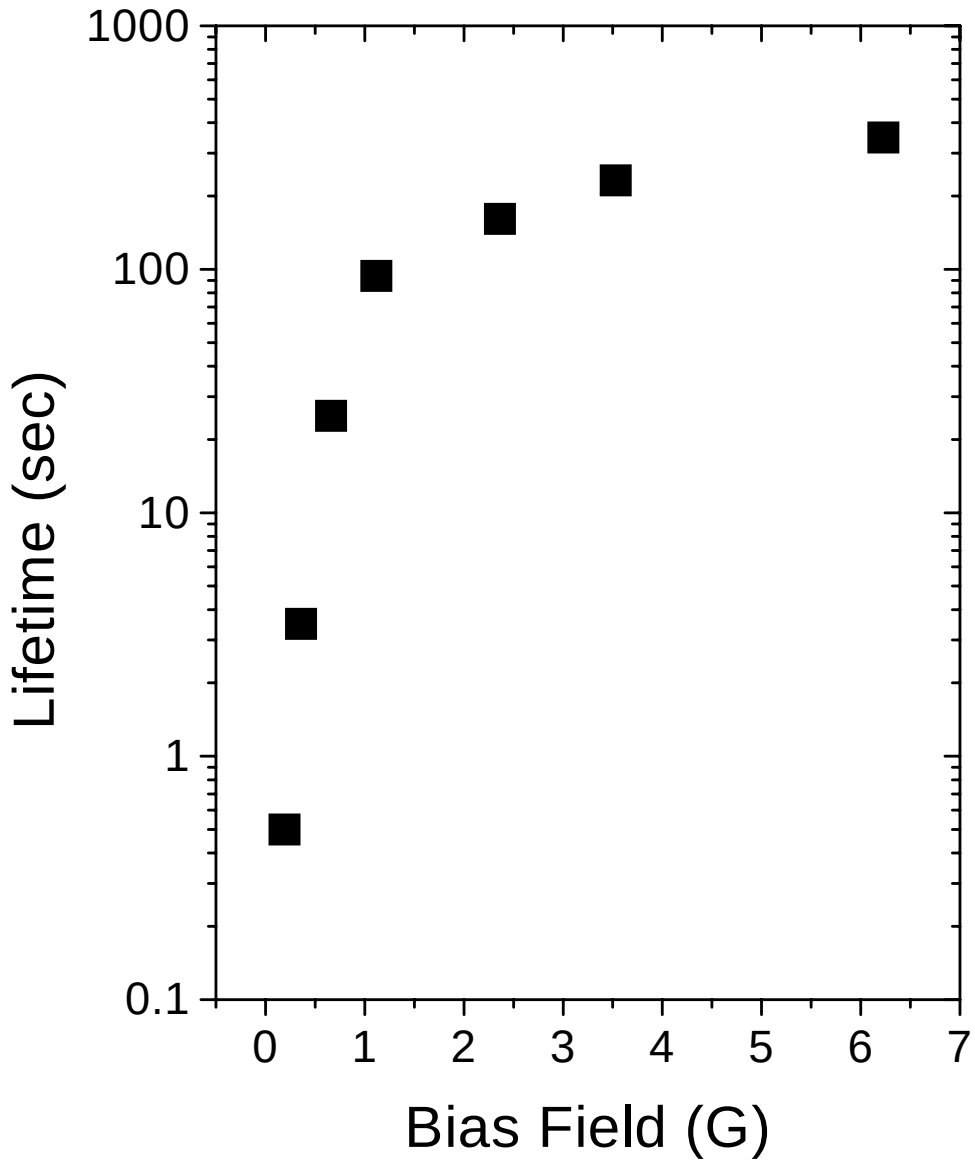


Figure 6.7: Lifetime for noncondensed clouds in a TOP trap at various bias fields. The lifetime is the $1/e$ time of an exponential fit to the atom number versus time data.

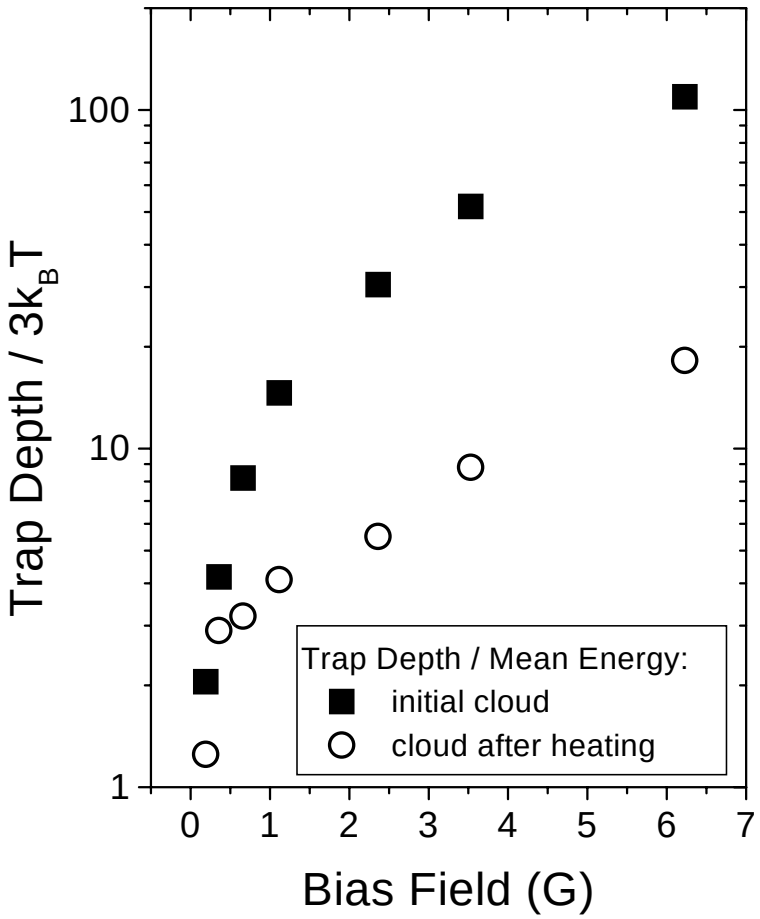


Figure 6.8: Ratio of trap depth to mean cloud energy for noncondensed clouds in a TOP trap at the same bias fields used to study lifetimes (see Fig. 6.7). The squares and hollow circles show the ratio of trap depth to mean cloud energy, $E_{\rm d}/3k_{\rm B}T$, for clouds initially in the trap and after a steady-state temperature is reached due to heating, respectively. $E_{\rm d}$ is defined in the text.

to heating should exhibit a very non-exponential loss profile. In these cases, in which mean energy is much less than the trap depth, a finite time is required to heat the atoms before their mean energy is comparable to the trap depth, at which point the loss is subsequently exponential. We neither observe this delay nor non-exponential character to our atom loss profiles.

At this point we exploit some features of the Bose condensate to better understand the loss physics. The maximum extent of a large ($10^6$ atom), pure condensate is $2-3$ times smaller than the full-width half maximum of non-condensed (Gaussian profile) clouds just above the BEC transition. The condensate density profile for our experiments is well-approximated by an inverted paraboloid which has a sharp spatial cut-off in the density profile, defined by the half-width at zero maximum (hwom) of the distribution. Therefore, the probability of a condensate atom encountering the zero of the quadrupole field, and hence being lost from the trap, is negligible if $R < X_{hwom}$. We created condensates with temperatures $T < 0.4T_c$ and measured their lifetime in the trap. Our first measurements of the condensate lifetimes, for bias fields larger than 1 Gauss, displayed a surprising linear decay of number with time. For these samples the condensate decays into a broad non-condensed cloud, which also decays in time. The decay of a condensate in a TOP trap of bias field 6.2 Gauss is shown in Fig. 6.9 (solid squares). The cloud has an initial central density of $7.3 \times 10^{13}$ atoms/cm$^3$, from which we predict an initial three-body limited lifetime of 86 sec. The observed $1/e$ time of the linear decay is only 12 sec. Our previous experience with similar loss behavior [152] suggested that atoms heated out of the condensate nonetheless remain trapped, albeit at higher energy, and enhance the loss rate by continuing to collide with the remaining condensate atoms. We quench the loss-inducing collisions by ap-

plying a weak rf magnetic field tuned to an energy lying at or just inside the orbit of the rotating zero-field. This so-called "rf shield" induces spin-flip of hot atoms before they return to knock atoms from the condensate. The shield lies at high enough energy that the initial condensate number is unaffected, but the effect on the loss of atoms is dramatic. The decay profile becomes well-fit by an exponential curve with a much longer $1/e$ lifetime than without the rf shield. At 6.2 Gauss the lifetime, as extracted by an exponential fit to the data (dashed line in Fig. 6.9), jumps to 67 sec, consistent with losses due to background collisions ($\approx 400$ sec) and 3-body recombination [186].

We measured lifetimes of pure condensates over the same range of bias fields we studied with noncondensed clouds and applying an rf shield. The data are shown in Figure 6.10. The lifetimes are determined by fitting exponential decay curves to the data. The condensate lifetime decreases as the bias field decreases. For bias fields larger than 1 Gauss, the data are reasonably fit by a linear function of the bias field that is constrained to intercept the origin (we expect no atoms to remain in the TOP at zero magnetic field). For bias fields less than 1 Gauss, the lifetimes are consistently shorter than the linear fit. We note that, even with the rf shield, only the data at 6.2 and 3.5 Gauss are quantitatively consistent with a three-body recombination. As the bias field is decreased, the effect of the rf shield also diminishes, until below 1 Gauss it provides no enhancement to the condensate lifetime. Nonetheless, the loss of atoms remains exponential for bias fields below 1 Gauss. Also qualitatively speaking, three-body recombination alone cannot explain the observed loss. Over the range of bias fields studied, the density increases a factor of two (Fig. 6.11, empty circles), implying a factor of four change in the loss rate due to recombination. The observed change in lifetime is a factor of 180.

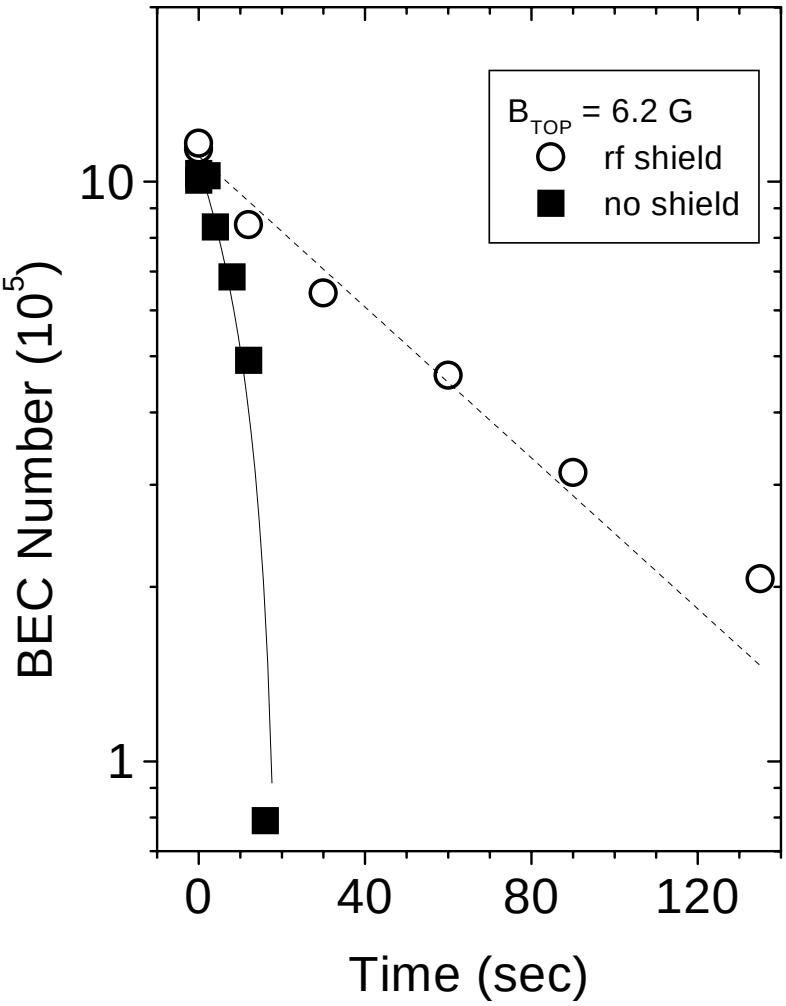


Figure 6.9: Decay of a Bose condensate in a TOP trap with bias field of 6.2 Gauss. Condensate decay was first measured without an rf shield (solid squares). The data are fit to a decay curve in which the number of atoms decreases linearly in time (solid curve). The $1/e$ decay time, obtained from the linear fit, is 12 sec. Next, condensate decay was measured using an rf shield (empty circles). The loss rate decreases dramatically and the data are well-fit by an exponential decay curve. From the fit to the shielded data we extract a $1/e$ lifetime of 67 sec.

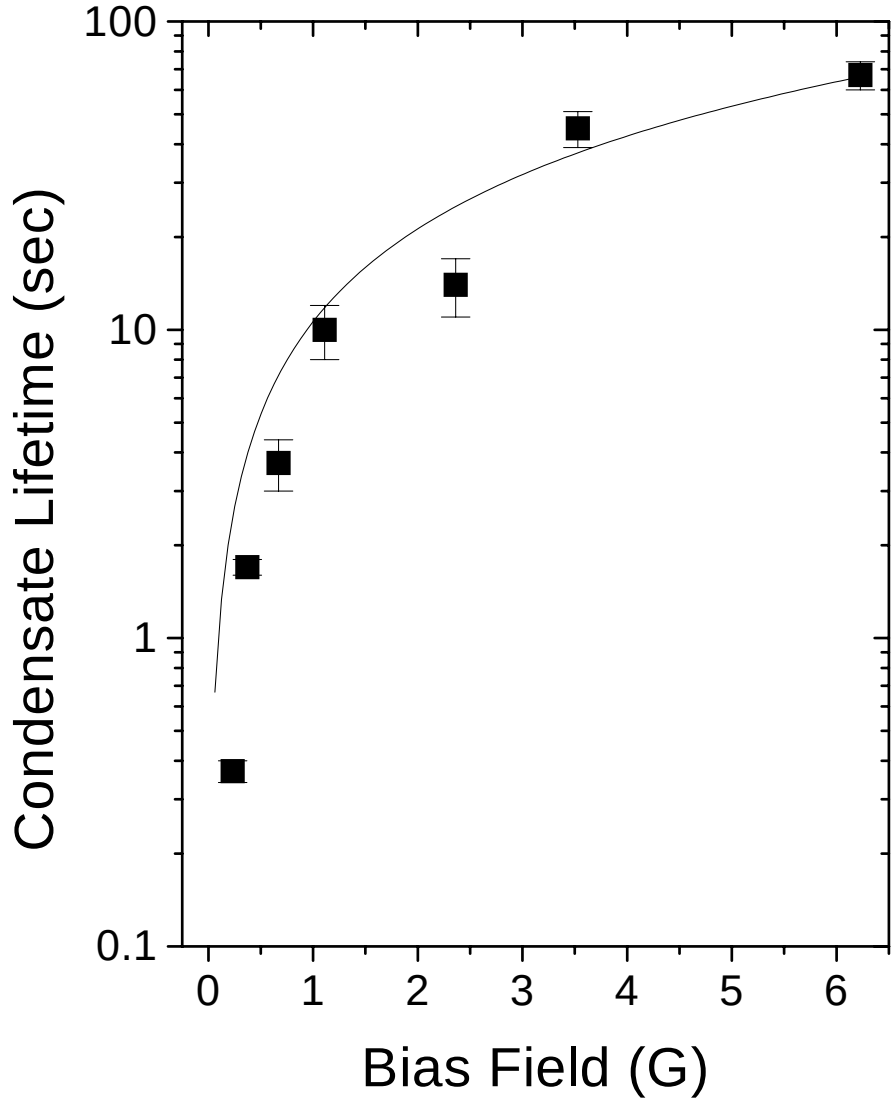


Figure 6.10: Lifetimes of Bose condensates in a TOP trap for various bias fields. The error bars are purely statistical, based on exponential fits to the observed number vs. time decays. The data are fit to a linear function of the bias field in which the lifetime is constrained to vanish when $B = 0$, as anticipated for the TOP.

Two additional observations argue against a general density-dependent loss that depends on magnetic field. First, at the same value of central density we measure two very different lifetimes (see Fig. 6.11). For example, at $9 \times 10^{13}$ atoms/cm$^3$ (and at $15 \times 10^{13}$ atoms/cm$^3$) we measure two lifetimes that differ by a factor of 3.2 (4.6). Second, as the bias field decreases, both condensate and non-condensate lifetimes converge to the same values ($0.4 - 0.5$ sec at 0.2 Gauss, see Figs. 6.7 and 6.10 ) even though the condensate central density is an order of magnitude larger than the non-condensate. We also dismiss trap depth as the mechanism for the decreasing condensate lifetimes. As seen in Fig. 6.11 (solid squares) the radius of the orbit of the quadrupole zero is never closer than 4.5 times the radial hwom (at the lowest bias field of 220 mG) and is usually much larger.

Another candidate to explain the trap loss is magnetic field noise. The first possible mechanism is that noise features near twice the trap frequencies parametrically heat atoms out of the trap. We find no correlation between reduced trap lifetime and coincidences of twice our trap frequencies with the closest noise features at 60 and 120 Hz. The axial trap frequency is 32 Hz at 6.2 Gauss and increases with decreasing field to 45 Hz at 0.23 Gauss. We note that the longest lifetime (67 sec) is observed for the axial frequency nearest the 60 Hz feature. In the radial direction, trap frequencies start at 13 Hz (6.2 G) and also increase with decreasing field up to 33 Hz (0.23 G). The low field lifetimes are near the 60 Hz noise, but the decrease in lifetimes begins for radial frequencies much smaller than 60 Hz and well outside its spectral bandwidth. Thus, parametric driving of atoms out of the trap appears unlikely.

Magnetic field noise at hundreds of kHz, which drives transitions in trapped atoms into untrapped spin states, is a more likely candidate for low-

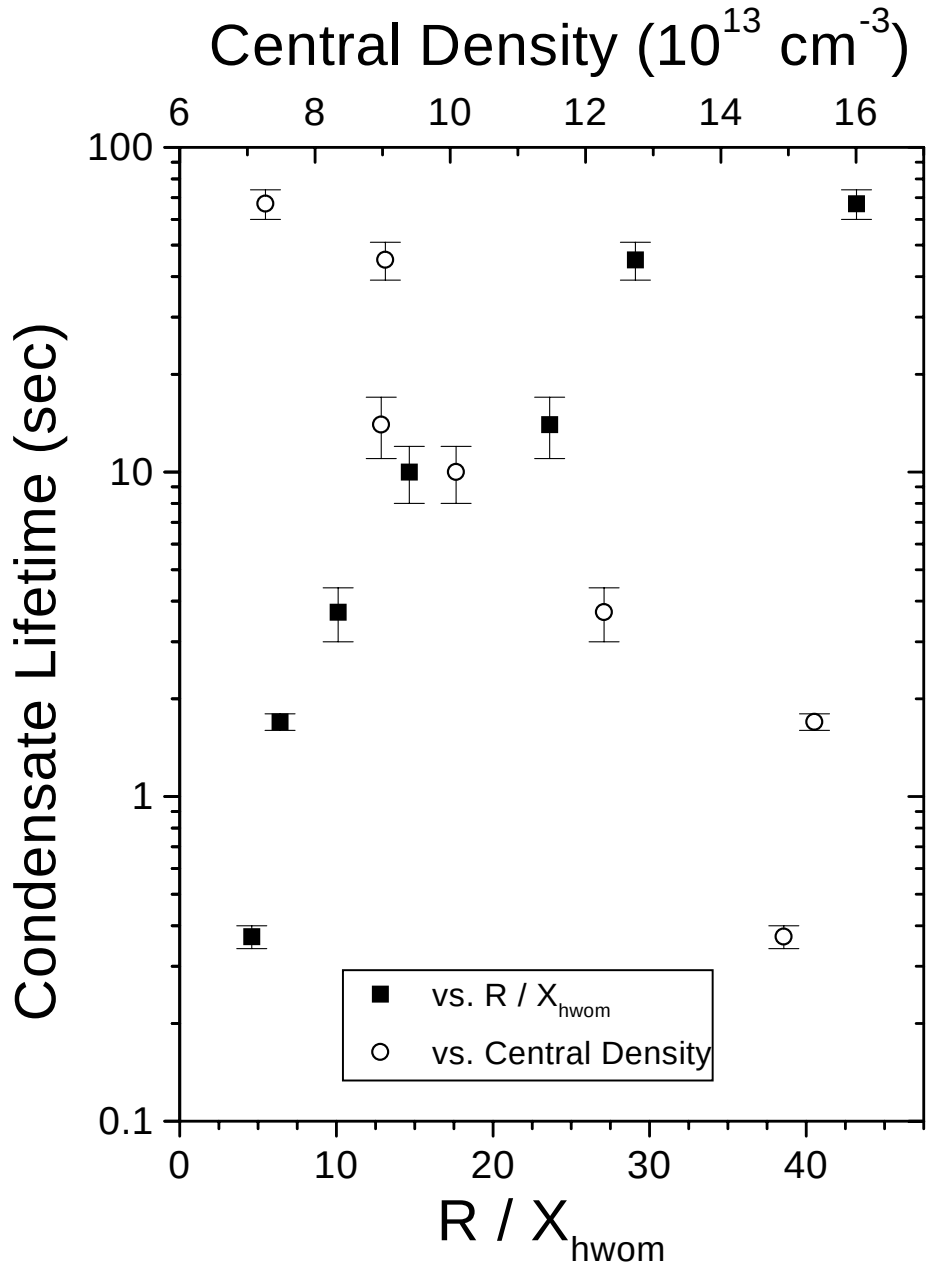


Figure 6.11: Lifetimes of Bose condensates in a TOP trap versus the ratio of quadrupole orbit radius to radial half-width at zero maximum (hwom), $R/X_{\rm hwom}$ (solid squares), and versus central density (hollow circles), for the data in Fig.6.10.

field loss. The danger of losses at these frequencies arises because the Larmor frequency splitting between Zeeman levels is 700 kHz at 1 Gauss, and reduces linearly with the bias field. We measure the magnetic field power spectrum by directly monitoring, on a spectrum analyzer, the voltage induced in a pick-up coil. The coil is placed near the trap region and oriented perpendicular to the axis of the quadrupole coils. When only the quadrupole coils are on, we noticed that the magnetic field noise spectrum exhibits a comb of noise spikes spaced by $\approx$ 20 kHz, beginning at 20 kHz and rolling-off in amplitude above 1 MHz. These features originate from the switching power supply for the quadrupole coils. However, noise on the quadrupole current should be greatly suppressed in the field at the center of the anti-Helmholtz coil pair because the quadrupole coils are connected in series and so current noise cancels. Indeed, reducing the noise spikes by $10 - 20$ dB, using a less noisy power supply, did not improve the lifetimes or the trend of reduced lifetime with reduced bias field. Only by generating an artificial noise comb of the same frequencies with substantially more power could we cause a reduction of trap lifetime.

Next we turned to the field noise associated with the TOP field. We measure the power spectrum of the magnetic field near the cell when the TOP coils are on, the quadrupole coils off, and without any rotating bias field. Using the same technique as above, we measure broad-band spectral noise that we estimate is 0.7 $\mu$G/$\sqrt{Hz}$ at 100 kHz, rolling-off roughly as 1/frequency$^3$ and hitting the noise floor of the spectrum analyzer at 800 kHz (see Fig. 6.12) [187]. Herein lies another possible loss mechanism: As the bias field of the trap is reduced, the Larmor frequency is tuned into resonance with the broad-band noise field. We estimate the loss rate of atoms from the cloud with the following model. We first calculate the rate at which a broad-band magnetic

field drives an atom from the trapped $F = 1, m_F = -1$ state into the untrapped $F = 1, m_F = 0$ state of $^{87}$Rb using time-independent perturbation theory. The rate $\gamma$ may be expressed in terms of the power spectral density of the magnetic field and is written as:

$$\gamma = \frac{\pi}{4}\left(\frac{\mu}{\hbar}\right)^2 S(\omega) \tag{6.17}$$

where $\mu$ is the magnetic moment of the initial state, $S(\omega)$ is the one-sided power spectrum given by

$$S(\omega) = \frac{2}{\pi}\int_0^\infty \cos(\omega\tau)\langle B(t)B(t+\tau)\rangle \, \mathrm{d}\tau.$$

and the correlation function of the magnetic field fluctuations is [188]

$$\langle B(t)B(t+\tau)\rangle \equiv \frac{1}{T}\int_0^T B(T)B(T+\tau)\, \mathrm{d}t$$

The loss rate for the entire sample is found by integrating the per atom loss rate over the condensate density profile. The span of frequencies covered by the condensate is so small that to an excellent approximation the power spectrum is constant across the cloud. The rate equation is therefore:

$$\frac{\mathrm{d}N}{\mathrm{d}t} = -\frac{\pi}{4}\left(\frac{\mu}{\hbar}\right)^2 S(\omega)N \tag{6.18}$$

The frequency $\omega$ is determined by the splitting between Zeeman levels of the $F = 1$ manifold, which is set by the magnetic bias field of the trap [189]. The

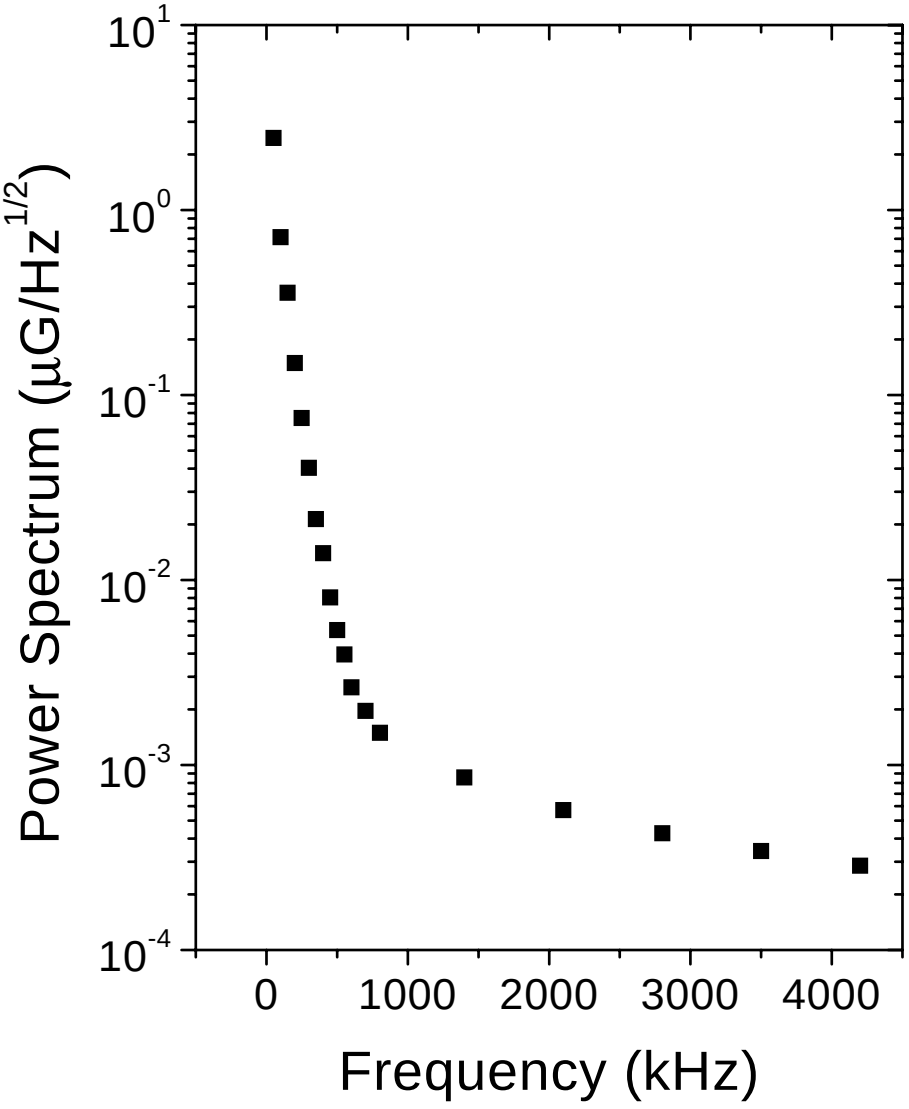


Figure 6.12: Measurement of the field noise from the TOP coils at the location of the trapped atoms. The field noise, in $\mu\mathrm{G}/\sqrt{Hz}$, rolls-off roughly as $1/\mathrm{frequency}^3$ until it reaches the noise floor of the rf spectrum analyzer at 800 kHz. Above 800 kHz, the plotted noise spectrum is an upper-estimate to the actual field noise.

rate equation describes a purely exponential loss whose rate is proportional to the power spectral density $S(\omega)$ of the magnetic field noise. In our data we also observe exponential decays, as well as increased losses for level-splitting frequencies where the power spectral density is measured to increase. We make a quantitative comparison to our data by modeling the overall loss rate as the sum in parallel of the initial three-body recombination rate, a background collision rate (0.0029 $\sec^{-1}$) and the noise-induced loss rate [190]. The results of the model are compared to the measured lifetimes in Figure 6.13. The model (solid line) closely resembles the lifetime data at very low bias fields, but underestimates the loss rate for much of our data. At low fields this is due to the rapid roll-off in the spectral noise density $S(\omega)$, which greatly reduces the noise-induced loss rate (dashed-dotted line) above 0.2 Gauss. By about 0.4 Gauss, three-body recombination is the predominant loss mechanism, in the model. The model agrees well with the measured lifetimes above 3 Gauss. Given the difficulty of measuring absolute field noise at the atoms a quantitative disagreement is not surprising. Unfortunately, even assuming twice the measured field noise, an increased noise-induced rate (dotted line) does not significantly improve the agreement of the theory to most of the data. The results of the model do suggest that broad-band noise-induced losses may be a significant loss mechanism at very low magnetic fields. A detailed understanding of the observed trap loss for all magnetic fields requires further study.

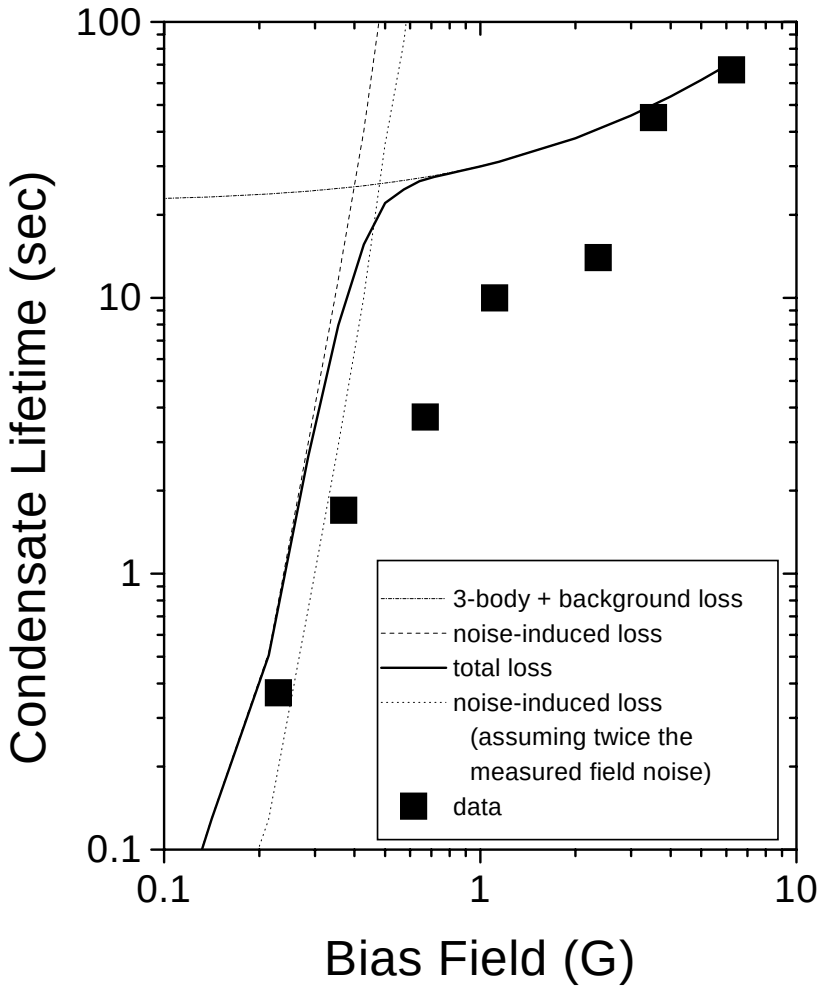


Figure 6.13: Comparison of measured lifetimes of Bose condensates in a TOP trap to a model (solid line) of noise-induced (dashed line) and three-body plus background collision (short dashed-dotted line) losses as a function of the net bias field. Small-scale roughness in the curves is an artifact of the sparse number of calculated points. The model, explained in the text, uses the measured power spectral density of the magnetic field noise to predict the rate of spin-flip transitions in the trapped cloud. Also shown is the predicted noise-induced lifetime if the field noise were twice the measured value (dotted-line).

## 6.6 Effects of Bias Field Rotation Frequency

As was mentioned at the end of Section 6.2.1, the original TOP trap easily satisfied the limiting conditions 6.1, and long trap lifetimes were observed [21]. To our knowledge, no one has ever performed experiments to determine at which rotation frequencies $\omega_{\rm T}$, relative to trap oscillation frequencies and Larmor frequency, the TOP trap no longer holds atoms. In this section we study the lifetime of atoms in the TOP trap as a function of $\omega_{\rm T}$ to experimentally quantify the breakdown of the time-averaging and adiabaticity conditions 6.1 in the TOP trap. Breaching the adiabaticity condition 6.1b is especially interesting as it may play a role in increasing loss in the TOP at small bias fields. In our study of lifetime versus magnetic field, $\omega_{\rm T}$ was held fixed while the bias field, and hence the Larmor frequency, was reduced.

The experimental method is much the same as for studying the lifetime in the TOP at different bias fields. We begin each experimental cycle in a TOP trap of 1.8 kHz bias rotation frequency. After evaporatively cooling the cloud until only a pure condensate remains we then adiabatically ramp the trap fields to the desired bias field and trap frequencies. We then change the TOP rotation frequency in $\lesssim 0.5$ ms, simultaneously adjusting the relative gain and phase of the TOP channels. The gain and phase shift adjustments compensate for the frequency-dependent gain and phase shifts of the TOP circuit and preserve the eccentricity and bias field for TOP frequencies other than 1.8 kHz. Technical limitations unfortunately prevent us from making the rotation frequency either less than the trap frequencies or greater than the Larmor frequency [191]. The atoms remain in the TOP trap for a variable dwell time, after which the TOP rotation frequency is returned to 1.8 kHz with the ap-

propriate channel gains and phases. Once returned to the 1.8 kHz trap, the atoms are probed with absorption imaging to count the remaining atoms. This method of *in situ* frequency adjustment allows us to create and probe clouds in a standard TOP trap whose critical timing is always the same, regardless of the rotation frequency we wish to study.

In a first experiment, we study the lifetimes of condensates of $\approx 7.5\times10^8$ atoms in a trap with frequencies $f_x = 36$ Hz and $f_z = 87$ Hz (Fig.6.14, solid squares). The bias field is 0.59 Gauss (413 kHz Larmor frequency). At 1.8 kHz the lifetime is 1.9 sec, consistent with previously measured low-field lifetimes. Over the decade of TOP frequencies up to 18 kHz the lifetime decreases only 15%, but at 27 kHz plummets to 0.2 sec. Decreasing the TOP rotation frequency from 1.8 kHz, the lifetime steadily decreases to 0.4 sec at 0.2 kHz.

In our second experiment we attempt to improve the sensitivity of the lifetimes to losses at extreme TOP frequencies by reducing the three-body recombination limit to the lifetime. We decrease the initial condensate density both by using only $\approx 1\times10^4$ atoms and lowering the trap frequencies to $f_x = 23$ Hz and $f_z = 43$ Hz [192]. The bias field is 0.65 Gauss (455 kHz Larmor frequency). The data are shown in Figure 6.14 (solid circles). The lifetime at 1.8 kHz is improved to 9 sec and remains approximately constant with frequency, up to 27 kHz. Decreasing the TOP frequency from 1.8 to 0.35 kHz decreases the lifetime by a factor of 2, in qualitative agreement with the 0.59 Gauss data.

For our final experiment we focused on losses at high TOP frequencies by reducing the Larmor frequency (Figure 6.14, empty triangles). We use an intermediate number of atoms ($\approx 2\times10^5$) and low trap frequencies ($f_x = 23$ Hz

and $f_z = 48$ Hz) to reduce three-body collisions. Working in a trap with bias field of 0.36 Gauss the Larmor frequency, 250 kHz, is just 9.3 times larger than the 27 kHz maximum TOP frequency. Increasing the TOP frequency from 1.8 to 27 kHz decreased the TOP lifetime by almost a factor of five.

Interpreting these data is difficult for several reasons. Let us begin with an examination of the data at high rotation frequencies. We point out that in a trap with 0.59 Gauss bias field the lifetime at 27 kHz rotation frequency is a factor of 10 smaller than at 18 kHz. In contrast, even though the Larmor frequency is virtually identical, lifetimes taken in the 0.65 Gauss trap for 27 and 18 kHz rotation frequencies are the same, within the experimental error bars. Such inconsistency may be due, in large measure, to the technical difficult of consistently creating a TOP trap with 27 kHz rotation frequency. We experience even greater problems in the data at low frequencies: in addition to the challenge of making a 200 Hz rotation frequency in our TOP circuit, the short lifetime measured at 200 Hz could be interpreted as the result of noise at 60 Hz or its harmonics. The data at 0.65 Gauss, excluding the 27 kHz data point, cover a wide range of rotation frequencies that are also far from the ambiguous regions of operation mentioned above. The best conclusion we are able to draw from these data is that if $\omega_{\mathrm{T}}$ is at least 25 times smaller than the Larmor frequency and at least 8 times larger than the axial trap frequency, then the TOP trap lifetime is not decreased due to violations of the basic TOP trap conditions 6.1b and 6.1a. Although the conclusion is less definitive than initially intended, it nonetheless reveals that the reduction in trap lifetimes at low bias fields cannot be due to loss of adiabaticity in the TOP trap. In the bias field data (Fig. 6.10), the Larmor frequency is at least 90 times larger than the TOP rotation frequency.

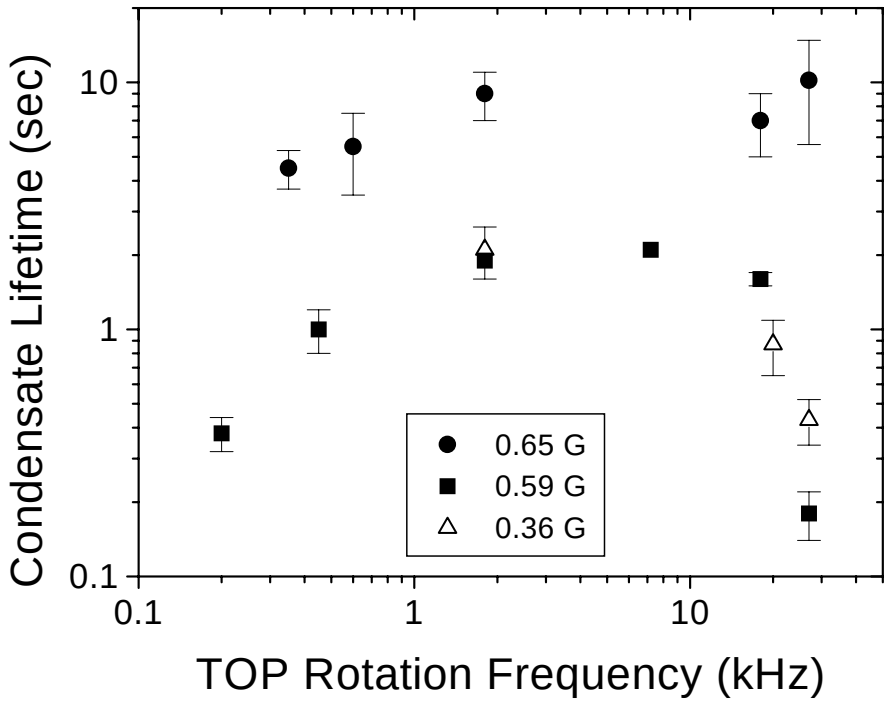


Figure 6.14: Lifetimes of Bose condensates in a TOP trap as a function of the frequency of the rotating bias field, for three different values of the bias field. The solid circles are measured in a trap of 0.65 Gauss bias field, $f_x = 23$ Hz and $f_z = 43$ Hz. The solid squares are measured in a trap with 0.59 Gauss bias field, $f_x = 36$ Hz and $f_z = 87$ Hz. The empty triangles are measured in a trap with 0.36 Gauss bias field, $f_x = 28$ Hz and $f_z = 48$ Hz. The Larmor frequency is 700 kHz/Gauss.

## 6.7 Summary and Conclusions

In this chapter we have explored the properties of the TOP magnetic trap both theoretically and experimentally. We rederived the time-averaged orbiting potential including the effects of gravity and found corrections to the spring constants that depend on the strength of the quadrupole gradient. Tuning the gradient adjusts the trap aspect ratio from $\sqrt{8}$ to less than 1. Simple control over the aspect ratio should permit study of the resonant response of the collective excitations of Bose condensates to trap symmetries [193]. We also precisely calculated the anharmonicity of the TOP and found that, for reasonable experimental conditions, the anharmonic terms introduce less than a 1% fractional shift in the axial and radial frequencies. Low anharmonicities should improve at least two classes of experiment. First, elimination of anharmonic dephasing will allow unambiguous identification of the damping mechanisms in condensate collective excitations [194]. Second, reducing systematic uncertainties in frequency will enable precision measurement of the condensate excitation frequencies beyond the 1% level, offering a first glimpse at many-body physics in the condensate [195].

We have studied TOP trap lifetimes operating the trap under various extreme conditions. We now understand several of the loss mechanisms that plague magnetic traps operating with very small bias fields. Above 1 Gauss, we observe a loss process in which atoms are lost from the observable cloud but remain trapped at higher energy, and subsequently collide with the observable cloud leading to an enhanced loss. We suppress the loss with an rf magnetic field (rf shield). Below 1 Gauss, the trap lifetime is strongly reduced and the mechanism is not as well understood. We have eliminated processes due to the

finite depth of the TOP trap and cloud density. A possible candidate is broad-band magnetic field noise that weakly drives atoms into untrapped atomic states. The mechanism is rather generic and may be the primary technical limitation to low magnetic field lifetimes in all magnetic traps. Reducing magnetic field noise could allow evaporative cooling in atomic Cs to reach BEC. In other studies we attempted to quantify the TOP criteria 6.1. We can conclude that there is no change in TOP trap lifetime when the rotation frequency is at least 25 times smaller than the Larmor frequency, and at least 8 times larger than the axial trap oscillation frequency. Unfortunately, technical problems impair our ability to draw conclusions about the trap lifetimes at rotation frequencies closer to the Larmor frequency and trap frequencies. This finding eliminates loss-of-adiabaticity in the TOP as a mechanism for the losses from low-bias field traps reported here.

The TOP and IP magnetic traps offer a multitude of options for experiments with trapped atoms and BEC. With the results of the present work and other insights we have made over the past several years we can now place the TOP trap in its context as a tool for the atomic physicist. Table 6.2 summarizes some of the advantages and disadvantages of the TOP magnetic trap. The TOP is clearly not always the best magnetic trap. For the largest field gradients and tightest confinement an IP trap (for example, the cloverleaf design [121]) is still better. IP traps can also achieve much larger differences in axial and radial frequencies in cylindrically symmetric traps. Large bias fields ($> 100$ G) rotating at several kHz are difficult to generate, given limitations on power dissipation. Thus, exploiting most of the Feshbach resonances predicted in alkali atoms is only feasible in IP traps [196, 197]. Even a modest TOP bias field is difficult to generate if a steel vacuum system is used, due to eddy

currents [198]. Both limits to the bias field limit the depth of the TOP, and probably prohibits loading atom samples that are not cooled below the Doppler Temperature. Finally, the time-dependent nature of the magnetic fields can complicate precision metrology in a TOP at the kHz level, such as measurement of atomic hyperfine transitions [199].

On the other hand, the TOP trap is very simple and contains a number of features that are nearly as good as, if not superior to, the IP traps. The TOP can cover a wide range of frequencies (almost a factor of 80, from a few Hz to 300 Hz axially) and bias fields (a factor of 250, from 0.2 to 50 Gauss). The TOP design is fairly economical: It requires only six coils, two of which are the anti-Helmholtz coils that are already part of experiments using MOT's. As a result, loading the atoms into the TOP trap from the MOT is relatively simple because the centers of MOT and TOP are quasi-aligned. The rotating bias field is a natural quantization axis that can be used over all 360° of the rotation plane. The time-dependence of the bias, while a hinderance to some precision measurements, can be a feature as well. Adjusting the frequency and amplitude of the rotating bias is a way to carefully control the amount of relative sag between states whose magnetic moments are identical [199, 163]. The rotation is also a natural method of angular averaging – an effect that can substantially reduce systematic errors in measurements of beta decay [200]. In terms of evaporative cooling, the TOP trap is assured of having at least 2-d evaporation, whereas gravitational sag can sometimes limit IP traps to 1-d. In fact, the quadrupole zero alone can perform evaporative cooling without any rf required [201]. We believe that these positives and the features discussed in the present work will continue to make the TOP magnetic trap an attractive choice for a number of experiments.

| Positive | Negative |
|---|---|
| 1. simple, compact 6 coil design | 1. gradients and trap frequencies smaller than Cloverleaf IP traps |
| 2. simple, analytical potential | 2. low-trap depths and limited maximum cloud sizes |
| 3. tunable aspect ratio: $< 1 \leftrightarrow \sqrt{8}$ | 3. large bias fields $> 100$ G are difficult |
| 4. low anharmonicities for most trap symmetries | 4. asymmetry above $\sqrt{8}$ not possible for high frequencies |
| 5. wide frequency range | 5. synchronization electronics, transformers needed |
| 6. intrinsic bias field/quantization axis with $2\pi$ orientation angles | 6. rotating field causes eddy-current heating of stainless-steel cells and limits size of bias field [198] |
| 7. variable drive symmetries for creating excitations in trapped clouds | 7. lifetime below 1 G is short |
| 8. near-cylindrical symmetry easy | 8. difficult to achieve 3-D evaporation |
| 9. center of TOP is very near the center of MOT due to quadrupole field | 9. shaving loss from quadrupole zero |
| 10. tunable sag in trap for different hyperfine states [199] | 10. time-dependent field complicates precision metrology |
| 11. low-bias field traps easy to make | |
| 12. cylindrically symmetric TOP always has 2-D RF evaporative cooling | |
| 13. stray DC magnetic fields only shift trap center and don't alter trap shape | |
| 14. no large fluctuation in net bias field | |
| 15. built in 2-D evaporation from quadrupole zero [201] | |
| 16. rotating bias averages over all angles | |

Table 6.2: Positive and Negative Features of the TOP Magnetic Trap

## Bibliography


[1] This paper first appeared in J. Opt. Soc. Am. B **11**, 1332 (1994).

[2] This paper first appeared in Phys. Rev. A, **50** R3597 (1994).

[3] This paper first appeared in Phys. Rev. Lett., **74** 3352 (1995).

[4] This paper first appeared in Science **269**, 133 (1995).

[5] F. Dalfovo and S. Stringari, Phys. Rev. A **53**, 2477 (1996).

[6] D. S. Jin *et al.*, Czech. J. Phys. **46**, 3070 (1996), Suppl. S6.

[7] M. J. Holland, D. S. Jin, M. L. Chiofalo, and J. Cooper, Phys. Rev. Lett. **78**, 3801 (1997).

[8] D. S. Jin *et al.*, Phys. Rev. Lett. **77**, 420 (1996).

[9] M. Edwards *et al.*, Phys. Rev. Lett. **77**, 1671 (1996).

[10] P. A. Ruprecht, M. Edwards, K. Burnett, and C. W. Clark, Phys. Rev. A **54**, 4178 (1996).

[11] B. D. Esry and C. H. Greene, Private Communication, 1996.

[12] S. Stringari, Phys. Rev. Lett. **77**, 2360 (1996).

[13] J. R. Ensher *et al.*, Phys. Rev. Lett. **77**, 4984 (1996).

[14] S. Grossmann and M. Holthaus, Phys. Lett. A **208**, 188 (1995).

[15] W. Ketterle and N. J. van Druten, Phys. Rev. A **54**, 656 (1996).

[16] W. H. Keesom and K. Clusius, Proc. Roy. Acad. Amsterdam **35**, 307 (1932).

[17] W. H. Keesom and A. P. Keesom, Proc. Roy. Acad. Amsterdam **35**, 736 (1932).

[18] A. Minguzzi, S. Conti, and M. P. Tosi, Jour. Phys. - Cond. Matt. **9**, L33 (1997).

[19] W. Petrich, M. H. Anderson, J. R. Ensher, and E. A. Cornell, J. Opt. Soc. Am. B **11**, 1332 (1994).

[20] M. H. Anderson, W. Petrich, J. R. Ensher, and E. A. Cornell, Phys. Rev. Lett. **50**, R3597 (1994).

[21] W. Petrich, M. H. Anderson, J. R. Ensher, and E. A. Cornell, Phys. Rev. Lett. **74**, 3352 (1995).

[22] M. H. Anderson *et al.*, Science **269**, 198 (1995).

[23] A. Einstein, Sitzungsber. Kgl. Preuss. Akad. Wiss. **1924**, 261 (1924).

[24] S. Bose, Z. Phys. **26**, 178 (1924).

[25] K. Huang, Statistical Mechanics (John Wiley and Sons, New York, 1987).

[26] M. Bijlsma and H. T. C. Stoof, Phys. Rev. A **54**, 5085 (1996).

[27] N. J. van Druten and W. Ketterle, Phys. Rev. Lett. **79**, 549 (1997).

[28] Actually, the notion that superfluidity was a manifestation of Bose-Einstein Condensation was seen as highly controversial in the early theory of liquid Helium. Landau rejected the idea in favor of quantum hydrodynamics. See the Ref. [37] for more discussion.

[29] G. E. Brown, in Bose-Einstein Condensation, edited by A. Griffin, D. W. Snoke, and S. Stringari (Cambridge University Press, Cambridge, 1995), Chap. 18, pp. 438–451.

[30] J. Ranninger, in Bose-Einstein Condensation, edited by A. Griffin, D. W. Snoke, and S. Stringari (Cambridge University Press, Cambridge, 1995), Chap. 16, pp. 393–417.

[31] F. Iachello, in Bose-Einstein Condensation, edited by A. Griffin, D. W. Snoke, and S. Stringari (Cambridge University Press, Cambridge, 1995), Chap. 17, pp. 418–437.

[32] J. L. Lin and J. P. Wolfe, Phys. Rev. Lett **71**, 1222 (1993).

[33] A. Mysyrowicz, D. Hulin, and A. Antonetti, Phys. Rev. Lett. **43**, 1123 (1979).

[34] E. Fortin, S. Fafard, and A. Mysyrowicz, Phys. Rev. Lett. **70**, 3951 (1993).

[35] A. Einstein, Sitzungsber. Kgl. Preuss. Akad. Wiss. **1925**, 3 (1925).

[36] English translation of Einstein's quotes and historical interpretation are from A. Pais, Subtle is the Lord..., (Oxford University Press, Oxford, 1982).

[37] K. Gavroglu, Fritz London (Cambridge University Press, New York, 1995).

[38] F. London, Nature **141**, 643 (1938).

[39] L. Tisza, Nature **141**, 913 (1938).

[40] L. D. Landau, J. Phys. Moscow **5**, 71 (1941).

[41] R. P. Feynman, in Progress in Low Temperature Physics, edited by C. J. Gorter (North-Holland, Amsterdam, 1955), Vol. I, p. 17.

[42] L. P. Pitaevski, Sov. Phys. JETP **12**, 155 (1961).

[43] P. Sokol, in Bose-Einstein Condensation, edited by A. Griffin, D. W. Snoke, and S. Stringari (Cambridge University Press, Cambridge, 1995), Chap. 4, pp. 51–85.

[44] D. M. Ceperley, Rev. Mod. Phys. **67**, 279 (1995).

[45] C. E. Hecht, Physica **25**, 1159 (1959).

[46] W. C. Stwalley and L. H. Nosanow, Phys. Rev. Lett. **36**, 910 (1976).

[47] I. F. Silvera and J. T. M. Walraven, Phys. Rev. Lett. **44**, 164 (1980).

[48] W. N. Hardy, M. Morrow, R. Jochemsen, and A. J. Berlinsky, Physica **109**, 1964 (1982).

[49] H. F. Hess *et al.*, Phys. Rev. Lett. **51**, 483 (1983).

[50] B. R. Johnson *et al.*, Phys. Rev. Lett. **52**, 1508 (1984).

[51] D. A. Bell *et al.*, Phys. Rev. B **34**, 7670 (1986).

[52] R. Sprik, J. T. M. Walraven, and I. F. Silvera, Phys. Rev. B **32**, 5668 (1985).

[53] H. F. Hess, Phys. Rev. B. **34**, 3476 (1986).

[54] Proceedings of the International School of Physics 'Enrico Fermi', Course CXVIII, Laser Manipulation of Atoms and Ions, edited by E. Arimondo, W. D. Phillips, and F. Strumia (North Holland, Amsterdam, 1992).

[55] S. Chu, Rev. Mod. Phys. **70**, 685 (1998).

[56] C. N. Cohen-Tannoudji, Rev. Mod. Phys. **70**, 707 (1998).

[57] W. D. Phillips, Rev. Mod. Phys. **70**, 721 (1998).

[58] D. J. Wineland and H. Dehmelt, Bull, Am. Phys. Soc. **20**, 637 (1975).

[59] T. W. Hänsch and A. L. Schawlow, Opt. Commun. **13**, 68 (1975).

[60] V. Letokhov, Pis'ma Zh. Eksp. Teor. Fiz. **7**, 348 (1968).

[61] J. E. Bjorkholm, R. E. Freeman, A. Ashkin, and D. Pearson, Phys. Rev. Lett. **41**, 1361 (1978).

[62] W. Neuhauser, M. Hohenstatt, P. Toschek, and H. Dehmelt, Phys. Rev. Lett. **41**, 233 (1978).

[63] D. J. Wineland, R. E. Drullinger, and F. L. Walls, Phys. Rev. Lett. **40**, 1639 (1978).

[64] S. V. Andreev, V. I. Balykin, V. S. Letokhov, and V. G. Minogin, Pis'ma Zh. Eksp. Teor. Fiz. **34**, 463 (1981), [JETP Lett., **34**, 442 (1981)].

[65] J. Prodan *et al.*, Phys. Rev. Lett. **54**, 992 (1985).

[66] W. Ertmer, A. Migdall, J. L. Hall, and M. Zhu, Phys. Rev. Lett. **54**, 996 (1985).

[67] S. Chu *et al.*, Phys. Rev. Lett. **55**, 48 (1985).

[68] W. D. Phillips, J. V. Prodan, and H. J. Metcalf, J. Opt. Soc. Am. B **2**, 1751 (1985).

[69] A. Aspect *et al.*, Phys. Rev. Lett. **57**, 1688 (1986).

[70] P. J. Martin *et al.*, Phys. Rev. A **36**, 2495 (1987).

[71] S. Chu, J. E. Bjorkholm, A. Ashkin, and A. Cable, Phys. Rev. Lett. **57**, 314 (1986).

[72] E. L. Raab *et al.*, Phys. Rev. Lett. **59**, 2631 (1987).

[73] P. D. Lett *et al.*, Phys. Rev. Lett. **61**, 169 (1988).

[74] J. Dalibard *et al.*, in Proceedings of the 11th International Conference on Atomic Physics, edited by S. Haroche, J. C. Gay, and G. Grynberg (World Scientific, Singapore, 1989), pp. 199–214.

[75] S. Chu, D. S. Weiss, Y. Shevy, and P. J. Ungar, in Proceedings of the 11th International Conference on Atomic Physics, edited by S. Haroche, J. C. Gay, and G. Grynberg (World Scientific, Singapore, 1989), pp. 636–638.

[76] J. Dalibard and C. Cohen-Tannoudji, J. Opt. Soc. Am. B **6**, 2023 (1989).

[77] T. Walker, D. Sesko, and C. Wieman, Phys. Rev. Lett. **64**, 408 (1990).

[78] N. Davidson, H.-J. Lee, M. Kasevich, and S. Chu, Phys. Rev. Lett. **72**, 3158 (1994).

[79] J. Lawall *et al.*, Phys. Rev. Lett. **75**, 4194 (1995).

[80] W. Ketterle *et al.*, Phys. Rev. Lett. **70**, 2253 (1993).

[81] Although see H. J. Lee and S. Chu, *Phys. Rev. A.* **57**, 2905 (1998) for recent progress, and a preprint by H. Katori, T. Ito, Y. Isoya and M. Kuwata-Gonokami.

[82] D. E. Pritchard, Phys. Rev. Lett. **51**, 1336 (1983).

[83] A. L. Migdall *et al.*, Phys. Rev. Lett. **54**, 2596 (1985).

[84] V. S. Bagnato *et al.*, Phys. Rev. Lett. **58**, 2194 (1987).

[85] R. V. E. Lovelace, C. Mehanian, T. J. Tommila, and D. M. Lee, Nature **318**, 30 (1985).

[86] J. M. Doyle *et al.*, Phys. Rev. Lett. **67**, 603 (1991).

[87] J. M. Doyle, Ph.D. thesis, Massachusetts Institute of Technology, 1991.

[88] O. J. Luitin *et al.*, Phys. Rev. Lett. **70**, 544 (1993).

[89] C. Monroe, W. Swann, H. Robinson, and C. Wieman, Phys. Rev. Lett. **65**, 1571 (1990).

[90] C. Monroe, E. Cornell, and C. Wieman, in Proceedings of the International School of Physics 'Enrico Fermi', Course CXVIII, Laser Manipulation of Atoms and Ions, edited by E. Arimondo, W. D. Phillips, and F. Strumia (North Holland, Amsterdam, 1992), pp. 361–377.

[91] E. A. Cornell, C. Monroe, and C. E. Wieman, Phys. Rev. Lett. **67**, 2439 (1991).

[92] C. R. Monroe *et al.*, Phys. Rev. Lett. **70**, 414 (1993).

[93] C. J. Myatt *et al.*, Opt. Lett. **21**, 290 (1996).

[94] N. R. Newbury, C. J. Myatt, and C. E. Wieman, Phys. Rev. A **51**, R2680 (1995).

[95] J. D. Gillaspy, I. F. Silvera, and J. S. Brooks, Phys. Rev. B **40**, 210 (1989).

[96] Y. Kagan, I. A. Vartanyants, and G. V. Shlyapnikov, Sov. Phys. JETP **54**, 590 (1981).

[97] Y. Kagan, G. V. Shlyapnikov, and I. A. Vartanyants, Phys. Lett. **101A**, 27 (1984).

[98] A. Lagendijk, I. F. Silvera, and B. J. Verhaar, Phys. Rev. B **33**, 626 (1986).

[99] D. E. Pritchard, in Electronic and Atomic Collisions, edited by D. C. Lorents, W. E. Meyerhof, and J. R. Peterson (North Holland, Amsterdam, 1986), pp. 593–604.

[100] M. Prentiss *et al.*, Opt. Lett. **13**, 452 (1988).

[101] P. L. Gould *et al.*, Phys. Rev. Lett. **60**, 788 (1988).

[102] D. Sesko *et al.*, Phys. Rev. Lett. **63**, 961 (1989).

[103] K. Gibble and S. Chu, Phys. Rev. Lett. **70**, 1771 (1993).

[104] K. B. Davis *et al.*, Phys. Rev. Lett. **74**, 5202 (1995).

[105] H. R. Thorsheim, J. Weiner, and P. S. Julienne, Phys. Rev. Lett. **58**, 2420 (1987).

[106] J. D. Miller, R. A. Cline, and D. J. Heinzen, Phys. Rev. Lett. **71**, 2204 (1993).

[107] P. D. Lett *et al.*, Phys. Rev. Lett. **71**, 2200 (1993).

[108] J. R. Gardner *et al.*, Phys. Rev. Lett. **74**, 3764 (1995).

[109] W. I. McAlexander *et al.*, Phys. Rev. A **51**, R871 (1995).

[110] E. R. I. Abraham, W. I. McAlexander, C. A. Sackett, and R. G. Hulet, Phys. Rev. Lett. **74**, 1315 (1995).

[111] K. Gibble, S. Chang, and R. Legere, Phys. Rev. Lett. **75**, 2666 (1995).

[112] C. G. Townsend *et al.*, Phys. Rev. A **52**, 1423 (1995).

[113] W. Ketterle, Private Communication, 1995.

[114] J. J. Tollett, C. C. Bradley, C. A. Sackett, and R. G. Hulet, Phys. Rev. A **51**, R22 (1995).

[115] D. Pritchard *et al.*, in Proceedings of the 11th International Conference on Atomic Physics, edited by S. Haroche, J. C. Gay, and G. Grynberg (World Scientific, Singapore, 1989), pp. 619–621.

[116] A. G. Martin *et al.*, Phys. Rev. Lett. **61**, 2431 (1988).

[117] C. S. Adams *et al.*, Phys. Rev. Lett. **74**, 3577 (1995).

[118] R. G. Hulet, Bull. Am. Phys. Soc. **40**, 1267 (1995).

[119] K. B. Davis *et al.*, Phys. Rev. Lett. **75**, 3969 (1995).

[120] C. C. Bradley, C. A. Sackett, J. J. Tollett, and R. G. Hulet, Phys. Rev. Lett. **75**, 1687 (1995), *ibid.* **79**, 1170 (1997).

[121] M.-O. Mewes *et al.*, Phys. Rev. Lett. **77**, 416 (1996).

[122] C. J. Myatt *et al.*, Phys. Rev. Lett. **78**, 586 (1997).

[123] This chapter is an expanded version of material that appeared in Ref. [6].

[124] L. P. Pitaevski, Sov. Phys. JETP **13**, 451 (1961).

[125] E. P. Gross, Nuovo Cimento **20**, 454 (1961).

[126] E. P. Gross, J. Math. Phys. **4**, 195 (1963).

[127] The system is dilute if the interparticle spacing is much larger than the two-body scattering length $a$ describing binary collisions between bosons. In other words, $na^3 \ll 1$ where $n$ is the density. By this standard, condensates of $^{87}$Rb [22] are indeed dilute: with densities of up to $\sim 10^{13}$ atoms/cm$^3$ and $a \approx 6.0$ nm the product $na^3 \sim 10^{-6}$.

[128] In the Gross-Pitaevskii equation, the ratio of interaction strength to the harmonic oscillator energy scales as $na/\nu_r$, where $n$ is the density of the condensate wavefunction. For the current experiments, the interactions are weak enough that the density profile is still approximately Gaussian, for which $n \sim N\nu_r^{3/2}$. In contrast, in the Thomas-Fermi limit the interactions are so strong that the density profile is a paraboloid for which $n \sim N^{2/5}\nu_r^{6/5}$.

[129] V. V. Goldman, I. F. Silvera, and A. J. Leggett, Phys. Rev. B **24**, 2870 (1981).

[130] G. Baym and C. J. Pethick, Phys. Rev. Lett. **76**, 6 (1996).

[131] H. M. J. M. Boesten, C. C. Tsai, D. J. Heinzen, and B. J. Verhaar, Private Communication, 1996.

[132] H. F. Hess *et al.*, Phys. Rev. Lett. **59**, 672 (1987).

[133] The release of the atoms for ballistic expansion is initiated by a sudden increase in the transverse bias field, which quenches the confining forces on a time-scale fast compared to any cloud dynamics. Interactions and residual kinetic energy cause the cloud to fly apart. The error in the final velocity determination due to residual magnetic fields is less than 2%.

[134] A. L. Fetter, Czech. J. Phys. **46**, 547 (1996), Suppl. S1.

[135] K. Singh and D. Rokhsar, Private Communication, 1996.

[136] This chapter is an expanded version of material that appeared in Ref. [8].

[137] The remaining noncondensate atoms represent less than 20% of the sample. We find good agreement between the calculated and measured BEC transition temperatures; this data will be presented in a future paper.

[138] A. L. Fetter and J. D. Walecka, Quantum Theory of Many-Particle Systems (McGraw-Hill, New York, 1971).

[139] A connection between the phase of the condensate perturbation and the ultimate width of the expanded cloud may be obtained by numerical integration of the non-linear Schrödinger equation. See for example P. A. Ruprecht, M. J. Holland, K. Burnett, and M. Edwards, Phys. Rev. A **51**, 4704 (1995); M. Holland and J. Cooper, Phys. Rev. A **53**, 1954 (1996).

[140] N. N. Bogoliubov, J. Phys. Moscow **11**, 23 (1947).

[141] D. S. Jin *et al.*, Phys. Rev. Lett. **78**, 764 (1997).

[142] C. C. Bradley, C. A. Sackett, and R. G. Hulet, Phys. Rev. Lett. **78**, 985 (1997).

[143] M.-O. Mewes *et al.*, Phys. Rev. Lett. **77**, 988 (1996).

[144] This chapter is an expanded version of material that appeared in Ref. [13].

[145] Some smoothing is performed in the wings of the distribution, where signal-to-noise is poor, using the same set of assumptions we use for thermometry.

[146] As the excluded central region is enlarged, systematic bias in the inferred temperature vanishes, but so does signal-to-noise. We found it necessary to fit to a region which unfortunately samples the outer edge of the degenerate portion of the cloud. From numerical studies of the ideal Bose-Einstein distribution, we derive and apply a modest ($< 10\%$) correction to the measured temperature. The feature we see in the cloud energy occurs regardless of whether we include this correction.

[147] S. R. de Groot, G. J. Hooyman, and C. A. ten Seldam, Proc. R. Soc. A **203**, 266 (1950).

[148] F. Dalfovo, S. Giorgini, L. Pitaevskii, and S. Stringari, Czech. J. Phys. **46**, 545 (1996), Suppl. S1.

[149] M. Bijlsma and H. T. C. Stoof, Czech. J. Phys. **46**, 553 (1996), Suppl. S1.

[150] H. J. Davies and C. S. Adams, Phys. Rev. A **55**, R2527 (1997).

[151] S. Giorgini, L. P. Pitaevskii, and S. Stringari, Phys. Rev. Lett. **78**, 3987 (1997).

[152] C. J. Myatt, Ph.D. thesis, University of Colorado, 1997.

[153] From Eq.(1.5), the collection rate of a vapor cell MOT scales as $R \sim V^{2/3} v_c^4$. The MOT volume $V = L^3$, where the volume is assumed to be a cube with side length $L$ equal to the MOT beam diameter. The capture velocity $v_c$ is proportional to the deceleration from spontaneously scattered photons and the distance over which that force acts. Thus, $v_c \sim IL^2$, where $I$ is the laser intensity, and the collection rate $R \sim I^2 L^4$.

[154] We use a 5 cm high breadboard that is more than rigid enough. The excess height of the breadboard reduces the optical access below the cells because our standard height for laser beams is only 15.2 cm. The entire vacuum system may be elevated even higher than the beam heights, but that introduces other problems: the beams are raised closer to eye levels and longer mounts are required, making the entire system more prone to vibrations.

[155] K. B. MacAdam, A. Steinbach, and C. Wieman, Am. J. Phys. **60**, 1098 (1992).

[156] F. E. Terman, Radio Engineers' Handbook, textbook ed. (McGraw-Hill, New York, 1943), pp. 53–64.

[157] C. R. Monroe, Ph.D. thesis, University of Colorado, 1992.

[158] D. Hoffmann, P. Feng, and T. Walker, Measurements of Rb trap-loss collision spectra, 1994.

[159] Z. T. Lu *et al.*, Phys. Rev. Lett. **77**, 3331 (1996).

[160] E. Majorana, Nuovo Cimento **8**, 107 (1931).

[161] J. Dalibard, Private Communication, 1998.

[162] T. Esslinger, I. Bloch, and T. W. Hänsch, Phys. Rev. A **58**, R2664 (1998).

[163] D. S. Hall *et al.*, Phys. Rev. Lett. **81**, 1539 (1998).

[164] D. J. Han, R. H. Wynar, P. Courteille, and D. J. Heinzen, Phys. Rev. A **57**, R4114 (1998).

[165] B. P. Anderson and M. A. Kasevich, Bull. Am. Phys. Soc. **43**, 1251 (1998).

[166] A. Wilson, Private Communication, 1998.

[167] L. Deng *et al.*, Bull. Am. Phys. Soc. **43**, 1379 (1998).

[168] M. Arndt *et al.*, Phys. Rev. Lett. **79**, 625 (1997).

[169] J. Arlt *et al.*, J. Phys. B **31**, L321 (1998).

[170] E. Arimondo, Private Communication, 1998.

[171] T. Bergeman, G. Erez, and H. Metcalf, Phys. Rev. A **35**, 1535 (1987).

[172] M. R. Matthews *et al.*, Phys. Rev. Lett. **81**, 243 (1998).

[173] V. E. Shapiro, Phys. Rev. A **54**, R1018 (1996).

[174] A. B. Kuklov *et al.*, Phys. Rev. A **55**, 488 (1997).

[175] J. D. Luca, R. Napolitano, and V. S. Bagnato, Phys. Rev. A **55**, R1597 (1997).

[176] V. I. Yukalov, Phys. Rev. A **56**, 5004 (1997).

[177] V. Minogin, J. A. Richmond, and G. I. Opat, Phys. Rev. A **58**, 3138 (1998).

[178] J. Dalibard, Lectures at the 1998 Enrico Fermi Summer School on BEC in Varenna, Italy.

[179] L. D. Landau and E. M. Lifshitz, Mechanics, 3rd ed. (Pergamon Press, Oxford, 1973).

[180] It should be possible to use large radial symmetry breaking in a rotating magnetic potential to impart angular momentum to cold atom clouds.

[181] We minimize phase uncertainty in the measured frequencies by fitting complete oscillation periods many periods apart. Systematic uncertainties due to anharmonic frequency shifts are below 0.1%.

[182] The argument in this paragraph is due to C. Monroe and E. Cornell. The results have been numerically validated by B. Verhaar's group.

[183] J. Söding *et al.*, Phys. Rev. Lett. **80**, 1869 (1998).

[184] E. A. Burt *et al.*, Phys. Rev. Lett. **79**, 337 (1997).

[185] M. E. Gehm, K. M. O'Hara, T. A. Savard, and J. E. Thomas, Phys. Rev. A **58**, 3914 (1998).

[186] The exponential decay curve suggests that the loss mechanism is more complicated than three three-body dominated loss, which should show a non-exponential loss of atoms with time.

[187] Our noise detection method provides a genuine measure of the noise on the TOP coils and an estimate of the noise near the atoms that is better than a factor of two. Noise power registered on the pick-up coil directly reflects noise on the TOP coil because the pick-up coil is wrapped immediately next to one of the TOP coils. The absolute noise voltage registered on the rf spectrum analyzer is calibrated with a digital FFT. The uncertainty in the measured voltage, determined by statistical noise in the power spectrum, is less than 3 dB. The resonance frequency of the pick-up coil does not influence the measured voltage since the resonance occurs at a much higher frequency than what we measure. We calculate the magnetic field noise at the location of the atoms from an estimate of the distance between the trapped atoms and the TOP coil.

[188] The details of this approach are discussed in Ref. [185], in the context of noise-induced heating in traps. We similarly reason that the averaging time $T$ is short compared to the time scale over which the level populations change, but is long compared to the correlation time of the magnetic field fluctuations.

[189] We assume that the loss rate is slow enough that (i) once an atom has made a transition to the $m = 0$ state it is lost from the trap before it can return to the $m = -1$ state; and (ii) the time-averaged magnetic field determines the Zeeman splitting at a point $\vec{r}$ in the potential. The roll-off in the power spectral density at high frequencies implies that atoms further from the trap center, which sample larger magnetic fields, are less likely to be lost from the trap.

[190] The three-body recombination rate is calculated assuming a per atom rate that is constant with magnetic field, using the initially measured condensate central density. Thus, the rate is an upper limit to the rate of loss we expect from recombination events. The background collision rate is assumed to be constant and equal to the lifetime measured for a classical cloud in a 6.2 Gauss trap.

[191] At low $\omega_T$, the ferrite-core transformer, which couples the oscillating currents to the TOP coils, has decreased coupling efficiency. The circuit which generates the oscillating currents is also a limitation. At high $\omega_T$, the roll-off in the amplitude gain and phase response in the circuit limits TOP operation above 30 kHz rotation frequencies. As a result of these two constraints, we can only preserve the same bias field ($\leq 1$ Gauss) for frequencies down to 150 Hz and up to 27 kHz. The limitations to high-frequency operation force us to lower the bias field such that $\omega_L \rightarrow \omega_T$. However, we cannot go to extremely low bias fields without sacrificing lifetime (see Section 6.5). A similar trade-off occurs in studying traps of low $\omega_T$. We can create axial trap frequencies of several hundred Hz, but the increased density of the cloud limits the lifetime through three-body recombination.

[192] We reduce the number of atoms by almost a factor of 100 by cutting deeply with the rf into a pure condensate. The deeper cuts are less repeatable and cause increased shot-to-shot fluctuations in the number of atoms, which contribute to the larger uncertainty in the lifetimes for these data.

[193] F. Dalfovo, C. Minniti, and L. P. Pitaevskii, Phys. Rev. A **56**, 4855 (1997).

[194] L. P. Pitaevskii and S. Stringari, Phys. Lett. A **235**, 398 (1997).

[195] L. Pitaevskii and S. Stringari, Phys. Rev. Lett. **81**, 4541 (1998).

[196] S. Inouye *et al.*, Nature **392**, 151 (1998).

[197] J. L. Roberts *et al.*, Phys. Rev. Lett. **81**, 5109 (1998).

[198] D. Heinzen, Private Communication, 1998.

[199] D. S. Hall *et al.*, Proc. SPIE **3270**, 98 (1998).

[200] D. J. Vieira, 1998, private Communication.

[201] K. Helmerson, Private Communication, 1998.

[202] A. M. Steane, M. Chowdhury, and C. J. Foot, J. Opt. Soc. Am. B **9**, 2142 (1992).

[203] C. Wieman, C. Monroe, and E. Cornell, in Proceedings of the Tenth International Conference on Laser Spectroscopy 4, edited by M. D. E. Giambini and G. Camy (World Scientific, Singapore, 1992).

[204] L. Marcassa *et al.*, Phys. Rev. A **47**, R4563 (1993).

[205] K. Lindquist, M. Stephens, and C. Wieman, Phys. Rev. A **46**, 4082 (1992).

[206] A. M. Steane and C. J. Foot, Europhys. Lett. **14**, 231 (1991).

[207] C. D. Wallace, T. P. Dinneen, K. Y. N. Tan, A. Kumarakrishnan, P. L. Gould, and J. Javanainen, University of Connecticut, Storrs, Mansfield, Conn. 06269 (personal communication, 1994).

[208] J. Werner, H. Wallis, and W. Ertmer, Opt. Commun. **94**, 525 (1992).

[209] D. W. Sesko, T. G. Walker, and C. E. Wieman, J. Opt. Soc. Am. B **8**, 946 (1991).

[210] A. Höpe *et al.*, Europhys. Lett. **22**, 669 (1993).

[211] It has been brought to our attention that an increase in density for larger detunings was also observed by C. Salomon and co-workers, Hertzienne de l'Ecole Nationale Supérieure, Laboratoire de Spectroscopie, 75231 Paris Cedex, France (personal communication), 1994; M. Drewsen, Ph. Laurent, A. Nadir, G. Santarelli, A. Clairon, Y. Castin, D. Grison, and C. Salomon, 'Investigation of sub-Doppler cooling effects in a cesium magneto-optical trap,' submitted to Appl. Phys. B.

[212] The calculations in Ref. [202] are valid only for small saturation parameters and for a $J = 0 \rightarrow J' = 1$ transition. Hence we cannot infer any quantitative statement by comparing our results directly with these calculations.

[213] N. Masuhara *et al.*, Phys. Rev. Lett. **61**, 935 (1988).

[214] M. Stephens, R. Rhodes, and C. Wieman, J. Appl. Phys. **76**, 3479 (1994).

[215] T. Walker and P. Feng, in Advances in Atomic, Molecular and Optical Physics, edited by B. Bederson and H. Walther (Academic Press, San Diego, 1994), Vol. 34, pp. 125–170.

[216] P. Feng, D. Hoffmann, and T. Walker, Phys. Rev. A **47**, R3495 (1993).

[217] C. Wallace *et al.*, Phys. Rev. Lett. **69**, 897 (1992).

[218] Numerical integration of Eq. B.1 yields a fill profile which is remarkably exponential, even with a large nonlinear loss term. The nonlinearity causes a surprising asymmetry between a fill profile and its related loss profile.

[219] For the case of retroreflected repumping beams we have not observed a dependence on the sign of the repumping laser detuning. However, it is normally positive.

[220] Lifetimes on the order of 50 min have also been observed for small numbers of trapped atoms by K. Libbrecht and coworkers, California Institute of Technology, Pasadena (private communication, 1994).

[221] A. Cable, M. Prentiss, and N. P. Bigelow, Opt. Lett. **15**, 507 (1990).

[222] T. H. Bergeman *et al.*, J. Opt. Soc. Am. B **6**, 2249 (1989).

[223] A. Antillón, A. Góngora, and T. H. Seligman, Z. Phys. D **24**, 347 (1992).

[224] W. Petrich, M. H. Anderson, J. R. Ensher, and E. A. Cornell, in Abstracts of Contributed Papers, International Conference on Atomic Physics XIV, edited by D. J. Wineland, C. E. Wieman, and S. J. Smith (unpublished, Boulder, Colorado, 1994), pp. 1M–7.

[225] F. G. Major and H. Dehmelt, Phys. Rev. **170**, 91 (1968).

[226] Variations across the cloud in the phase and amplitude of the small-amplitude circular motion, coupled with the secular motion of atoms through the cloud, will give rise to a very small viscous heating associated with each intratrap collision. The scale of the velocity variation across the cloud is given by the ratio of the size of the cloud to the radius of the hole orbit, times the speed of the circular motion. As an atom moves across the cloud, there is a small amount of hysteresis, whose fractional scale is given by the trap frequency over the field rotation frequency, such that when short-range pairwise collisions take place the collision velocity will have an additive term of order $\delta\nu_{circ} = (\omega_t/\omega_b)(l/R_0)\mu B\prime_q/m\omega_b$. This

extra velocity, which gives rise to viscous heating, is for the present TOP parameters very small compared to(for instance) the zero-point motion of a hypothetical Bose condensate confined in the TOP trap.

[227] C. E. Wieman (private communication), 1995. See also V. Shapiro, TRI-UMF Report No. TRI-PP-94-83, 1994.

[228] There are limits to the amount the bias field may be safely reduced. As the bias field is lowered, the oscillation frequencies in the TOP will no longer be much smaller than $\omega_b$, calling into question the validity of time averaging the potential. Furthermore, for very low bias fields the Larmor frequency will no longer be much larger than $\omega_b$, and the possibility of nonadiabatic flip loss is resurrected.

[229] E. Tiesinga, B. J. Verhaar, and H. T. C. Stoof, Phys. Rev. A **47**, 4114 (1993).

[230] $\lambda_{db} = h/(2\pi mkT)^{1/2}$, where $h$ is Planck's constant, $m$ is the mass of the atom, $k$ is Boltzmann's constant, and $T$ is the temperature.

[231] For reviews of the hydrogen work, see T. J. Greytak and D. Kleppner, in New Trends in Atomic Physics, Proceedings of the Les Houches Summer School, Session XXXVIII, Les Houches, France, 22 to 28 June 1993, G. Greenberg and R. Stora, Eds. (North-Holland, Amsterdam, Netherlands, 1994), pp. 1127-1158; I. F. Silvera and J. T. M. Walraven, in Progress in Low Temperature Physics, D. Brewer, Ed. (North-Holland, Amsterdam, Netherlands, 1986), vol. 10, pp. 139-173; T. J. Greytak, in Bose Einstein Condensation, A. Griffin, D. W. Snoke, A. Stringari, Eds. (Cambridge Univ. Press, Cambridge, 1995), pp. 131-159.

[232] O. J. Luiten *et al.*, Phys. Rev. Lett. **70**, 544 (1993).

[233] Special issue on laser cooling and trapping of atoms, edited by S. Chu and C. Wieman [J. Opt. Soc. Am. B **6** (1989)].

[234] D. Pritchard *et al.*, in Proceedings of the 11th International Conference on Atomic Physics, S. Haroche, J. C. Gay, G. Grynberg, Eds. (World Scientific, Singapore, 1989), pp. 619-621. The orbiting zero-field point in the TOP trap supplements the effect of the rf by removing some high energy atoms by Majorana transitions. Two other groups have evaporatively cooled alkali atoms [C. S. Adams, H. J. Lee, N. Davidson, M. Kasevich, S. Chu, *Phys. Rev. Lett.* **74**, 3577 (1995); K. B. Davis, M. O. Mewes, M. A. Joffe, M. R. Andrews, W. Ketterle, ibid., p. 5202].

[235] J. R. Gardner *et al.* [Phys. Rev. Lett. **74**, 3764 (1995)] determined the ground-state triplet scattering lengths and found that they are positive for $^{87}$Rb and negative for $^{85}$Rb. It is believed that a positive scattering length is necessary for the stability of large samples of condensate. The $F = 2, m = 2$ state also has the advantage that, of the Rb 5S states, it is the spin state with the maximum magnetic trapping force.

[236] After the rotating field has been reduced to one third its initial value, which increases the spring constant by a factor of 3, it is held fixed (at 5 G) and the final cooling is done only with the rf ramp.

[237] After the sample is cooled to just below the transition temperature, the condensate peak does not appear immediately after the ramp ends but instead grows during this 2-s delay.

[238] This exact correspondence between velocity and coordinate-space distributions requires that the particles be an ideal gas, which is an excellent approximation in our system, except in the condensate itself. It also requires that sinusoidal trajectories of the atoms have random initial phase. This is much less restrictive than requiring thermal equilibrium.

[239] Below the transition temperature the fraction of the atoms that go into the condensate is basically set by the requirement that the phase space density of the noncondensate fraction not exceed 2.612 (for an ideal gas). As the cloud is further cooled or compressed, the excess atoms are squeezed into the condensate [25].

[240] The temperature of a classical gas that would correspond to the kinetic energy of the pure condensate cloud ($\nu_{evap} = 4.11$ MHz), after adiabatic expansion, is only 2 nK, and during the near-ballistic expansion it becomes substantially lower.

[241] E. Tiesinga, A. J. Moerdijk, B. J. Verhaar, and H. T. C. Stoof, Phys. Rev. A **46**, R1167 (1992).

[242] C. Myatt, N. Newbury, and C. Wieman, personal communication, 1995.

[243] L. You, M. Lewenstein, and J. Cooper, Phys. Rev. A **51**, 4712 (1995).

[244] O. Morice, Y. Castin, and J. Dalibard, Phys. Rev. A **51**, 3896 (1995).

[245] J. Javanainen, Phys. Rev. Lett. **72**, 2375 (1994).

[246] B. V. Svistunov and G. V. Shylapnikov, JETP **71**, 71 (1990).

[247] P. A. Ruprecht, M. J. Holland, K. Burnett, and M. Edwards, Phys. Rev. A **51**, 4704 (1995).

# Appendix A

## Behavior of atoms in a compressed magneto-optical trap [1]

### A.1 Abstract

We investigate the behavior of a cloud of atoms in a magnet-optical trap, which– after collection– is compressed when the field gradients of the trap magnetic field are increased. We measure sizes and shapes of the atom cloud as a function of laser detuning, magnetic field gradient, and number of trapped atoms. A transient density increase of more than an order of magnitude has been achieved. Moreover, reproducible Gaussian density distributions are observed at large detunings and intermediate magnetic-field gradients, permitting an accurate determination of density.

### A.2 Introduction

The ability to capture and store atoms from a vapor in a magneto-optical trap [72, 89] (MOT) has stimulated a broad field of research in atomic physics and quantum optics including cold collisions and studies of quantum effects in a dense, cold atom cloud [203, 115, 204]. Many of these experiments require high trapped-atom densities. In this appendix we investigate the properties of a trapped-atom sample that we collected using low magnetic-field gradients and subsequently compressed increasing the gradients of the confining

magnetic field. This two-step procedure avoids the drawback of low collection efficiency associated with high magnetic-field gradients in the MOT. Hence we are able to maintain a large number of atoms and to achieve a transient but substantial increase in the density of the atom cloud in the highly compressed magneto-optical trap (CMOT).

The density and the temperature of optically trapped atoms have been studied in detail [205, 202, 80]. Temperatures well below the Doppler limit have been observed and associated with polarization gradient cooling [206, 207, 208]. Density studies have uncovered two density-limiting mechanisms. For small numbers of atoms the density of the trapped atom cloud is given by the thermal motion of each individual atom in the trapping potential. Considering the trapping potential to be a simple harmonic well, we see that this motion causes the atom cloud to adopt a Gaussian density distribution with a root- mean-square radius $\langle r_i \rangle$ given by the equipartition theorem,

$$\frac{1}{2} k_B T_i = \frac{1}{2} \kappa_i \langle r_i \rangle^2 \tag{A.1}$$

where $T_i$ is the temperature, $k_B$ is the Boltzmann constant, $\kappa_i$ is the spring constant of the trap, and $i = x, y, z$. In MOT's the cloud is usually treated as being equilibrated ($T_x = T_y = T_x \equiv T$), and the spring constants in the horizontal and the vertical directions fulfill the relation $2\kappa_x = 2\kappa_y = \kappa_z \equiv K$. Hence for $N$ trapped atoms the peak density $n_p$ is given by

$$n_p \equiv \frac{N}{\sqrt{(2\pi)^3}\langle r_x\rangle\langle r_y\rangle\langle r_z\rangle} \sim N\left(\frac{\kappa}{k_B T}\right) \tag{A.2}$$

The second major density limitation arises from the reradiation of the photons within the cloud and from the attenuation of the laser beams. For large numbers of atoms the density is determined by the counterbalance between the force related to these effects and the trapping force and is calculated [209] to be proportional to

$$n_p \sim \frac{\kappa}{I\sigma_L(\sigma_R - \sigma_L)} \tag{A.3}$$

where $I$ denotes the laser intensity and $\sigma_L$ and $\sigma_R$ are the cross sections for absorbing a photon from the laser field and for absorbing a reradiated photon, respectively. Note that the density is independent of position $r$ and is therefore constant inside the cloud.

Collisions between the trapped atoms affect the lifetime of the trapped atoms and thus the number that can be accumulated in a MOT. The number of trapped atoms will in turn affect the density. But since in our experiments atom collection and density compression are accomplished at different times, we do not include collisions in our discussion of density.

From relations (A.2) and (A.3) it follows that the maximum densities in the temperature-limited and in the reradiation- limited regimes are proportional to $\kappa^{3/2}$ and $\kappa$, respectively. Our experimental approach is to modify the spring constant $\kappa$ to achieve higher densities.

Because the spring constant is proportional to the magnetic-field gradients $\partial B/\partial r_i$, it is desirable to operate the trap at large gradients when aiming for high densities. However, Höpe *et al.* [210] observed that increasing the gradients leads to a strong decrease of the loading rate $R \sim (\partial B/\partial r_i)^{-14/3}$ at which atoms are captured from the vapor gas. They reported a decrease in the number of trapped atoms from $10^7$ for a normal MOT with field gradients of the order of 10 G/cm down to 10 atoms for a vertical gradient of 207 G/cm. In contrast, for the measurements described in this paper we first collect atoms from the vapor gas, using low field gradients, and then rapidly increase the field gradients. This separation of the collection and the compression processes allows us to achieve high densities for large numbers of atoms.

In addition it can be advantageous to increase the detuning $\delta_L$ of the trapping laser beams. In the reradiation limit large detunings are expected to decrease the repelling reradiation forces strongly ($\sim \delta_L^{-4}$), while the decrease of the trapping force only scales as $\delta_L^{-1}$ in the central, low-magnetic-field region of the trap and as $\delta_L^{-3}$ in the outer region [202, 208]. Thus for a given number of atoms the new balance between these forces favors higher densities. Although in the temperature-limited regime larger detunings have been found to lead to lower temperatures, the actual densities depend on the ratio between the temperature and the (detuning-dependent) spring constant according to relation (A.2). Steane *et al.* [202] suggest that the densities in the temperature-limited regime are in fact independent of detuning.

## A.3 Experimental Procedure

For trapping $^{85}$Rb atoms from a vapor gas we employ the standard configuration of a MOT, i.e., three pairs of appropriately polarized counter-propagating laser beams intersecting in the zero point of a magnetic quadrupole field, which is created by a pair of coils in an anti-Helmholtz configuration. Light from a diode laser drives the $5s^2S_{1/2}(F = 3) \rightarrow 5p^2P_{3/2}(F' = 4)$ transition in $^{85}$Rb (natural linewidth $\Gamma/2\pi = 6$ MHz) at a wavelength of 780 nm with a peak intensity of 15 mW/cm$^2$ in each of the six beams (FWHM beam size, 7 mm). To provide hyperfine pumping we overlap the light emitted from a second laser with the trapping laser beams and repump the atoms on the $5s^2S_{1/2}(F = 2) \rightarrow 5p^2P_{3/2}(F' = 3)$ transition. At a measured effective saturation parameter of $S \approx 13$ we are able to trap up to $10^8$ atoms with a loading rate of $10^7$ atoms/s. The $1/e$ time constant for atoms to remain in the trap under these conditions is 9 s. The number of trapped atoms can be deduced from measuring a known fraction of the emitted fluorescent light on a calibrated photodiode. The accuracy in determining the absolute number of atoms is about $\pm 20\%$, whereas the measurements on relative numbers at a fixed detuning are better than $\pm 5\%$. Information on the size of the cloud is obtained by observation of the fluorescent light with a CCD camera and analysis of the obtained video pictures of the cloud with a computer. (More precisely, we store data from only the one horizontal line and the one vertical line that include the peak of the atom cloud.) The resolution of this detection scheme is better than 20 $\mu$m.

Initially we set the detuning to $-9$ MHz and the field gradient to $\partial B/\partial r_z (= 2\partial B/\partial r_{x,y}) = 11$ G/cm to optimize the collection efficiency of the

MOT. After collection for typically 0.5 s, the cloud contains $6 \times 10^6$ atoms and exhibits horizontal and vertical FWHM sizes of 0.8 and 0.3 mm, respectively, giving a density of $2 \times 10^{10}$ cm$^{-3}$. Note that in the uncompressed MOT the shape of the cloud and hence also the ratio between the horizontal and the vertical cloud sizes is significantly distorted by intensity inhomogeneities of the trapping laser beams. We then jump the detuning to various values. One millisecond after having jumped the detuning, we ramp the magnetic field in five steps over 5 ms to field gradients $\partial B/\partial r_z$ between 11 and 228 G/cm. After each step the magnetic field settles within 0.1 ms. Details of stepping time and step size are not critical unless the gradient is jumped in a single step; in this case a significant loss of atoms is observed. After establishing a new magnetic-field gradient, we allow the cloud to equilibrate for 20 ms before we measure sizes, shapes, and numbers of atoms of the cloud.

## A.4 Laser Detuning Effects

In the measurements described first, we concentrate on the influence of the laser detuning and do not change the field gradients. We collected atoms from the vapor gas for 0.5 s ($\rightarrow N \approx 6 \times 10^6$ atoms) and then jumped the laser detuning from the collection detuning $\delta_L = -9$ MHz to values of $-19$, $-32$, and $-44$ MHz at a constant vertical field gradient of $\partial B/\partial r_z = 11$ G/cm. We observe that for these low field gradients the cloud exhibits an irregular non-Gaussian shape. Hence the measured sizes and therefore also the densities in this regime have to be considered estimates. We believe that the irregular shapes are due to an increased sensitivity to laser field inhomogeneities at lower field gradients. When we jump the detuning from $-9$ to $-19$ MHz, the

cloud sizes decrease to $\approx 0.5$ mm (FWHM) in the horizontal plane and $\approx 0.3$ mm (FWHM) in the vertical direction. For larger detunings the cloud size does not decrease any further. Since the number of atoms in the trap stays approximately constant as the detuning is jumped, the estimated densities increase by a factor of 3 in going from $-9$ to $-19$ MHz (Ref.[211]) but do not increase for further detuning. The density's insensitivity to detuning above $-19$ MHz coincides with the predictions in Ref.[202] for a cloud that is density limited by its temperature; i.e., for large detunings ($4\pi\delta_L \gg \Gamma$) the cloud size should become independent of the detuning [212].

## A.5 Effect of the quadrupole field gradient

We now describe measurements in which we ramp the field gradient after we jump the laser detuning to $-44$ MHz. For this detuning and for vertical field gradients of up to 60 G/cm all atoms are compressed into a narrow peak that exhibits a Gaussian shape, permitting an accurate determination of the densities. For $\partial B/\partial r_z > 60$ G/cm, however, this narrow peak (central feature) is surrounded by a diffuse cloud of atoms. While the position and the shape of the diffuse cloud strongly depend on the alignment and the imbalance of the laser beams, the position, the shape, and the size of the central feature are relatively insensitive to slight misalignment. The existence of the two parts of the atom cloud and their differing behavior is predicted in Refs.[202] and [208]. This result is consistent with a picture of the central feature's being compressed by a strong, position-dependent polarization gradient force, which has been found to be the dominant trapping force for low magnetic fields,. i.e., in the trap center. On the other hand, in the large magnetic fields

beyond the trap center this force is suppressed, and only the spontaneous force remains, which allows the atoms to spread into a sparse cloud. In addition, even the force of the magnetic field on the magnetic moments of the atoms may be nonnegligible in this region. The precise roles of the individual forces, however, require further investigation. Figure A.1(a) shows the FWHM of the central feature in the horizontal and the vertical directions as a function of the vertical field gradient $\partial B/\partial r_z$, for the detuning of $\delta_L = -44$ MHz. The data follow the dependence expected from Eq. (A.1) for a constant temperature, i.e., $\langle r_i \rangle \sim (\partial B/\partial r_i)^{-1/2}$, and the ratio of the sizes in the horizontal and the vertical directions is close to $\sqrt{2}$ (see the dashed curves in Fig. A.1). The fraction of atoms in the central feature can be estimated from the video data, and the total number of atoms in the trap is deduced from the photodiode signal. For the detuning of $-44$ MHz we observe no measurable decrease of the total number of atoms during compression, and the lifetime of the atoms in the CMOT is found to be of the order of seconds. Although the total number of atoms stays approximately constant as the magnetic- field gradient changes, the fraction of atoms in the central feature starts to decrease for gradients larger than 60 G/cm [Fig. A.1(b)]. Knowing the total number of atoms, the Gaussian width of the central feature, and having estimated the fraction of atoms in the central feature, we calculate the peak density $n_p$ shown in Fig. A.1(c) as a function of the vertical magnetic-field gradient. For fields smaller than 60 G/cm, peak densities as high as $5 \times 10^{11}$ cm$^{-}3$ have been achieved. This corresponds to an increase in density of more than an order of magnitude compared with the density of a normal MOT ($n_p \approx 2 \times 10^{10}$ cm$^{-}3$). We point out that for this large detuning the CMOT exhibits high densities with long lifetimes and Gaussian density distributions; therefore it is an ideal tool to use

in studies that require high densities and for which a precise knowledge of this density is desirable, such as investigations of cold collisions[204].

Analogous measurements have been performed with smaller detunings of $-9$ (i.e., the normal MOT detuning), $-19$, and $-32$ MHz. In general we find lower densities and less Gaussian-shaped curves in these cases. These deviate significantly from the magnetic-field gradient dependence expected for the temperature-limited sizes $\sim (\partial B/\partial r_i)^{-1/2}$ as well as for reradiation-limited sizes $\sim (\partial B/\partial r_i)^{-1/3}$. On the other hand, we observe that the sparse cloud surrounding the central feature diminishes with decreasing detuning. In addition, we find that the total number of atoms remaining in the trap after compression also decreases; for the smallest detuning and the largest field gradient this loss amounts to 65%. The loss of atoms occurs on two time scales: a rapid loss of atoms, which is not yet understood, is observed mainly during compression, followed by a slow decay with time constants between $\approx 50$ ms ($\partial B/\partial r_z = 228$ G/cm, $\delta_L = -9$ MHz) and seconds (both the rapid loss and the slow decrease become less pronounced with larger detunings and smaller gradients). The slow loss of atoms is likely to be caused by intratrap collisions, which are dependent on the laser detuning in a manner consistent with light-assisted collisions [102]. In any case the lifetime of the CMOT would be plenty long enough to allow for the transfer of the compressed atom cloud to a purely magnetic trap, in which there would be no light-assisted collisions and where further cooling, for instance, by evaporation [213], seems feasible.

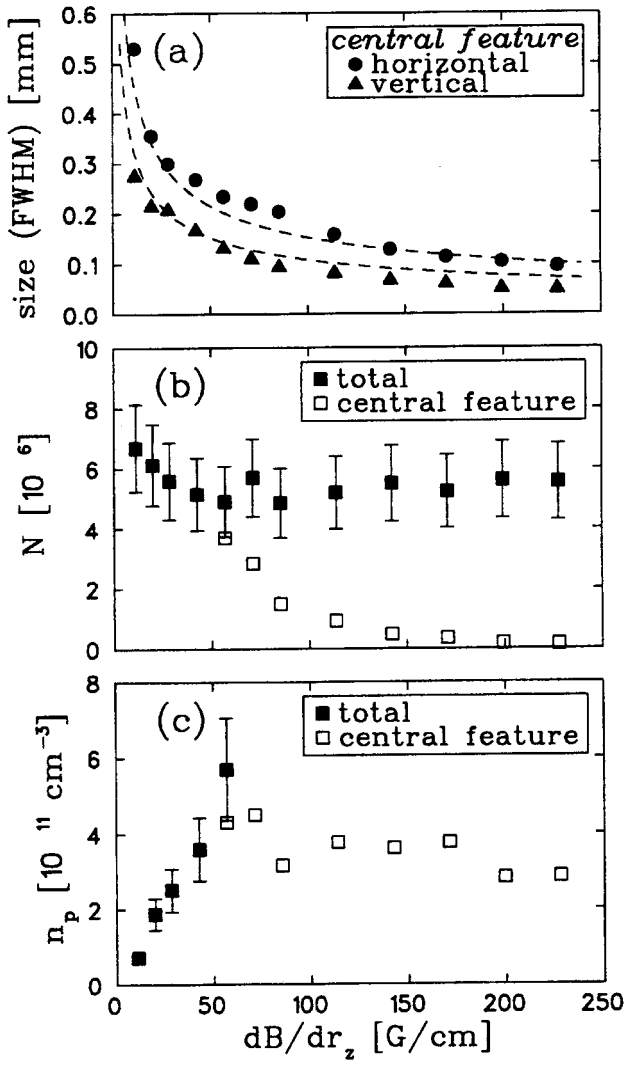


Figure A.1: (a) Horizontal and vertical sizes, (b) number of atoms, and (c) peak densities shown as a function of the vertical magnetic field gradient $\partial B/\partial r_z$ ($= 2\partial B/\partial r_{x,y}$). The detuning was set to -44 MHz. The filled symbols in (b) and (c) represent the actual parameters of the cloud, and the open symbols are an estimate of the fraction of atoms in the central feature and the peak densities connected to this estimated fraction (see text). The dashed curves in (a) are a fit to an inverse-square-root dependence with a forced ratio of $\sqrt{2}$ between the radial and the axial sizes. Figure taken from Ref. [19].

## A.6 Effect of changing the number of atoms in the trap

In a further series of measurements the collection time $\tau$ and hence the total number of atoms is varied from $\tau = 0.1$ s to $\tau = 30$ s, corresponding to $3 \times 10^6 \leq N \leq 8 \times 10^7$. After collection of the atoms the detuning is jumped to $\delta_L = -32$ MHz, and the magnetic field gradient is ramped to $\partial B/\partial r_z = 85$ G/cm. We find that both the sizes $\langle r_i \rangle$ [Fig.A.2(a)] and the number of atoms in the central feature $N_{cf}$ (Fig.A.2(b)] increase for small total numbers of atoms $N$ in the trap. Analyzing the data yields a dependence of $\langle r_i \rangle \sim \sqrt[3]{N_{cf}}$, which is expected in the reradiation-limited regime according to relation (A.3); in fact, the densities derived from the shown sizes and numbers are approximately equal and amount to $n \approx 2 \times 10^{11}$ cm$^{-3}$ [Fig.A.2(c)]. For $N \geq 2 \times 10^7$ any additionally loaded atoms are dispersed into the sparse cloud around the central feature, so the number of atoms in the central feature as well as its size do not increase any further. We believe that the limit on the size of the central feature, and therefore on the number of atoms compressed therein, arises from a suppression of polarization gradient forces for large radii. As is mentioned above, the dominant role of these forces in the center of an ordinary MOT is pointed out in Refs. [202] and [208]. Steane *et al.* [202] suggest that the high gradients, however, give rise to Larmor frequencies, which then become comparable with the optical pumping rate and the ac Stark shifts at radii small enough to be inside the actual cloud. The occurrence of large magnetic fields close to the trap center will inhibit the polarization-gradient forces even at these small radii, and in this way could lead to a limitation of the size of the strongly compressed central feature. We find the size limit of the central feature and the existence and properties of the diffuse cloud an intriguing problem worthy

of further theoretical as well as experimental studies.

## A.7 Conclusion

In summary, we have investigated the behavior of an atom cloud in a magneto-optical trap that is suddenly exposed to high magnetic-field gradients. We have studied sizes and shapes of the atom cloud as a function of the amplitude of the magnetic-field gradient, of the laser detuning, and of the total number of atoms. For large detunings and intermediate field gradients, peak densities as high as $5 \times 10^{11}$ cm$^{-3}$ are achieved, corresponding to a density increase of more than an order of magnitude compared with the density of a normal MOT. Although this density increase is in principle of a transient nature, we observe lifetimes of the order of seconds for large detunings. Moreover, we find that the density distribution in this highly compressed MOT is purely Gaussian for large detunings and intermediate field gradients. Therefore in this regime the CMOT appears to be an ideal tool for investigations that require an accurate knowledge and high values of the density, such as studies of cold collisions. Furthermore, first measurements indicate that the transfer of atoms from the normal MOT into a magnetic trap can be significantly improved by this method of compression. The resulting high densities in the magnetic trap are an important step toward the goal of evaporative cooling in the magnetic trap, which might eventually lead to the observation of collective effects such as Bose-Einstein condensation of the weakly interacting atom sample [203].